Experiences with a pre–series of Micro Strip Gas Counters with Gas Electron Multipliers for high rate applications

Von der Fakultät für Mathematik, Informatik und Naturwissenschaften der Rheinisch-Westfälischen Technischen Hochschule Aachen zur Erlangung des akademischen Grades einer Doktorin der Naturwissenschaften genemigte Dissertation

vorgelegt von

Diplom-Physikerin Anette Zander

aus Kassel

Breichter:

Universitätsprofessor Dr. Günter Flügge

Privat Dozent Dr. Wolfgang Struczinski

Tag der mündlichen Prüfung: 17. Dezember 2001

Zusammenfassung

Mikrostreifengasdetektoren (MSGCs) sind ein vielversprechender Kandidat für großflächige Anwendungen. Sie vereinen eine gute Ortsauflösung mit hoher Granularität und einem geringen Preis. Als mögliche Erweiterung der einfachen MSGC kann eine Gas–Elektronenvervielfachungsfolie hinzugefügt werden, um die Betriebssicherheit zu erhöhen.

Der äußere Teil der Spurkammer des Compact Muon Solenoid (CMS) Experimentes des zukünftigen Large Hadron Colliders (LHC) am Centre de Recherche Nucléaire (CERN) sollte mit MSGCs ausgestattet werden. In der zentralen Spurkammer sollten einfache MSGCs verwendet werden. Für den Vorwärts und Rückwärtsteil war MSGC+GEM Technologie vorgesehen.

Diese Arbeit beschreibt den Bau und Test einer Vorserie von 18 voll funktionsfähigen MSGC+GEM Vorwärtsmodulen, deren Strahlenhärte und Tauglichkeit zur Massenproduktion getestet werden sollte. Fünf der Module wurden in Aachen gebaut, weitere 13 im 'Institut für Experimentelle Kernphysik' in Karlsruhe.

Für die beschriebene Vorserie wurden zwei verschiedene Gem–Typen verwendet: 17 Folien wurden in einem Naßätzverfahren (in einer Werkstatd des CERN) hergestellt, was zu einer doppelt konischen Lochform führte. Eine Folie wurde mit einem Plasmaätzverfahren (von der Firma Würth Elektronik) hergestellt, was zum Überätzen der Löcher führte.

1999 war es nicht klar, ob die Technologien der MSGC und MSGC+GEM der hohen Strahlenbelastung am LHC gewachsen waren. Um die Strahlenhärte der 18 Module zu testen, wurden sie zum Paul Scherrer Institut gebracht und dort in dem sogenannten 'mf2 milestone' für 376 Stunden unter LHC Bedingungen bestrahlt zu werden.

16 der Detektoren waren von ausreichender Qualität, um an dem Milestone teilzunehmen. Sie konnten über die 376 Stunden Strahlzeit stabil betrieben werden. Dabei wurden weniger als 0,14% der Auslesestreifen beschädigt. Daraus kann man eine reduzierte Ortsauflösung in weniger als 5% der aktiven Detektorfläche nach 10 Jahren Betrieb am LHC voraussagen. So konnte gezeigt werden, daß die MSGC+GEM Technologie für den Einsatz im CMS Experiment geeignet ist.

Die fünf in Aachen gebauten Module, unter ihnen die Kammer mit der überätzten GEM, wurden in einem weiteren Test im Labor untersucht. Ihre Uniformität wurde untersucht, um festzustellen, ob eine Massenproduktion von MSGC+GEMs realistisch ist. Außerdem wurde die Pulsformung und Tranzparenz der Detektoren in den drei Gasmischungen Ne/DME, Ar/CO_2 und Ne/DME/CO_2 untersucht. Dabei wurde festgestellt, daß lediglich die überätzte Folie in allen drei Gasmischungen unter optimalen Bedingungen betrieben werden kann. Für die doppelt konischen GEMs muß ein schnelles Gas wie Ar/CO_2 benutzt werden, um mit der verwendeten Ausleseelektronik auf dem Transparenzplateau arbeiten zu können. Außerdem wurden verschiedene Probleme, die bei einer Massenproduktion von Detektoren auftreten können, identifiziert, so daß in Zukunft Lösungen erarbeitet werden können.

Auch wenn die MSGC+GEM Technologie nicht im CMS Experiment eingesetzt werden wird, beweist diese Arbeit, daß die Detektoren für den Einsatz an derartigen großflächigen Hochratenexperimente geeignet sind.

Abstract

Micro strip gas chambers (MSGCs) are promising candidates for large scale applications. They combine a good spatial resolution with high granularity and low cost. As a possible extension of the plain MSGC, a Gas Electron Multiplier (GEM) foil may be implemented into the detector in order to increase the safety of operation.

It was planned to equip the outer part of the tracking system of the Compact Muon Solenoid (CMS) experiment at the future Large Hadron Collider (LHC) at the Centre de Recherche Nucléaire (CERN) with MSGCs. In the barrel part of the tracker, plain MSGCs were to be used. For the forward part, the MSGC+GEM technology was envisaged.

This thesis describes the assembly and test of a pre–series of 18 fully functional MSGC+GEM forward detector modules to determine their radiation hardness and their readiness for mass production. Five of the modules were built at Aachen, thirteen more at the 'Institut für Experimentelle Kernphysik' in Karlsruhe.

For the pre–series, two different types of GEM foils were used: 17 foils were wet etched (by a workshop at CERN) in a procedure that resulted in double conical holes. One foil was plasma–etched (by Würth Elektronik GmbH) which has lead to an underetching of the GEM–holes.

In 1999 it was not clear, whether the MSGC or MSGC+GEM technology are suited to withstand the high rate irradiation at the LHC. To test the radiation hardness of the 18 modules, they were taken to the the Paul Scherrer Institut to be irradiated for 376 hours under LHC–like conditions in the so–called 'mf2 milestone'.

16 of the detectors were found to be of good quality and were chosen to participate in the milestone. They showed stable operation during the 376 hours of irradiation, loosing less than 0.14% of the readout strips. This can be extrapolated to a degradation of spatial resolution in less than 5% of the active surface of the CMS outer tracker within 10 years of operation. Thus it could be shown that the MSGC+GEM technology is well suited for the operation in CMS–like experiments.

The five Aachen–built modules, among them the one with the underetched GEM, have further been tested in a laboratory experiment. There the uniformity of the detectors was determined in order to find out whether a mass production of MSGC+GEMs is feasible. In addition, signal shaping and transparency were measured in different gas mixtures, namely Ne/DME, Ar/CO_2 and $Ne/DME/CO_2$. It was found that only the underetched foil can be operated under optimal conditions with all gas mixtures under test. For the double conical GEM, a fast gas like Ar/CO_2 is required in order to operate on the transparency plateau with the readout electronics used. Finally, several problems that may arise in a detector mass production were identified so that solutions can be found in the future.

Even though the MSGC+GEM technology was rejected for the CMS experiment, this thesis proves that the detectors are suited to equip large scale, high rate experiments.

Contents

Chapter 1

Preface

This thesis deals with the micro strip gas detector technology with gas electron multipliers (MSGC+GEM) envisaged for the outer forward tracker of the CMS[1] experiment at the future LHC[2] collider at CERN[3]. Their readiness for mass production, high rate capability and transparency will be investigated.

The LHC collider and the CMS experiment will be introduced and described in chapter 2. To equip the CMS outer forward tracker, several thousand detector modules are required. They have to be manufactured and mounted in a mass production during several years.

After an introduction to the principle of the detector technology in chapter 3, the assembly of a pre-series of MSGC+GEMs will be described in chapter 4. Five fully operational modules have been built in Aachen using GEM foils from two different manufacturers. The state of readiness and remaining needs for an MSGC+GEM mass production will be discussed in that chapter.

The CMS tracker will be exposed to high rate irradiation. Thus all tracker components have to be radiation hard. The robustness and high rate behaviour of the five Aachen–built detectors have been studied in a hadron beam test together with 13 modules of a pre–series assembled in Karlsruhe. The results of this so–called "mf–2"[4] test will be presented in chapter 5.

In chapter 6, some of the various working parameters that have to be optimised within an MSGC+GEM, will be studied. Especially, the impact of the drift field on the ballistic coefficient and GEM transparency will be addressed. Consequences for the detector uniformity will be discussed.

In the final chapter, conclusions will be drawn.

[1] **C**ompact **M**uon **S**olenoid
[2] **L**arge **H**ardon **C**ollider
[3] Conseil Europeen pour la Recherche Nucléaire
[4] **m**ilestone **f**orward number 2

Chapter 2

Introduction to LHC and CMS

2.1 The standard model of high energy physics

High energy physics is the science dealing with the fundamental constituents of matter. In the standard model of high energy physics [1], quite a few such particles have been identified. Today, 3 families of fermions (and antifermions) are known, each consisting of a quark and a lepton doublet:

$$Quarks: \begin{pmatrix} u \\ d \end{pmatrix} \begin{pmatrix} c \\ s \end{pmatrix} \begin{pmatrix} t \\ b \end{pmatrix}$$

$$Leptons: \begin{pmatrix} \nu_e \\ e \end{pmatrix} \begin{pmatrix} \nu_\mu \\ \mu \end{pmatrix} \begin{pmatrix} \nu_\tau \\ \tau \end{pmatrix}$$

Theses particles interact through the exchange of gauge bosons. Up to now four types of interactions and the corresponding particles have been postulated:

interaction	gauge boson	mass
gravitational	graviton h	0
strong	gluons g	0
weak	$W^{\pm}$	$\approx 80\ GeV/c^2$
	Z^0	$\approx 91\ GeV/c^2$
electromagnetic	photon γ	0

The latter three of these interactions are described by the standard model of high energy physics. It is based on the demand of local gauge symmetry under the symmetry group of $SU(3) \times SU(2)_L \times U(1)$. However, this leads to massless gauge bosons while the Z^0 and $W^{\pm}$ are massive. Their masses are introduced through spontaneous symmetry breaking by the higgs mechanism. As a consequence, the higgs boson H has to be added to the standard model. Alike the masses of the other particles, the higgs mass cannot be predicted. Once the higgs boson has been found, it's mass has to be measured. Demanding that the theory remains renormalizable, a theoretical upper limit of the order of $1\ TeV/c^2$ for the higgs mass can be set [2].

The higgs boson is the only particle predicted by the standard model that has not yet been observed. Alas, hints of a higgs with a mass of around 115 GeV/c^2 have been seen during the last year of running at the LEP[1] collider at CERN[7].

In the past years, the standard model has been very successfull in describing and predicting the results of various experiments [3]. Even high precision measurements are in good agreement with standard model predictions. Still there are a few subjects under investigation. The higgs boson has yet to be discovered. A second matter of ongoing research is the so–called CP violation.

Despite it's tremendous success, the standard model leaves some questions unanswered. For example it offers no reason why exactly three fermion families exist. Another pending problem is that of the hierarchy of masses between the generations of quark and lepton families. Thus extensions of the standard model are investigated.

A favored approach to 'new physics' are the theories of SUSY[2]. Within these, each standard model particle has a supersymmetric partner thus doubeling the number of particles. Still up to now, no experimental evidence for SUSY could be found.

To answer the remaining questions in the standard model or find evidence for new physics, further high energy experiments have to be built and carried out. One of these is the LHC.

2.2 The Large Hadron Collider

The LHC accelerator is currently being installed into the old LEP tunnel and shall be finished until 2006. It has been decided to use the LEP facilities in order to reduce the enormous cost of the collider project. An overview over the LHC collider is given in figure 2.1.

The LHC ring is meant to store protons or heavy ions. For this thesis, only the pp[3] project is of interest and will be summarised in the following. The production cross section of some characteristic processes in pp collisions can be seen in figure 2.2. For example, the $b\bar{b}$ production has a very high cross section so that it will be possible to study b physics with good statistics. The same is true for top quarks that will be produced at a higher rate than at any other experiment.

The main design parameters for LHC are listed in table 2.1. There it can be seen that the center of mass energy in the pp collisions will be 14 TeV. However, a proton is composed not only of three quarks but also contains virtual sea quarks and gluons. The proton momentum is shared between all constituents. Thus the effective collision energy will be about 1 TeV.

Four experiments will be installed at the interaction points (see also figure 2.1):

- A Toroidal LHC Apparatus (ATLAS)
- Compact Muon Solenoid (CMS)
- LHCb

[1] **L**arge **E**lectron Positron **C**ollider, that has been running until November 2000
[2] **SU**per**SY**mmetry
[3] **p**roton–**p**roton

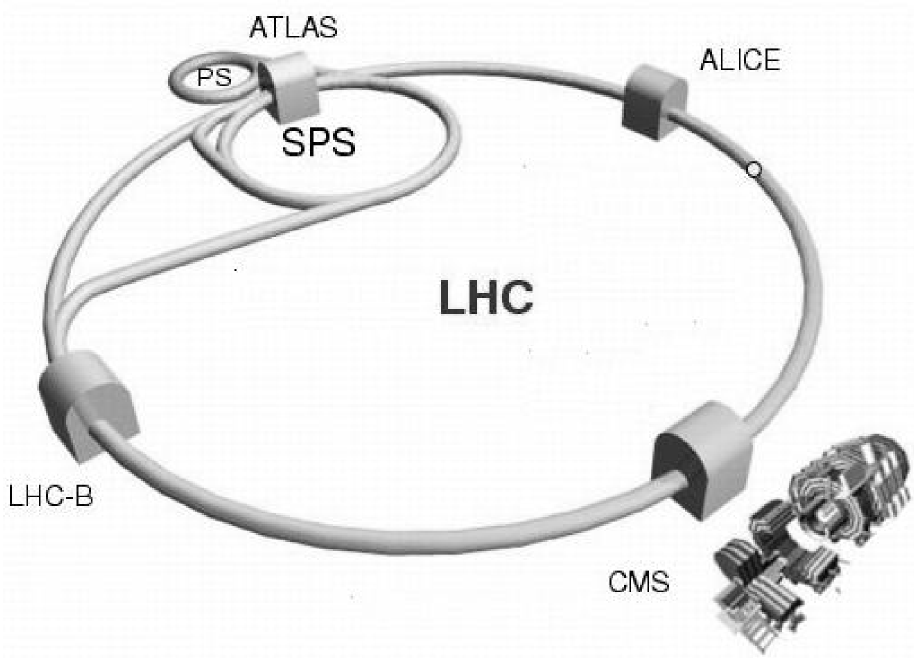

Figure 2.1: The LHC collider and it's four experiments.

particles	protons
beam energy	7 TeV ($\sqrt{s} = 14TeV$)
circumference	26.7km
interaction points	4
luminosity	$10^{34}\ cm^{-2}s^{-1}$
bunch crossing frequency	40 MHz
particles per bunch	10^{11}
pp collisions per b.c.	≈ 20 (inelastic)
crossing angle	200 μrad
bunch length	7.5 cm
beam radius	16 μm
luminosity lifetime	10 h

Table 2.1: The main LHC design parameters.

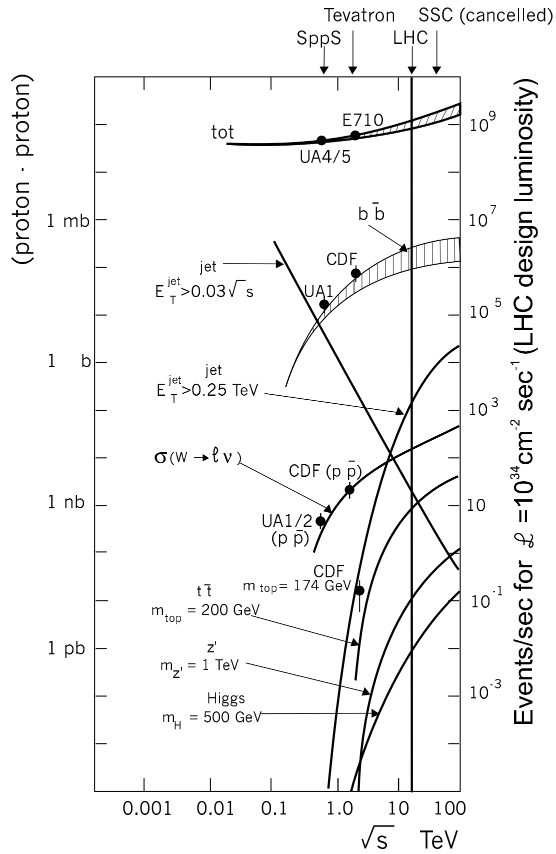

Figure 2.2: The production cross sections of some characteristic processes in pp collisions as a function of the center of mass energy. For comparison, the LHC energy is marked together with other accelerators.

- A Large Ion Collider Experiment (ALICE)

ATLAS and CMS will be general purpose detectors competing e.g. for the discovery of the higgs boson. They will also search for 'new physics' like the predicted supersymmetric particles. LHCb is designed to study CP violation in the b–quark sector, whereas ALICE will concentrate on heavy ion collisions and the study of the quark–gluon plasma.

2.2.1 Searching for the higgs boson at LHC

The main reason to propose the LHC has been the search for the higgs boson. At the beginning of the LHC project, the experimental constraints on the higgs mass have been very weak. Thus the collider was designed to be able to produce the boson up to the theoretical limit of $m_H = 1\ TeV/c^2$. Today the higgs mass in the standard model is constrained mainly by the LEP experiments to $114.1\ GeV < m_H < 196\ GeV$ (95 % confidence level [7]). The lower limit is derived from the direct search, whereas the the upper limit can be determined by measuring radiative corrections in electroweak interactions.

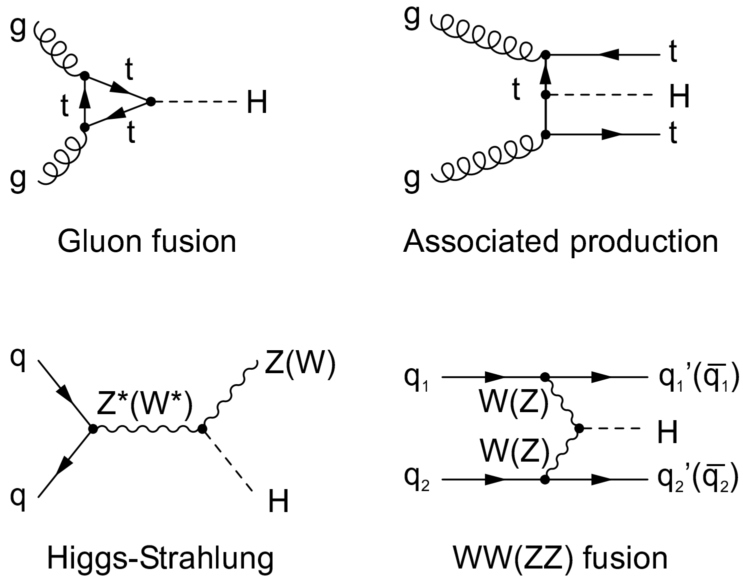

Figure 2.3: Feynman graphs of the most important higgs production processes.

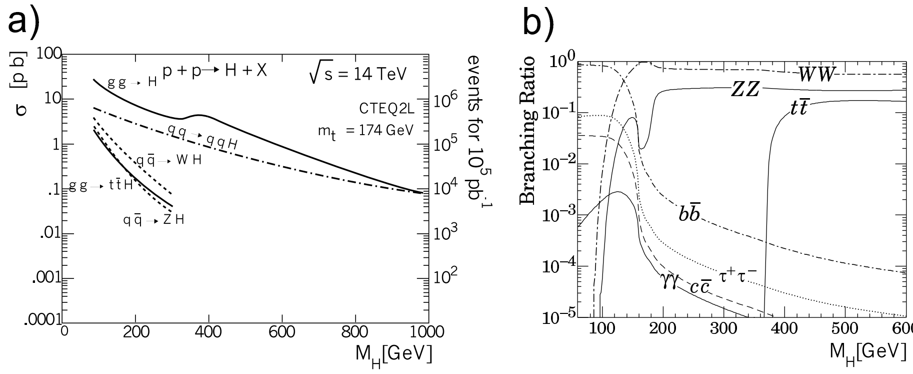

Figure 2.4: Higgs production cross section (a) and branching ratio (b) [25]

In figure 2.3, the four processes that are most important for the higgs production at LHC can be seen. Figure 2.4 (a) shows the corresponding production cross sections. Obviously, these cross sections are very small. Thus a collider with high luminosity is needed to find the higgs boson. This was the main motivation to choose the LHC design luminosity as high as possible.

In fiugre 2.5, the most important decay modes of the higgs boson are shown. The corresponding branching ratios can be seen in figure 2.4 (b). For low higgs mass, the main decay channel is into a $b\bar{b}$. If the higgs mass is above the thresh-

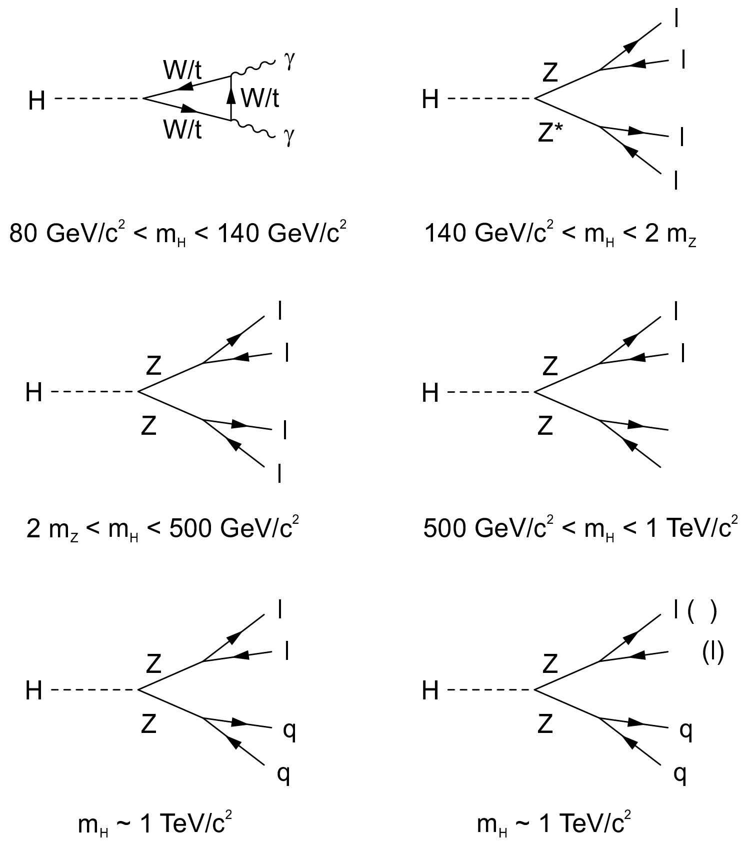

Figure 2.5: Feynman graphs of the favoured higgs decay modes for higgs masses between 80 GeV/c^2 and 1 TeV/c^2. The indicated leptons are either electrons or muons. The $H \rightarrow \tau\bar{\tau}$ decay is not easily detectable, because the τ leptons mostly decay into hadron jets that are not easily distinguished from the huge background.

old for WW and ZZ productions, these processes become dominant. However, the decays with the highest branching ratio do not necessarily coincide with the favored discovery channels. For example for $m_h < 140 GeV/c^2$, the favored decay is the one into two photons, since it leaves a very clear signature of two back–to–back photons in the detector. The decay into $b\bar{b}$ on the other hand has a large branching ratio but is hard to isolate due to enormous background. Especially around 20–25 minimum bias events per bunch crossing make the b–tagging difficult.

2.3 The Compact Muon Solenoid

As mentioned before, CMS is designed as a multi purpose experiment. Thus it's task will be to correctly identify the products of pp interactions and measure their momenta and energies. As can be seen in figure 2.6, CMS will consist of

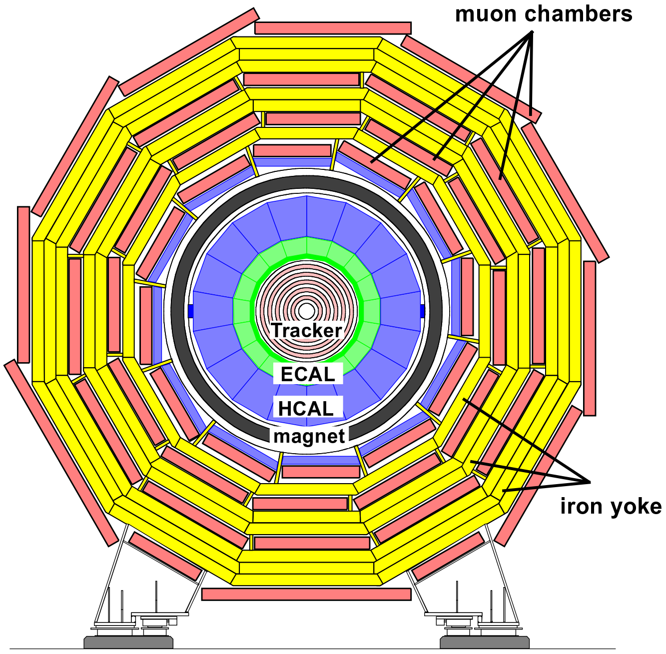

Figure 2.6: Cross section of the CMS detector. [27]

the following components (from outside inwards):

- muon chambers
- 4 Tesla solenoid
- hadronic calorimeter
- electromagnetic calorimeter
- tracking system

The whole CMS experiment will be 21 m long and 15 m in diameter at a weight of 12500 t. The size of it's components can be seen in figure 2.7.

The muon chambers will be outside the magnet with the iron return yoke spaced in between. In this way the detectors will be within a magnetic field of 2.5 Tesla. The calorimeters will be placed inside the magnet so that no additional material will reduce the precision of the energy measurement. The tracking system will be the innermost part of the detector.

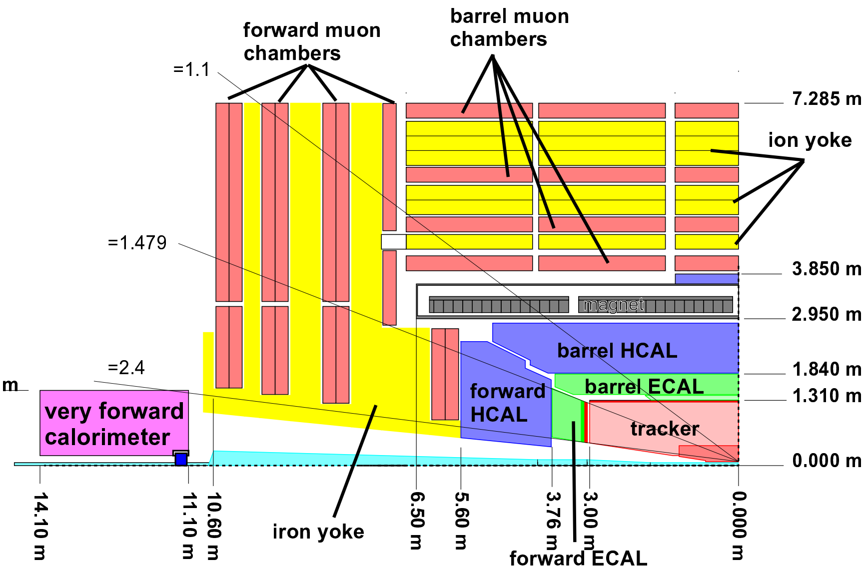

Figure 2.7: r–ϕ cross section of one quarter of the CMS detector. [27] The collision point is in the bottom right hand corner.

The magnetic field within the tracker and the muon system will be needed to measure particle momentum and charge through the curvature of the tracks.

Each component of the CMS detector will be divided into two forward parts that will detect tracks of higher pseudorapidity[4] η and a barrel part for tracks with lower η (see figure 2.7). In the following subsections, the various components of the CMS detector will be described.

2.3.1 The muon system

Because the higgs boson decays into four leptons over a vast energy interval, the muon system will be an important part of CMS.

As mentioned before, the muon system is placed within the iron yoke. The resulting 2.5 Tesla magnetic field allows a measurement of the muon momentum. The transverse momentum resolution $\Delta p_t/p_t$ will be between 8 % and 40 % for 10 $GeV/c^2 < p_t < 1\ TeV/c^2$ muons. An even better result can be achieved if the information from the central tracker is combined with the muon system. In that case the momentum resolution is $0.5\ \% < \Delta p_t/p_t < 20\ \%$.

Three different technologies will be used within the muon system:

drift tubes In the barrel part, three stations of drift tubes with twelve layers each will be implemented. They will be operated with Ar/CO_2

cathode strip chambers In the forward part of the tracker, two stations with six layers of cathode strip chambers on each side will be used. The counting gas will be $Ar/CO_2/CF_4$.

[4] $\eta = -ln\left(tan\frac{\theta}{2}\right)$ where θ is the scattering angle.

resistive plate chambers (RPCs) One RPC–layer will be added to each station in both parts of the muon system. This technology was chosen because of the good time resolution so that the RPCs can be used as a muon trigger.

2.3.2 The calorimeter system

The calorimeter system will be divided into a hadronic calorimeter (HCAL) and an electromagnetic calorimeter (ECAL).

The HCAL is designed to measure the energy of hadron jets. It will consist of alternating layers of copper plates and plastic scintillators. A fine segmentation will be required in order to separate jets. The energy resolution will be about $\Delta E/E = 100$ % for $30GeV < E < 1TeV$. The HCAL will be the only component of the CMS experiment that does not only consist of a forward and a barrel part. In addition a very forward calorimeter will be added to cover a pseudorapidity range up to $|\eta| < 5.3$.

The ECAL will determine the energy of leptonic and photonic showers. After the possible observation of a 115 GeV higgs at LEP, the energy measurement of photons has gained even higher importance since the favored discovery channel for a higgs of that mass is the one into two photons. Those can only be detected in the ECAL.

The calorimeter will consist of lead–thungstate crystals ($PbWO_4$). The energy resolution will be $\Delta E/E$=0.7 % for electrons or photons of 120 GeV which will be necessary in order to detect the higgs signal in the huge background of the $H \rightarrow \gamma\gamma$ decay channel.

2.3.3 The tracker

The design of the CMS tracker has gone through large modifications since the TDR[5] [27] was written in 1998. This thesis deals with the MSGC[6] technology which will no longer be implemented into the tracker due to a decision in december 1999. Thus the old TDR layout will be described in this section and the recent modifications will be mentioned briefly in the end.

The main task of the tracker is the correct identification and separation of tracks and the momentum measurement of charged particles. The identification of lepton tracks in combination with the muon system is of special importance to detect the higgs decay into two W or Z bosons. In addition, the separation of hadron jets and vertex measurements has to be accomplished within the tracker.

In the old design, the tracker consisted of three types of detectors with different technologies: silicon pixel–, silicon strip– and micro strip gas detectors. For the so–called 'inner tracker', semiconductor technology has been envisaged.

The high irradiation rate in the inner tracker poses a great challenge. To limit radiation damage as well as leakage current within the modules, the whole silicon tracker will have to be operated below -10^o C during the 10 years of CMS operation. MSGC technology was envisaged for the outer tracker.

[5] **T**echnical **D**esign **R**eport
[6] **M**icro **S**trip **G**as **C**hamber

The high interaction rate at LHC leads to a vast track multiplicity. Consequently, the detectors used in the tracker need a high granularity and good time and spatial resolution. This requirement holds for all three components in order to limit the occupancy[7] to a few % per readout channel.

In addition, the whole tracker should contain as little material as possible so that it does not disturb the energy measurement. This is of special importance for the detection of the $H \rightarrow \gamma\gamma$ decay. In order to increase the sensitivity in that channel, the probability that either photon converts should be below 50 %.

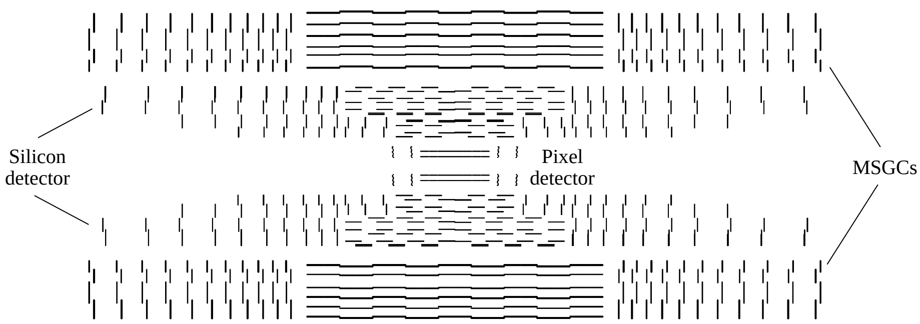

Figure 2.8: Cross section of the CMS tracker where the three different components can be seen. [27]

The layout of the tracker as it is in the TDR can be seen in figure 2.8. The whole tracker will be about 2.6 m in diameter and 6 m long. It's components will be described in the following:

The pixel system For the innermost part of the tracker, silicon pixel detectors will be used. The special importance of this part lies in vertex identification and b–tagging. Since the minimum bias events form a vast background in the pixel tracker, an especially high granularity is required ruling out the simpler strip detectors this close to the beam pipe.

The cell size of the pixels will be 150×150 μm at a thickness of 250 μm. With these detectors, a spatial resolution at the 10–15 μm level can be achieved. The pixel system will consist of three layers in the barrel– and two in the forward–region.

The silicon strip tracker The pixel system will be followed by 300 μm thick silicon strip detetors. The barrel region will be composed of 5 layers of modules and 6 mini–disks. The forward region will contain 10 disks in each endcap.

A single hit resolution of better than 20 μm is required in the r–ϕ coordinate whereas 500 μm is sufficient in the z coordinate. Obviously, any micro strip detector provides only one impact coordinate, r–ϕ in the barrel region and ϕ in the forward region respectively. To obtain the missing coordinate, some of the rings will be be equipped with two modules mounted back to back, one module tilted by a stereo angle of 100 mrad.

[7]Number of hits per trigger.

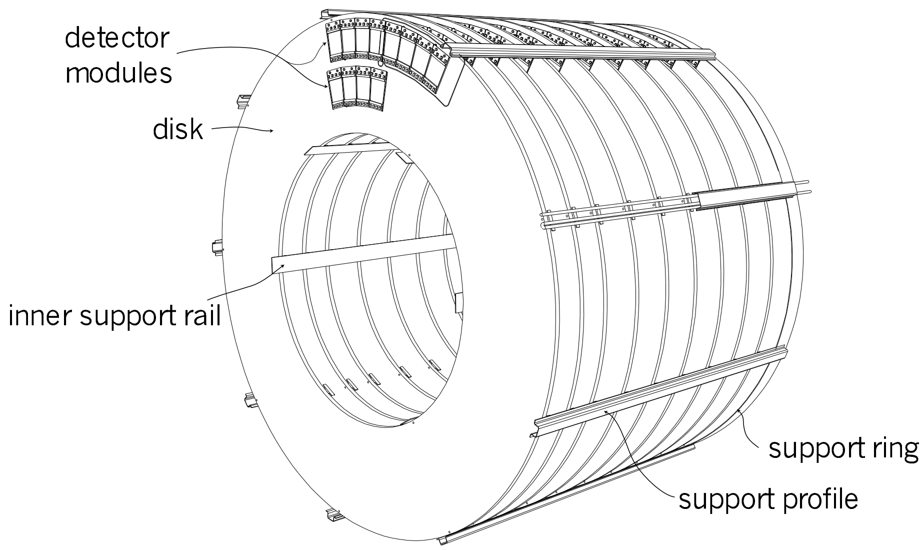

Figure 2.9: The forward MSGC tracker with some modules already mounted [27]. Only two rings can be seen in this perspective since the other rings are mounted on the back side of the disk.

The MSGC tracker The MSGC tracker was meant to consist of 6 rings of detectors in the barrel part and 11 disks in each forward region. It would have reached from $r > 675\ cm$ to $r = 1233\ cm$ and $1215\ cm < z < 2760\ cm$.

A single hit resolution of less than 50 μm would have been achieved in the coordinate perpendicular to the strips. The impact information parallel to the strips would have been obtained in a similar way as for the silicon strip tracker. Some of the rings would have been built of two modules mounted back to back, one tilted by a stereo angle of 50 mrad. This leads to a resolution of $\approx 1\ mm$ parallel to the strips which is sufficient.

Each forward disk would have been equipped with four concentric rings of banana–like shaped MSGC detector modules with the strips pointing towards the beam pipe. A scheme of the forward MSGC tracker can be seen in figure 2.9. In the scheme, only two of the four rings are visible, since the other two are mounted on the back side of the disk. The layout of a single forward detector module will be discussed in chapter 4. As counting gas Ne/DME[8] was foreseen.

In spring 1999 it was decided not to use plain MSGCs in the forward part of the detector. Instead the MSGC+GEM[9] technology was envisaged that will be described in chapter 3.3.

[8] **Di** **M**ethyl**E**ther
[9] **G**as **E**lectron **M**ultiplier

The new tracker design

In December 1999 it was decided to implement a full silicon tracker into the CMS experiment. This decision leaves the inner tracker essentially undisturbed while the outer tracker is replaced by five barrel rings and nine forward disks of 500 μm thick silicon strip detectors. Therefore, the whole support structure and cooling system had to be redesigned [28] in order to keep the whole tracker at $-10^o\ C$.

Chapter 3

Micro Strip Gas Detectors and Gas Electron Multipliers

MSGC+GEM detectors are proportional counters that divide the avalanche amplification between micro strips and GEM in order to increase the safety of operation.

The following chapter will give an overview over the main properties of these devices. In section 3.1, the principle of ionisation and amplification in gases will be explained. In section 3.2 and 3.3, the properties of MSGC and GEM technology will be discussed.

3.1 Gaseous detectors

Before discussing the MSGC+GEMs in detail, a general overview over gas detectors will be given within this section. Essentially, a gaseous detector is a volume filled with a counting gas in an electric field. Traversing particles ionise the gas atoms. The produced electrons and ions drift towards the electrodes that set up the electric field. Normally the electrons are multiplied in an avalanche process near the detector anodes and collected to form the detector signal.

Since only charged particles have been used for the detector tests described in this thesis, only their detection will be discussed. A complete and more detailed description of the theory of gas counters can be found in [4, 5]. Here only the main results of these references are summarised.

3.1.1 Ionisation processes

When charged particles traverse a gaseous detector, they ionise some of the atoms in the counting gas, producing electron–ion pairs.

In addition to the primary ionisation described above, the electrons that are liberated by the traversing particles may carry enough energy to ionise gas molecules as well. This is called secondary ionisation.

The maximum kinetic energy E_{max} that can be passed to a liberated electron depends on the incident mass and velocity of the particle:

$$E_{max} = \frac{2m_e c^2 \beta^2 \gamma^2}{1 + \frac{2\gamma m_e}{m} + \left[\frac{m_e}{m}\right]^2} \tag{3.1}$$

with:

m_e	= electron mass
m	= mass of traversing particle
c	= velocity of light
$\beta c = v$	= velocity of the traversing particle
γ	$= \frac{1}{\sqrt{1-\beta^2}}$

For massive incident particles with $\left(\frac{m_e}{m}\right)^2 << 1$ (being a valid assumption for all charged particles except electrons) this relation can be approximately written as:

$$E_{max} = \frac{2m_e c^2 \beta^2 \gamma^2}{1 + \frac{2\gamma m_e}{m}}$$

For electrons ($m = m_e$) (3.1) can be approximated as:

$$E_{max} = E - m_e c^2$$

The mean energy loss of a particle with $m >> m_e$ in a medium can be described by the Bethe–Bloch formula:

$$-\frac{dE}{dx} = \frac{4\pi\alpha^2\hbar^2 z^2 NZ}{m_e \beta^2} \left(ln \frac{2m_e v^2 \gamma^2}{I} - \beta^2 - \frac{\delta(\beta)}{2} \right) \tag{3.2}$$

with:

x	= thickness of the traversed medium
α	= fine structure constant
$2\pi\hbar = h$	= Planck constant
ze	= charge of traversing particle
N	= atomic density in the traversed medium
Z	= atomic number of the traversed medium
I	= effective ionisation potential (a good approximation is $I = 16\ Z^{0.9}\ eV$)
$\delta(\beta)$	= so–called density effect that reduces the relativistic rise for $\beta \approx 1$

In the case of traversing electrons, the following slightly modified equation gives a good approximation for $\frac{dE}{dx}$.

$$-\frac{dE}{dx} = \frac{4\pi\alpha^2\hbar^2 z^2 NZ}{m_e \beta^2} \left(ln \frac{\gamma m_e c^2}{2I} - \beta^2 - \frac{\delta^*(\beta)}{2} \right) \tag{3.3}$$

For thin detectors, the total energy loss of the detected particle can be approximated by:

$$\Delta E = \frac{dE}{dx}x$$

where x is the detector thickness.

The mean energy loss of protons, muons and electrons can be seen in figure 3.1. For low particle energy $\frac{dE}{dx}$ is approximately proportional to $\frac{1}{E}$ whereas for high energies the logarithmic increase of a relativistic particle dominates in gases (see equation 3.2 and 3.3). Between the two extremes, the energy loss distribution has a wide minimum around $\beta\gamma \approx 4$. Relativistic particles with $\beta \approx 1$ and an energy loss around that minimum are called MIPs[1].

Examples for the minimum of $\frac{dE}{dx}$ for some absorbers can be found in table 3.1.

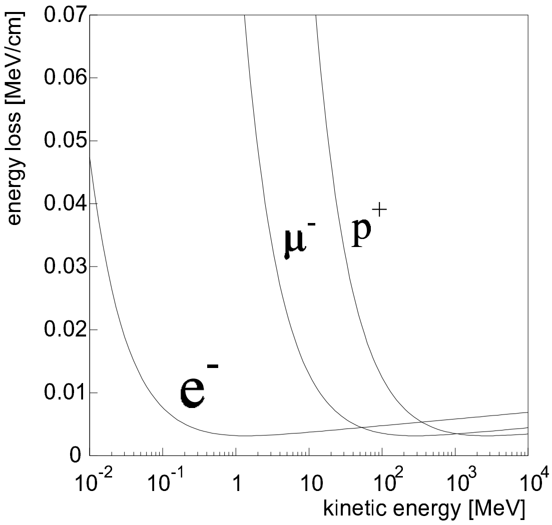

Figure 3.1: Mean energy loss of charged particles in argon gas. [29]

absorber	$\frac{dE}{dx}_{min} \left[\frac{MeV}{cm}\right]$
Nitrogen	$2.3 \cdot 10^{-3}$
Oxygen	$2.3 \cdot 10^{-3}$
Neon	$1.56 \cdot 10^{-3}$
Silizium	1.66
Argon	$2.69 \cdot 10^{-3}$
$C_2H_6O(DME)$	$3.9 \cdot 10^{-3}$
CO_2	$3.62 \cdot 10^{-3}$

Table 3.1: The minimum energy loss for several absorbers.

[1]**M**inimum **I**onising **P**articles

For gas mixtures, the total energy losses of the constituents have to be summed up:

$$\frac{dE}{dx} = \sum_i f_i \frac{dE}{dx}|_i$$

with:

f_i = relative fraction of constituent i
$\frac{dE}{dx}|_i$ = mean energy loss of constituent i

Attachment

The number of primary charges may be reduced when electrons are absorbed by gas molecules producing negative ions. This process is called (associative) attachment. The molecule may even be broken in this process (dissociative attachment). In any case, the attached electron is lost for the detector signal.

The attachment rate can be expressed by the so–called attachment coefficient A. In a constant drift field, the loss L of primaries can be calculated as:

$$L = 1 - e^{-D \cdot A}$$

where D is the drift path.

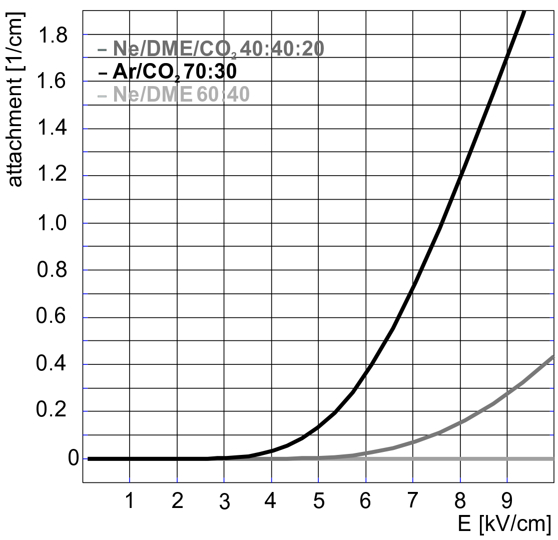

Figure 3.2: Dependence of the attachment coefficient on the electric field for the three gases that will be used in this thesis [23]

For the gases used in this thesis, the attachment coefficients can be seen in figure 3.2. Obviously, attachment plays no role for Ne/DME. For the gas mixtures that include CO_2, it becomes important at high electric fields. For example in the Ar/CO_2 gas mixture 10 % of the primary electrons are lost due to attachment at a field of 6 kV/cm over a drift distance of 3 mm.

3.1.2 Statistical fluctuations

The energy loss of a particle in an absorber shows statistical fluctuations. This is of special importance in thin gaseous detectors where the number of primary ionisations is small.

The Landau theory provides the means to calculate the energy loss fluctuations. An approximation for the resulting so–called Landau distribution [6] is:

$$L(\lambda) = \frac{1}{\sqrt{2\pi}}\, exp\left[-\frac{1}{2}\left(\lambda + e^{-\lambda}\right)\right]$$

with λ being the deviation of the most probable energy loss from the real energy loss:

$$\lambda = \frac{\Delta E^{real} - \Delta E^{m.p.}}{\xi}$$

with:

ΔE^{real}	= real energy loss
$\Delta E^{m.p.}$	= most probable energy loss
ξ	$= \frac{2\pi\alpha^2\hbar^2 z^2 NZ}{m_e\beta^2}\rho x$
ρ	= absorber density
x	= absorber thickness

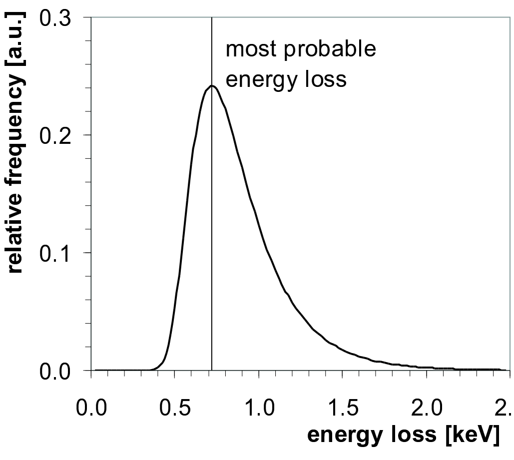

Figure 3.3: Energy loss distribution of a minimum ionising muon in 3 mm of argon gas [14].

It can be seen in figure 3.3 that the energy loss is not symmetric. The tail in the Landau distribution is mainly caused by so–called δ–electrons that gained a high energy during the primary interactions. These electrons carry enough energy to cause secondary ionisations.

3.1.3 Diffusion and drift

Diffusion

Electrons and ions that are created in a gas rapidly loose their energy and get thermalised, resulting in a Maxwell–Boltzmann distribution:

$$F(\epsilon) = const \cdot \sqrt{\epsilon}\ exp\left(-\frac{\epsilon}{kT}\right)$$

with:

ϵ	= mean particle energy
k	= Boltzmann factor
T	= temperature [K]

The thermal movement of the charge causes diffusion that leads to a gaussian charge cloud whose size increases in time:

$$\frac{dN}{N} = \frac{1}{\sqrt{4\pi Dt}}\ exp\left(-\frac{x^2}{4Dt}\right) dx$$

with:

$\frac{dN}{N}$	= fraction of charge in dx after the time t
D	= diffusion constant of the gas

Drift in an electric field

In an electric field, electrons and ions will drift along the field lines between collisions. The electrons drift towards the anodes while the ions move towards the cathodes. However, electrons and ions have to be treated differently due to their very different masses.

The ions have a very large mass. Thus their drift is not influenced much by collisions with the gas atoms. Therefore the ion drift velocity is constant:

$$\vec{v}_{Drift} = \mu \vec{E} \frac{p}{p_0}$$

with:

$\mu(\epsilon)$	= mobility of the drifting particle
$\vec{E}$	= electric field
$\frac{p}{p_0}$	= pressure in the counting gas relative to atmospheric pressure

Examples for the mobility of some ions in different gases can be seen in table 3.2.

gas	ion	$\mu\ \left[\frac{cm^2}{Vs}\right]$
Neon	Ne^+	4.14
Argon	Ar^+	1.4
$C_2H_6O(DME)$	DME^+	0.56

Table 3.2: Mobility of ions in some gases at atmospheric pressure.

For electrons all information about the previous drift is lost during a collision with a gas atom. After the collision, the drift along the electric field will be reinitiated. The electron drift velocity thus depends strongly on the time between two collisions. It is up to three orders of magnitude larger compared to ions:

$$\vec{v}_{Drift} = \frac{e}{m}\vec{E}\tau(\vec{E},\epsilon)$$

with:

$\tau(\vec{E},\epsilon)$ = mean time between collisions depending on the electric field and the energy of the particle.

Measured and simulated drift velocities of electrons in several gases can be seen in figure 3.4.

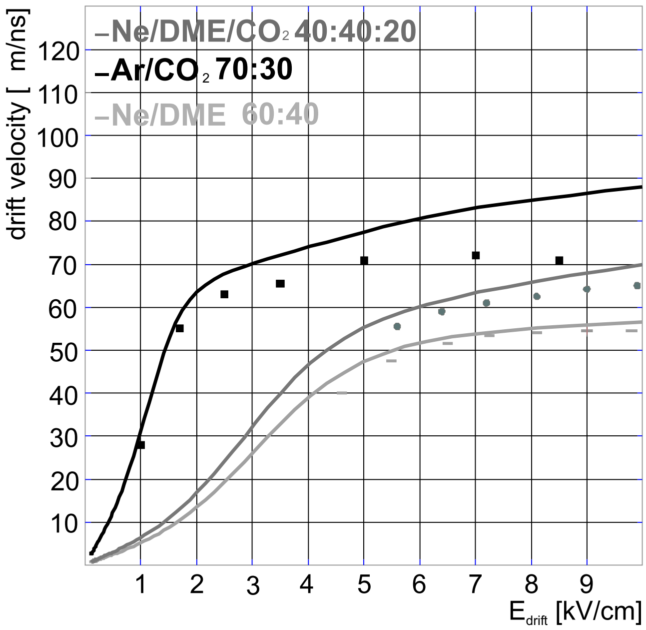

Figure 3.4: Dependence of the drift velocity on the electric field for the three gas mixtures that will be used in this thesis. The dots are measured data while the lines were obtained in simulations. [8]

3.1.4 Gas amplification

Besides the primary and secondary ionisation in the drift volume, an avalanche process near the electrodes is used to amplify the signals of traversing particles in proportional counters. That process is briefly described in this section.

The simplest kind of proportional counter is a wire chamber, where the field increases proportional to the inverse radius close to the wire. When the primary and secondary electrons approach a critical distance d_{crit} from the wire, an avalanche of electron–ion pairs is initiated. Each electron ionises gas atoms near the wire. Due to the high field, the liberated electrons can start another generation of ionisations. All avalanche electrons are finally collected by the anode wire thus ending the amplification process.

In principle the same procedure is used in modern micro pattern detectors like MSGC+GEMs. Here, the avalanches are created within the GEM foil and on the MSGC substrate (see sections 3.2 and 3.3).

The amplification of an avalanche is given by the number of electron–ion–generations whereby each generation doubles the number of charge pairs. The number Z of generations for a single initiating electron is given by:

$$Z = \frac{U_{anode} - U(d_{crit})}{\Delta V}$$

with:

$U_{anode} - U(d_{crit})$	= potential difference between anode and d_{crit}
ΔV	= average ionisation potential

Obviously, the amplification $\overline{M}$ in the avalanche process is given by:

$$\overline{M} = \frac{N}{N_0} = 2^Z$$

where N_0 is the sum of primary and secondary electrons and N is the number of electrons in the avalanche.

Alike the primary ionisation, the charge amplification by the avalanche is statistical. It can be described by a so–called Polya distribution $p(k)$ [4]:

$$P(M) = \frac{p(M/\overline{M})}{\overline{M}}, \quad p(k) = \frac{m(mk)^{m-1}}{\Gamma(m)} exp\,(-mk)$$

with:

m	= field dependent constant
$\overline{M}$	= average gas gain
M	= real gas gain
Γ	= gamma function

If the gain near the electrodes exceeds a certain limit, so–called self–quenched streamers may develop. They are initiated when UV photons are created within the avalanche and initiate their own amplification process near the tails of the electron avalanche where the electric field is highest. The streamer moves away from the electrode and quenches when approaching r_{crit}.

For even higher gain, the streamers may become unquenched, developing into discharges between anode and cathode. Then the limit of stable detector operation is reached, since discharges may be fatal, especially to fragile micropattern structures. To limit the occurrence of streamers, quenching gases like DME, isobuthane or CO_2 are added to the counting gas. The quenching gases absorb UV photons and thus reduce the appearance of streamers.

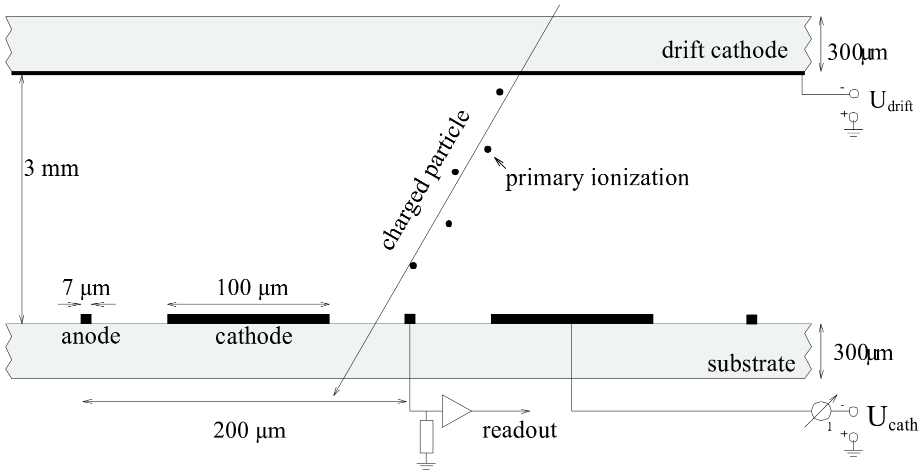

Figure 3.5: Schematic cross section of an MSGC.

3.2 The MSGC

3.2.1 Detector principle and layout

An MSGC is a type of proportional counter, that essentially consists of three parts:

- drift cathode
- drift volume
- micro patterned glass substrate

A cross section of a CMS–type MSGC can be seen in figure 3.5.

In the drift volume, a traversing particle initiates primary ionisation. The produced electrons drift towards the substrate.

The MSGC substrate is covered with a pattern of alternating anode and cathode strips. The cathode strips are brought to high voltage while the anodes are grounded through the readout electronics. The resulting field can be seen in figure 3.6. Close to the anodes, the field is sufficient to start an avalanche amplification of the primary charges.

In a CMS type MSGC with a 3 mm thick drift space, the typical voltage on the drift cathode is -3000 V. A typical cathode voltage is around -530 V.

In calculating the drift field E_d of an MSGC, the substrate geometry has to be taken into account [13]:

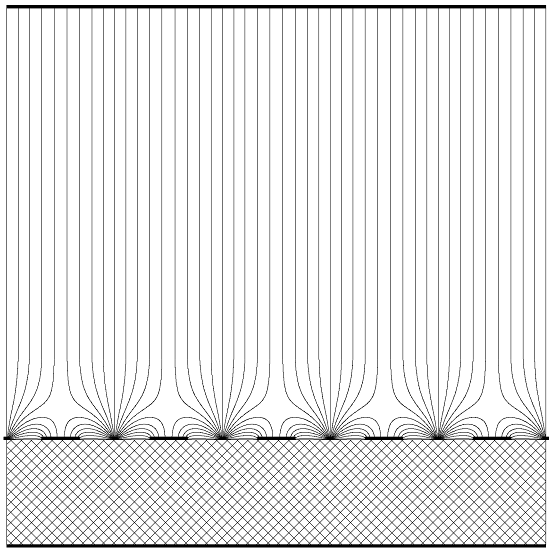

Figure 3.6: The field configuration within an MSGC. [27]

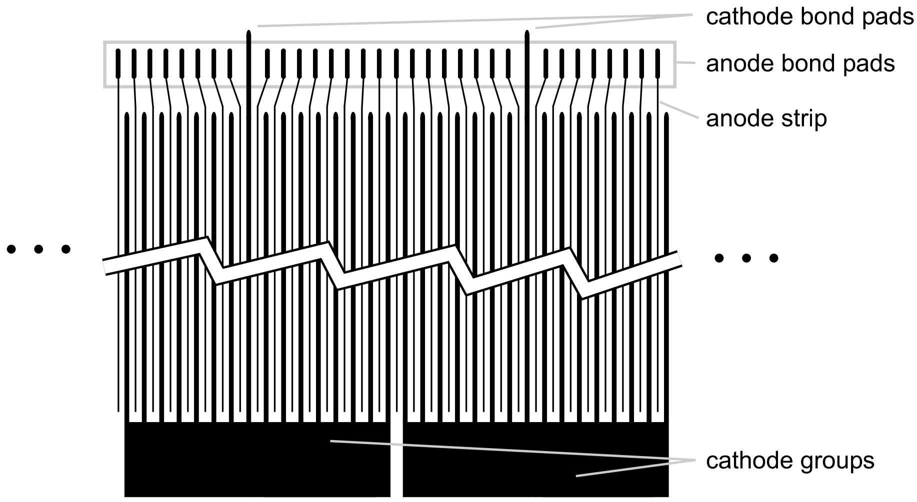

Figure 3.7: Schematic layout of a CMS–MSGC substrate

$$E_d = \frac{U_{drift} - \alpha U_{cath}}{d}; \quad \alpha = \frac{w_k - w_b/2}{d}$$

with:

U_{drift} = drift cathode voltage
U_{cath} = cathode strip voltage
w_k = width of a cathode strip
w_b = space between two cathode strips
d = thickness of the drift space

A scheme of the substrate layout can be seen in figure 3.7. The cathode strips are grouped to reduce the effort in HV[2] contacting. In the case of the CMS MSGCs, 16 cathodes form one high voltage group. The connection between the strips is made on one edge of the strip pattern.

The contacting for both anode and cathode strips is realised through wire bonding. It is planned to bond anodes and cathodes on the same side of the substrate. There the anode strips are longer than the cathodes. Beyond the cathode edges, the anodes widen into bond–pads. For each HV group, one cathode strip reaches beyond the anode bond–pads. This strip is used to contact the entire group.

Alternatively, the cathodes may be contacted on the opposite side through the pads that are formed by connecting 16 strips to HV groups.

3.2.2 Detector characteristics

In the following section, an overview over the most important MSGC properties will be given.

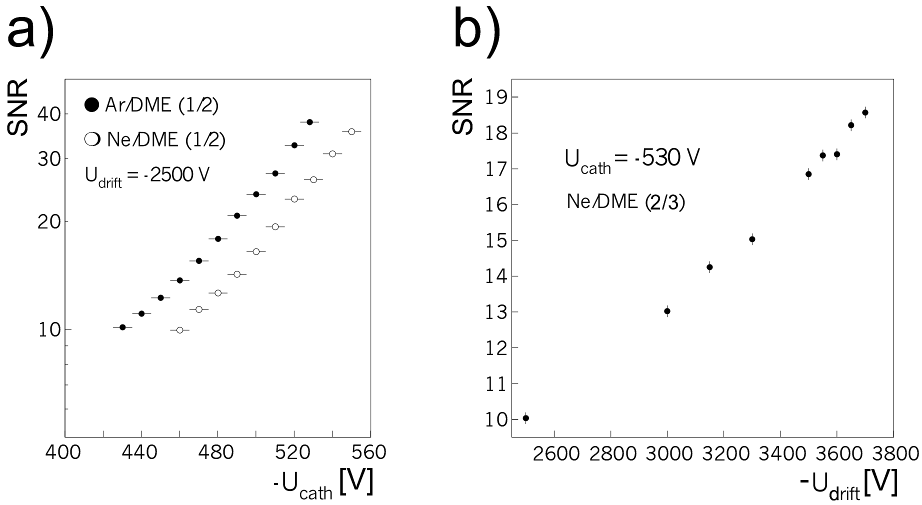

Figure 3.8: Dependence of the MSGC SNR on cathode voltage (a) and drift field (b). [27]

[2]**H**igh **V**oltage

Detector signal

For an MSGC the signal of the detector and therefore it's SNR[3] depends on the voltage settings on cathode strips and drift cathode. Another important parameter is the gas mixture that is used. Figure 3.8 (a) shows the exponential dependence of the SNR on the cathode voltage for two different gas mixtures. For the drift cathode the increase of SNR with the voltage is almost linear as can be seen in figure 3.8 (b).

Efficiency

A very important parameter for detector operation is the detection efficiency ϵ:

$$\epsilon = \frac{number\ of\ detected\ hits}{number\ of\ traversing\ particles}$$

.

It depends on many parameters some of which will be discussed in the following:

detector SNR: A signal within an MSGC has to reach a certain height above the detector noise before it can be detected by the hit finding software.

cluster finding criteria: Whether a hit is accepted depends on the cuts that are applied to distinghish between random noise fluctuations and a real hit (see appendix F). The tighter the applied cuts, the lower the efficiency. Thus the best efficiency is achieved if the cuts are set as loose as possible. At the same time, fake clusters will be found where the noise rises over the particle detection threshold by coincidence. Thus a compromise has to be found between good detection efficiency and a tolerable rate of fake hits. At the CMS experiment a fake rate of about 0.1–0.2 % could be tolerated [27].

gas mixture: Drift and diffusion are different for different gas mixtures [18, 35]. This may also influence the detection efficiency. For example if diffusion increases, so does the cluster size and a wider cluster is not as reliably detected as a narrow one.

For the CMS experiment, it is crucial to know the efficiency of the MSGC. In the hostile CMS environment, a detector should be operated at the minimum gain where it is still efficient. Thus the stress on the detector is minimised. Since the gas mixture and the tolerable rate of fake hits (and thus the cut parameters) are fixed, the efficiency only depends on the detector SNR. It has been shown, that a standard CMS–MSGC becomes 98 % efficient at an SNR of about 13 [16].

Spatial resolution

The spatial resolution of a counter may depend on two parameters:

- diffusion
- anode pitch p

[3] **S**ignal over **N**oise **R**atio, see also appendix F

For a small anode pitch and a high diffusion, the cloud of primary electrons is spread across many strips thereby dominating the resolution.

For a high anode pitch, this parameter determines the resolution. If a particle is detected by only one strip, the spatial resolution can be easily calculated being the rms[4] of the distribution of the traversing particles. Assuming that the particle hits were randomly distributed between -p/2 and p/2, the spatial resolution is given by:

$$\sigma = \frac{p}{\sqrt{12}}$$

For an MSGC with a pitch of 200 μm this would result in a resolution of $\sigma = 58\ \mu m$.

In case of the CMS MSGCs however, a hit is detected as a cluster spread over several strips. By calculating the hit position using the center of gravity method (see appendix F), the spatial resolution can be improved. Consequently, the resolution in a CMS MSGC depends on both, anode pitch and diffusion.

Resolutions around 40 μm have been obtained in a Ne/DME gas mixture [14].

Time resolution

The primary electrons have to reach the substrate before they can create a detectable signal. Since electrons are produced randomly in the drift gap, the signal is stretched over the drift time of about 50 ns within the detector.

The readout at CMS however will be sampled with the LHC bunch crossing interval of 25 ns. Thus an ambiguity of two bunch crossings has to be accepted within the MSGC tracker. It was planned to combine the information from silicon and MSGC tracker in order to identify the correct bunch crossing for the MSGC track.

Rate capability

The rate capability of an MSGC is limited. With increasing particle flux, the probability for two or more particles to pass the same readout strip simultaneously becomes non–negligible. The occupancy[5] has to be kept at the 1 % level for the CMS tracker where the MSGCs will be irradiated at a rate of 10^3–10^4 Hz/mm^2. The MSGC strip length and pitch have to be chosen accordingly.

3.2.3 Limitations and possible solutions

Even though the rate capability of an MSGC is good due to it's high granularity, there are limitations for the simple glass + metal substrates described. The two main limitations are:

- reduced gain due to charging of the substrate
- damage to the anode and cathode strips caused by discharges between them.

[4] standard deviation
[5] number of hits on one strip per trigger

These problems will be discussed in the following:

Charging of the substrate: The cause of the charging problem becomes apparent when looking at the field configuration close to the substrate. For a plain glass substrate, some field lines coming from the anode strip terminate on the glass surface (see figure 3.9 (a)). Ions that drift along these field lines will cause a charging up of the glass, thus reducing the gain of the MSGC.

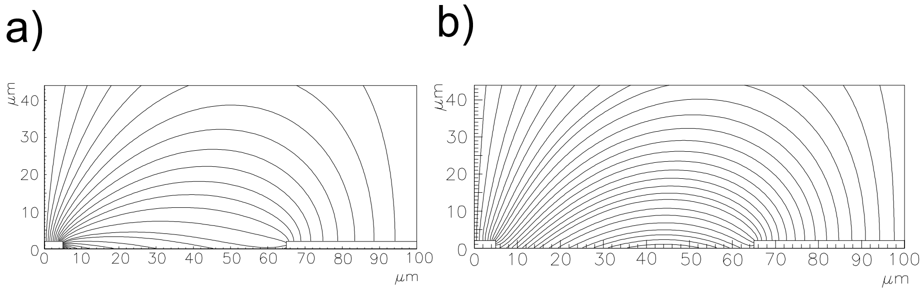

Figure 3.9: Electric field between anode and cathode for an uncoated (a) and coated (b) substrate. [27]

The charging may be overcome by coating the glass with a layer that has a surface resistivity of $10^{14} - 10^{15}$ Ω. The coating modifies the electric field in a way that field lines from the cathodes will terminate on the anodes (see figure 3.9 (b)). A comparison between the high rate performance of coated and uncoated MSGCs can be seen in figure 3.10.

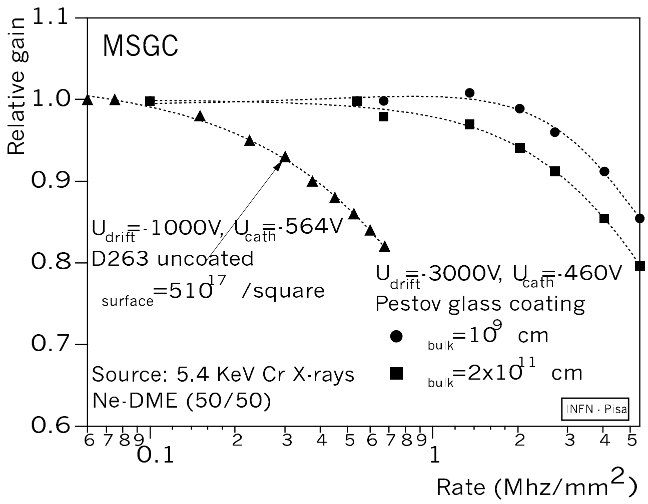

Figure 3.10: The rate capability of an MSGC with an uncoated substrate compared to two types of coated substrate. [27]

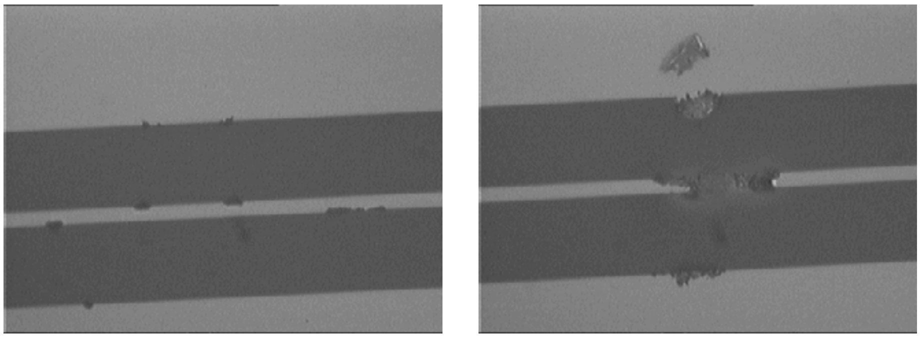

Figure 3.11: Photo of a damaged anode strip that is still fully functional (left) and one that was interrupted by discharges (right). [32]

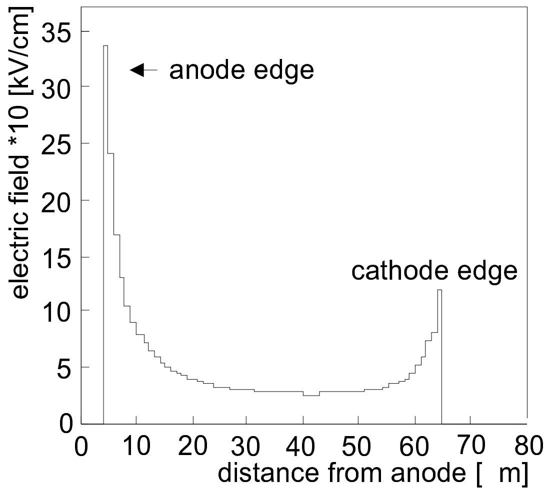

Figure 3.12: Electric field strength between anode and cathode strip. [27]

Discharges between anode and cathode strips: Even for coated MSGCs, new limitations arise, when studying the rate capability in high intensity hadron beams. It was found by the HERA-B collaboration, that the risk of discharges between anode and cathode strips is substantially increased by the presence of HIPs[6] [33]. The gold strips on the substrate may be damaged or even interrupted by the discharges as can be seen in figure 3.11. Several approaches have been made in order to overcome this limitation.

One solution to the discharge problem was proposed by R. Bellazzini. The risk of discharges is highest at the peak regions of the electric field. As can be seen in figure 3.12, the electric field between cathode and anode strip peaks at the strip edges. Thus R. Bellazzini invented the so–called 'advanced passivation' where the cathode edges are protected by a thin

[6]**H**eavily **I**onising **P**articles

polyimide layer that reduces the electric field. This solution was adopted for the MSGC barrel tracker. Good results were obtained with passivated MSGCs in a high intensity hadron beam [16]. A cross section of a passivated substrate can be seen in figure 3.13.

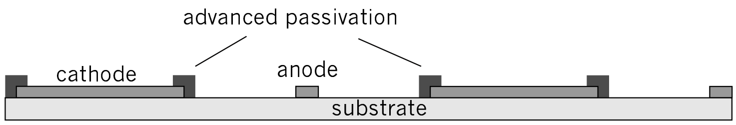

Figure 3.13: Cross section of an advanced passivated MSGC substrate.

In the forward part of the outer tracker, a different solution was envisaged that will be described in the following section.

3.3 The MSGC+GEM detector

3.3.1 Detector principle

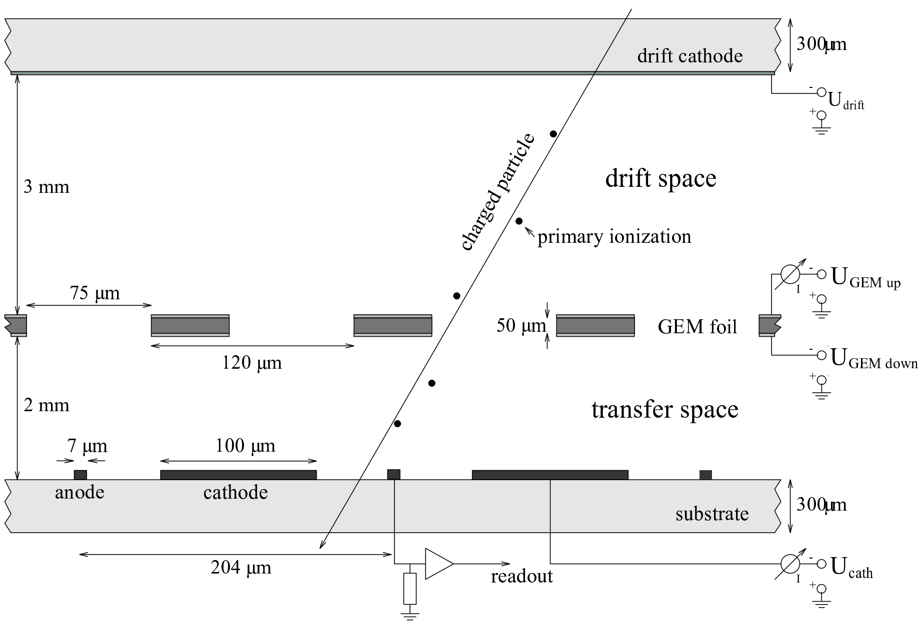

Figure 3.14: Schematic cross section of an MSGC+GEM

It is possible to reduce the discharge probability within an MSGC substrate by dividing the amplification into two stages. Therefore the MSGC+GEM technology has been invented [20]. As second amplification stage, a GEM foil is introduced into the drift space thereby dividing it into two parts: the transfer space below the GEM and the drift space above. A schematic view of an MSGC+GEM detector can be seen in figure 3.14.

The GEM itself is a 50 μm thick copper clad polyimide foil with a pattern of circular holes etched into. Normally, the holes are arrayed in hexagons as can be seen in figure 3.15. The two characteristic properties of a GEM are the hole diameter d and the pitch p. Using these, the optical transparency τ ($\tau = \frac{hole\ area}{total\ area}$)of the foil can be calculated:

$$\tau = \frac{\pi\ d^2}{2\ \sqrt{3}\ p^2}$$

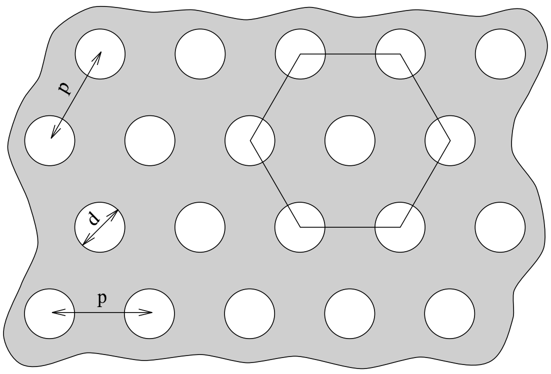

Figure 3.15: Top view onto a GEM foil where the hexagonal hole geometry can be seen.

Within the GEM holes, the electric field is sufficiently large to initiate an avalanche amplification of the primary electrons produced in the drift region. Consequently, the amplification on the substrate can be reduced, allowing the cathode voltages to be lowered by about 100 V.

Of course, a GEM foil can not only be used in the MSGC+GEM detector. A vast field of applications exists, where one or more foils are used for amplification.

The GEM technology was not only considered by the CMS tracker collaboration but such detectors are implemented into the HERA–B [33] inner tracker in an MSGC+GEM system. Single or multiple GEM detectors are envisaged for various experiments like COMPASS [9] and LHC b [10].

3.3.2 GEM foils and producers

Within this thesis, GEMs from two different producers will be discussed. The most common foil manufacturer is a CERN workshop[7]. Recently, Würth Elektronik[8] has been established as an alternative producer [35].

The two manufacturers produce their foils using almost identical etching techniques. However, a small difference between the two production processes has been found to result in foils with some quite different properties (see chapter 5.7.1 and chapter 6).

[7]CERN Surface Treatment Service, Geneva, Switzerland
[8]Würth Elektronik GmbH, Roth am See, Germany

The difference in the two foil types lies in the etching of the holes into the polyimide. While the CERN workshop uses wet etching in the whole manufacturing procedure, Würth electronics plasma etches the foil to obtain the GEM holes.

This results in different hole shapes. For the wet etched foils, the holes are double conical while the plasma etched holes turn out to be underetched resulting in a more cylindrical shape. A more detailed description of the processes can be found in appendix B. A cross section of the holes and the resulting electric field configuration can be seen in figure 3.16

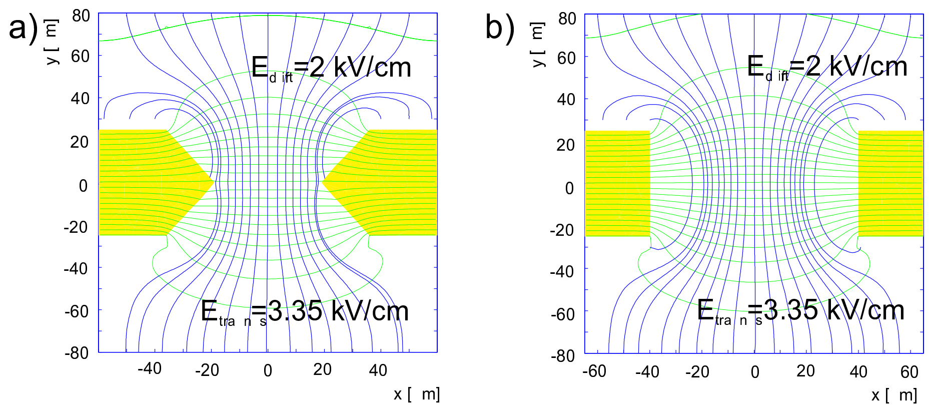

Figure 3.16: Cross section and field configuration of the CERN (a) and Würth (b) GEM [23]).

A second but minor difference lies in the material used for the foils. At CERN, a copper clad kapton foil is used whereas Würth prefers a polyimide called espanex that is also copper clad on both sides.

3.3.3 Detector characteristics

Since an MSGC+GEM is more complex than a plain MSGC, additional characteristic properties have to be studied to understand the detector among them the amplification within the GEM foil.

The GEM foil is in the drift path of primary charges produced in the drift space, so that electrons may be collected on the GEM surface. Consequently they will be lost for further amplification. This directly leads to the GEM transparency which will be discussed in a separate section.

Detector signal

Within an MSGC+GEM, the following parameters may influence the detector signal:

- cathode voltage
- transfer field
- GEM potential difference ΔU_{GEM}

- GEM hole geometry
- drift field

Despite the more complicated structure of the detector, the dependence of the SNR on cathode voltage, transfer field and GEM potential difference (ΔU_{GEM}) can easily be determined.

The detector gain increases exponentially with the cathode strip voltage and ΔU_{GEM} (see also section 5.7.1). The dependence of the gain on the transfer field, however, is linear and will be discussed in section 6.

The gas gain within GEM holes of different geometry has been studied in [19]. There it is shown, that the GEM amplification increases with decreasing hole diameter [19] as can be seen in figure 3.17. This is due to the higher electric field within smaller holes.

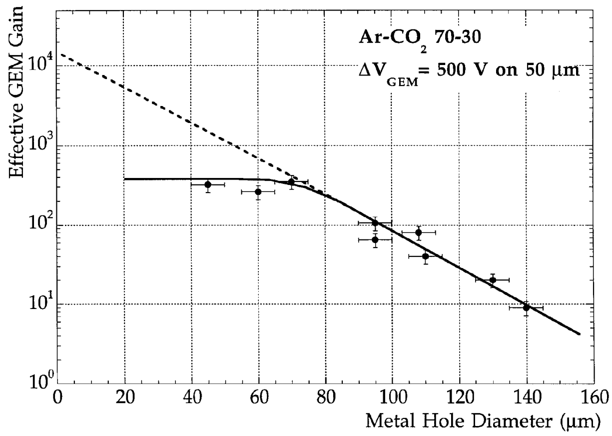

Figure 3.17: Effect of the GEM hole diameter on the gain of the detector. [19]

However, the effective gain in figure 3.17 reaches a plateau below a critical radius of about 70 μm. There the increasing gain is compensated by a loss of avalanche electrons which are collected by the lower GEM side.

The drift field mainly influences the detector transparency and thus will be discussed in the following section.

GEM transparency

The transparency of a GEM foil is defined as the fraction of primary electrons produced in the drift region that enters the GEM holes to initiate an avalanche. It has been studied in detail in [19]. Some of the results obtained there will be summarised here. For the measurements performed in this thesis, mainly two parameters are of importance:

- optical transparency
- drift field

It is straight forward, that the transparency of the GEM depends on it's optical transparency. As the fraction of hole area on the foil surface increases, obviously, more primary charges are collected by the holes.

The dependence of the transparency on the drift field is less obvious. Still it can be understood by looking at the field configuration for two different drift fields as depicted in figure 3.18: In this case a CERN GEM with a pitch of 120 μm and a hole diameter of 72 μm and 35 μm was chosen and the field lines around the GEM holes were simulated. For a drift field of 2 kV/cm, all field lines coming from the drift space traverse the GEM. Thus all primary electrons will enter the holes. With increasing E_{Drift}, field lines start terminating on the upper GEM side so that electrons will be deposited there thus being lost for further amplification.

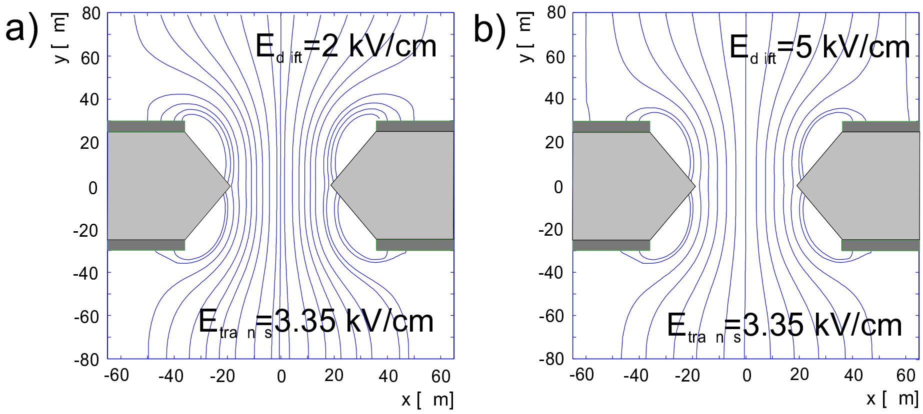

Figure 3.18: Electric field simulations for two different drift fields in CERN GEMs, being 2 kV/cm (a) and 5 kV/cm (b) respectively [23].

The change in detector transparency with altering drift field can directly be seen in the detector pulse height. Two such measurements of pulse height vs. drift field are shown in figure 3.19. In the curve for the MSGC+GEM, the pulse height and thus the transparency is constant over a wide drift field range and starts decreasing between 4 kV/cm and 5 kV/cm. The region of constant transparency is called transparency plateau. The MWPC[9] module displayed in the figure shows a very short (if any) transparency plateau. This can be accounted to two parameters: the lower optical transparency and the lower GEM potential difference of the foil since both parameters influence the plateau length.

As mentioned in the previous subsection, bad transparency is not the only source of signal loss in an MSGC+GEM. It is also possible that electrons are transported to the lower GEM side when they leave the GEM hole. Those are lost for the detector signal as well.

[9]**M**ulti **W**ire **P**roportional **C**hamber

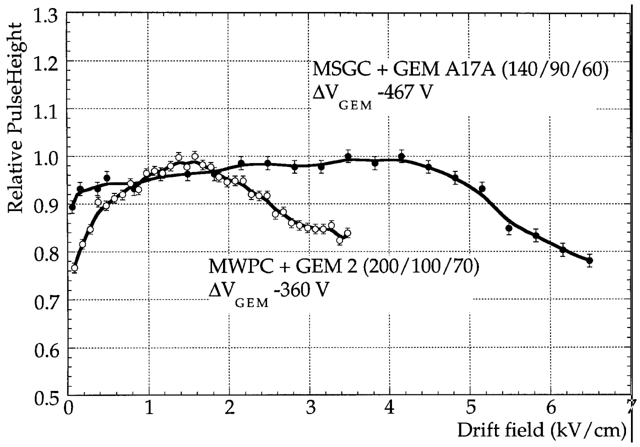

Figure 3.19: Dependence of the detector signal on the drift field for two CERN GEM foils of different optical transparencies in Ar/CO_2 70:30. The hole parameters for the two double conical foils are given in brackets (pitch/outer diameter/inner diameter) [19]

Efficiency

It has been found under similar conditions as in [16], that an SNR of about 18 is needed to reach 98 % efficiency for an MSGC+GEM [17].

Spatial resolution

For an MSGC+GEM with a 200 μm pitch a resolution of about 40 μm was measured in a Ne/DME gas mixture [35]. This is comparable to the resolution of a plain MSGC.

Time resolution and occupancy

The signal shape within an MSGC+GEM detector is determined in the drift space (see chapter 6). The drift space is of the same thickness as for a plain MSGC but the drift field is much lower. Thus the total drift time is increased and the ambiguity in the bunch crossing identification will be increased.

The same is true for the occupancy which should also be slightly increased.

Chapter 4

Large scale assembly of MSGC+GEM detectors

In total 18 detector modules of the same geometry have been assembled and tested within a period of two months[1]. Five of them were built and tested in Aachen. The remaining 13 were assembled in Karlsruhe (Institut für Experimentelle Kernphysik, Universität Karlsruhe) and tested in Karlsruhe, Strasbourg (Institut de Recherches Subatomiques) and Bruxelles (Universite Libre de Bruxelles). At the time of their assembly, the modules were built as a pre-series for the CMS outer forward tracker, to demonstrate mass-production capability. Right after assembly their radiation–hardness was investigated in the so-called "mf2 milestone" that will be described in chapter 5.

4.1 Layout and components

As described in chapter 2.3, the forward tracker was meant to consist of four rings of MSGC+GEMs per disk. For the 18 modules described, the geometry of ring 2 was chosen. The detector layout can be found in appendix A. As can be seen in fig. 4.1, each module consists of the following components:

- One gold-clad, 300 μm thick ferrozell[2] drift cathode.
- One GEM-foil of 50 μm thick copper-clad Kapton with a hexagonal hole layout. For the 18 detector modules built, 17 foils were produced at CERN and one by Würth. For the CERN foils, the outer hole diameter is 72 μm and the inner diameter is 35 μm at a pitch of 120 μm. They are also divided into four segments, each the size of one substrate. For the unsegmented Würth Elektronik foils, the holes are 80 μm in diameter and 130 μm in pitch.
- Four wedge shaped substrates with 512 gold strips on uncoated DESAG263[3] glass. The pitch is 204 μm at maximum and 181 μm at minimum while the strips are 9.75 cm long. The substrates were produced by IMT[4] (60

[1]mid August 1999 to mid October 1999
[2]Ferrozell GmbH, Augsburg, Germany
[3]**DE**utsche **S**pezialglas **AG**, Delligsen, Germany
[4]IMT Masken und Teilungen AG, Greifensee, Switzerland

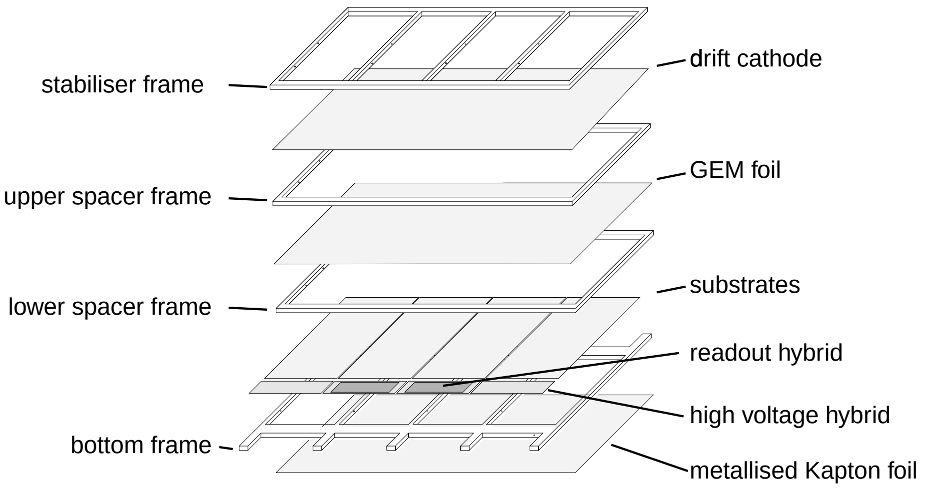

Figure 4.1: Blow up of one detector module

substrates), Optimask[5] (8) and IMEC[6] (4)

- Two readout hybrids equipped with PreMux128 [11] electronics (see appendix D). Since the available test beam facilities provided particle beams of approximately 10 cm in diameter, no more than two substrates could be simultaneously illuminated. Thus, to reduce the costs, only the two inner substrates were equipped with readout electronics.
- Four HV hybrids to power the four substrates.
- One copper-clad Kapton foil that was used to close the detector module below the bottom frame.
- Four frames:
  - A bottom frame onto which the substrates were glued. Two precision holes in that frame allowed an absolute positioning during module assembly.
  - A 2 mm thick lower spacer frame between substrates and GEM foil.
  - A 3 mm thick upper spacer frame between GEM foil and drift cathode.
  - A stabiliser on top of the drift cathode to prevent it from sagging.

The choice of the materials described was mainly dictated by two requirements: Firstly, the detectors had to be radiation-hard. Secondly they had to withstand flushing with DME which is a solvent. During the past 10 years of research, extensive studies regarding both aspects have been carried out [24]. Thus the 18 modules were mainly built of the materials that would have been used for the assembly of the CMS detector with only the two following exceptions:

[5]Optimask, Morangis, France

[6]**I**nteruniversitaire **M**icro **E**lektronika **C**entrum, Leuven, Belgium

- The readout electronics used in this milestone is not suitable for the CMS tracker, since the PreMux128 chip is not radiation–hard. However, the final chip, APVM [40], was not available at the time of assembly. After mf2, two substrates in two different modules have been equipped with APVM readout for further testing (see chapter 6 and [38]).

- Although the modules in Aachen and Karlsruhe were identical in layout and purpose, different materials have been used for the frames. While Karlsruhe chose to use machined Ferrozell frames, in Aachen molded PEEK[7] frames were preferred. The choice in Aachen was made with respect to the envisaged mass production of detector modules. Ferrozell and PEEK are very expensive and machining all frames for a CMS tracker would have meant wasting more than 90 % of the material. Thus for a large scale assembly of MSGC+GEMs it is cheaper to use molded frames. In the pre-series of 5 modules, it could be tested whether it is possible to mold frames of the required precision.

A cross section of a finished detector module can be seen in fig. 4.2.

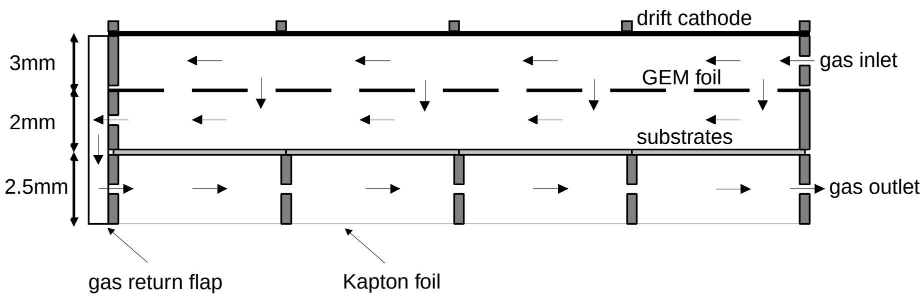

Figure 4.2: Cross section of one detector module

4.2 Assembly

Before starting the assembly , the quality of the GEM foils and substrates were tested. Therefore the GEM was brought to a potential difference of -500 V in a dry N_2 atmosphere. Foils that were not capable of stable operation under these conditions were rejected.

For the substrates, the capacitance of the readout strips was measured with a probe station in order to identify broken anode strips or short circuits.

After these initial tests, the detector components were glued together using EPO93L[8]. Since this glue requires one day to dry, it limits the assembly speed. The production of the five modules in Aachen has thus been optimised to reduce the required assembly time for each module to six or seven days:

Day one: The substrates are cut along the edge of the outer cathode strip. They are then rinsed with isopropanol and deionised water and cleaned

[7] polyetheretherketon, Bohlender, Lauda
[8] AXSON GmbH, Dietzenbach, Germany

in an ultrasonic bath for 10 minutes. After the cleaning procedure, the substrates are inspected optically using a microscope to find flaws in the micro–strip pattern.

For the substrate positioning, a fibre optic alignment system is used that allows a precision of 5 μm. Two neighboring substrates are aligned in a way that the cathode strips on the edges are exactly one pitch apart [21, 38]. The substrates are then glued to the bottom frame through four connection points.

On the same day, the stabiliser frame is glued onto the drift cathode. In parallel, the GEM foil is fixed between the two spacer frames. For the latter task, a precision jig has been developed that consists of two aluminum plates. The negatives of the two spacers have been machined into those plates in order to fix the frame position with the required precision. Using pins for alignment, the GEM is now glued to the lower frame and stretched flat using tape. Then the top spacer is glued onto the GEM foil.

Day two: With glue, the substrates are sealed gas tight from the back. In addition, the drift cathode is fixed on top of the GEM+spacers element. Therefore, the lower spacer remains fixed in the aluminum frame. To position the drift cathode, a similar tool as for the glueing of the GEM on the previous day is used. A photo of the jig used in this assembly step can be seen in fig. 4.3

Day three: In order to cut the GEM to the size of the frames, the upper part of the detector is taken out of the jig. The module is then closed by glueing the upper part onto the substrates. To ensure correct positioning, the holes in the bottom frame are used for alignment.

Day four: The Kapton foil is glued to the lower side of the bottom frame.

Day five: The Kapton foil is cut to the size of the module, leaving only one flap at the side, where the gas is to be flushing from the detection volume to below the substrates. That flap is then glued to the side of the detector in order to close the gas volume (see fig. 4.2). In parallel, the gas inlet and outlet are equipped with two tubes that ensure the gas connection.

Day six: The finished module is connected to a gas system to test whether it is gas tight. If leaks are found, they are sealed with EPO93L and the glue is left to dry over night so that the detector is finished on the seventh day.

If no leaks are found, the HV hybrids and readout electronics are glued to the substrates. The module is now ready to be bonded and mounted after six days of assembly. A photo of a mounted mf2-module can be seen in fig. 4.4

In a mass production, it is possible to assemble several modules in parallel. In such a scenario, two bottle necks have to be considered.

Firstly, the substrate positioning system is rather expensive. Thus only one such tool can be afforded in Aachen. This means that only one detector module can be started each day, since the glued frame and substrates have to stay on

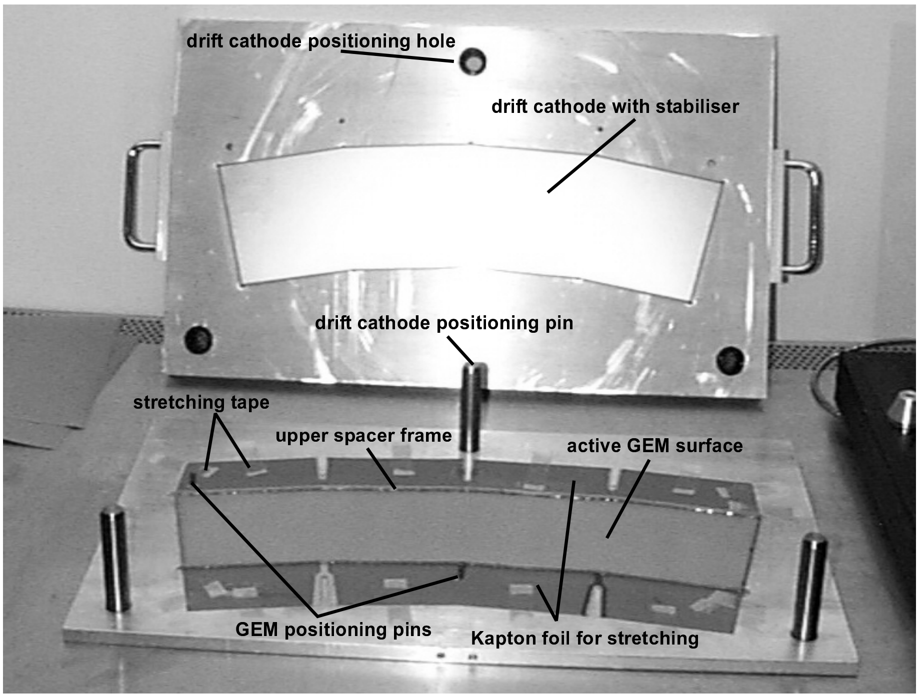

Figure 4.3: Photo of the jig that is used to glue the drift cathode on top of the upper spacer frame. The GEM (in this case produced by Würth Elektronik) between two spacers can be seen on the aluminum plate that is lying on the table. The drift cathode with it's stabiliser is put into the upright plate. Three positioning pins in one aluminum jig and the corresponding holes in the other one are used to guide the upper plate into the correct position.

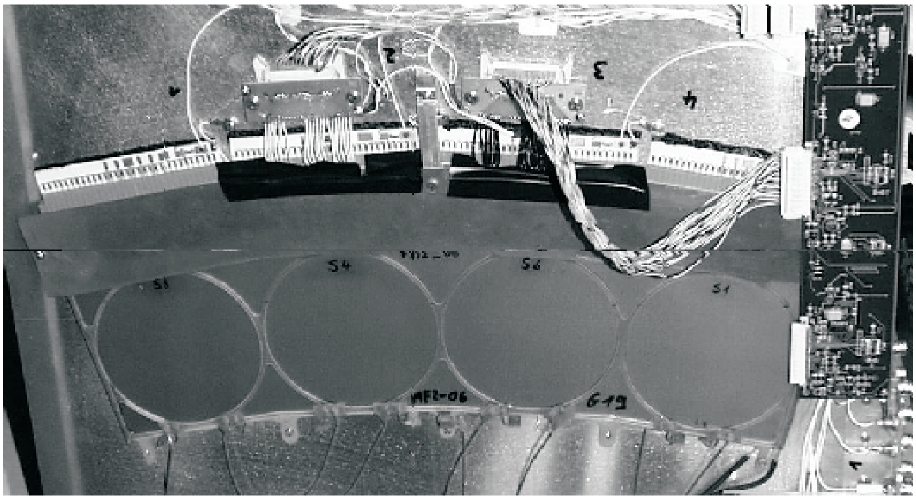

Figure 4.4: Photo of a mounted mf2 detector module already connected to the readout electronics.

the jig to dry over night. As a consequence the amount of modules that can be glued in parallel is limited to five[9].

Secondly, MSGC+GEMs are very fragile devices and have to be assembled in a clean room facility, where space is limited. In Aachen, a clean room to provide space for five glueing jigs would have been available in flow boxes where the glueing could take place.

The assembly procedure used in Karlsruhe was not entirely identical to the one described here. A description can be found in [17].

4.3 Module burn–in and functionality test

Before the mf2 test beam, it had to be ensured that all modules were working properly. Therefore firstly, high voltage capability of substrates and GEMs had to be checked separately in the so-called "burn-in" process (see section 4.3.1). Secondly, the modules were fully powered in order to determine whether they could be operated as efficient particle detectors (see section 4.3.2).

In addition, all dead channels due to damaged readout electronics or broken anode strips had to be identified. A description of how this is done can be found in appendix C. In the following two sections only the testing of the five Aachen-built modules is described. The Karlsruhe modules will be referred to briefly in section 4.3.3. The burn-in and functionality test in Aachen has been done, using a Sr^{90} source and the same facility as for the measurements described in chapter 6.1.1. A more detailed description of the laboratory test setup will be given therein. The analysis software that is used here is described in appendix F.

4.3.1 Burn–in

For the burn–in of the GEMs each foil was slowly ramped up to a potential difference of -400 V and left there for one night in order to prove it's remaining high voltage capability. Since the foils had already been tested, their burn–in was uncritical.

The substrates were slowly ramped to $U_{cath} = -400\ V$ and left there over night. On the next day, they were ramped up to $U_{cath} = -500\ V$.

The substrate burn–in is a more delicate process than for the GEMs. Due to bad etching of the gold pattern some of the anode strips may be weak enough to be damaged or interrupted during the burn-in. In addition, shortcuts may develop between weak strips during the first hours of operation at high voltage. Those shortcuts have to be removed by cutting the bond between anode and readout electronics before applying high voltage. Thus one strip is lost for further operation.

This is what makes the burn-in important in detector mass production: The CMS outer tracker is a system containing several thousand detectors. Therefore, weak spots have to be found before closing the tracker. Afterwards it is very difficult to reach the detectors for maintenance.

After the assembly and burn-in of the five Aachen modules, 88 strips out of

[9]Only the assembly steps on days one to five are considered here. The leak testing of the modules is independent of the rest of the assembly procedure.

5120 have been lost[10]. This amounts to 1.7 % of damaged readout channels. Finally all substrates were capable of withstanding voltages of at least -500 V on the cathodes.

4.3.2 Functionality test

To ensure the good performance of a module, the following tests were made:

- Ramping up of all voltages until an SNR of the order of 30 is achieved.
- Measurement of the peaking time of a detector in a delay scan.
- Measurement of the signal uniformity across the active surface.
- Comparison of the gain of a detector with the other modules by determining the cluster charge at a given voltage setting.

After powering the five Aachen modules, it could easily be seen, that three detectors equipped with CERN GEMs were performing well and showed a comparable signal. For the remaining two modules, a different performance was observed. Further investigations were made to understand the variations.

The fourth CERN–GEM module had a significantly lower signal than the other three. In addition, the peaking time of the signal was shifted towards higher delay values. A possible reason for this could be found in an accident that had happened during detector assembly: The GEM foil had been ripped off the frames and re-glued. Thus the foil was no longer properly stretched and might be sagging.

A sagging GEM foil would lead to a changed drift– and transfer gap and thus to a modified field configuration within the detector. This can certainly affect the signal of a module. The reduced signal indicates a sag towards the drift cathode.

Since the sagging of the GEM changes the drift– and transfer field, the drift velocity of the electrons is affected and the peaking time should be shifted (see also chapter 6). This shift depends on the position across the substrate, because the GEM sag is lower at the edges of the detector. Indeed it was found that the peaking time was shifted and that near the frames it was closer to that of the intact detectors.

During the test of the Würth–GEM module, a flaw in the design of the Würth-GEM became apparent. The Kapton on the left and right edge of the foil ends a few millimetres beyond the spacer frame[11] (see figure 4.3). Since a wider kapton edge is required to apply tape, the foil could not be stretched in that direction which resulted in a fault across one substrate. This fault could be identified in the same way as for the sagging CERN GEM. By carefully monitoring the peaking time across both substrates, it could be shown, that only one substrate is affected by the GEM-sag, while the other is performing normally. In any case, this particular sag can be avoided by modifying the layout of future Würth GEMs.

[10] Only the two inner substrates of each module are considered since the outer ones are not read out.

[11] For the CERN–GEMs the Kapton exceeds the spacer frame by several cm in all directions.

4.3.3 Burn in and functionality test for the Karlsruhe modules

For the 13 modules assembled in Karlsruhe, the same tests as in Aachen have been done. 12 modules were found to be operational while the module equipped with IMEC substrates could not be operated properly. The IMEC substrates already failed during the burn in.

Six detector modules out of the 12 showed signs of GEM sagging though no reason could be identified. After the test beam, one of the Karlsruhe modules was opened and indeed a GEM sag of about 1 mm was measured.

4.4 Conclusions

In Aachen, five modules have been successfully built and tested. They were all found to be operational with only slight restrictions in two cases. The cause for the problems has been identified in assembly errors that can be avoided in the future. Thus it has been shown that mass production of MSGC+GEMs at a rate of one module per day is possible in Aachen.

Chapter 5

High rate beam test and the mf2 milestone

To prove that MSGC+GEMs were fit for the CMS experiment, they had to be tested in a high intensity hadron beam. Therefore, the mf2 milestone[1] was defined (see section 5.1) where the 18 modules from Aachen and Karlsruhe were irradiated at PSI[2]. After a discussion of the test setup and test beam conditions in sections 5.2 – 5.4, the milestone results will be given in sections 5.5 and 5.7.2

In addition, the capability of safe operation beyond the working point (safety margin) was investigated in the test beam for some modules (see section 5.6) and a comparison of the two different GEM foil types was made (see section 5.7.1).

5.1 Definition of the mf2 milestone

For the mf2 milestone, the following demands had to be met:

- Production of 12 fully functional MSGC+GEM forward prototypes.
- Irradiation of 24 substrates in a hadron beam at an intensity of $\approx 6\ kHz/mm^2$ for 360 hours while operating at a working point that ensures > 98 % detection efficiency at CMS.
- Loss of less than 0.27 % of anode strips. This can be extrapolated to a partial loss of less than 10 % of strips after 10 years of LHC operation.

On the working point, the modules had to be operated at an SNR, where a sufficient detection efficiency could be guaranteed. For PreMux128 electronics it has been shown, that 98 % detection efficiency is reached at an SNR of ≈ 17 [17]. In order to ensure the same efficiency in CMS using APVM electronics in deconvolution mode an operation at 2.2 times that SNR is required (see appendix E). Thus the working point for the mf2 milestone was set to an SNR of ≈ 37.

[1]**M**ilestone **F**orward number 2, following the first forward milestone [12]
[2]**P**aul **S**cherrer **I**nstitut, Villigen, Switzerland

The main danger for an MSGC+GEM detector module in CMS lies in the destruction of anode strips by sparks leading to a degraded detector performance. Thus the loss of readout strips is a sufficient criterion for the safety of detector operation.

It has been shown that the loss of a single readout strip does not lead to a reduced detection efficiency but only to a degraded spatial resolution [27]. Thus loosing less than 10% of the readout strips in 10 years of LHC operation means that the spatial resolution in less than 5 % of the area of the MSGC+GEM tracker will be somewhat degraded.

5.2 Test setup and data acquisition

The milestone test took place in the πM1 test facility at PSI. There the modules were mounted on an optical bench in 9 groups, each consisting of two detectors placed back–to–back.

The modules were named from 1A/1B to 9A/9B according to their bench position and grouping, as can be seen in figure 5.1. The modules 1A and 2A–3B were the ones built and tested in Aachen.

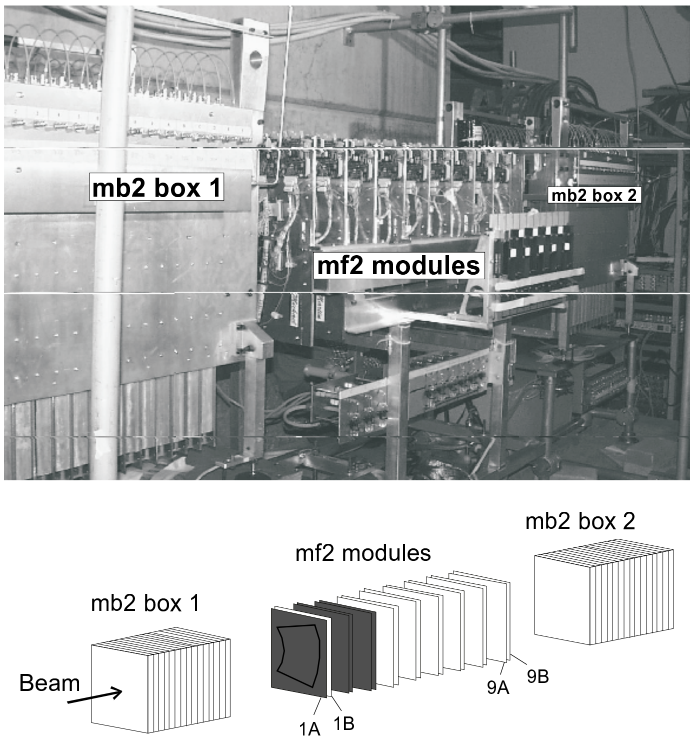

Figure 5.1: Photo and scheme of the milestone test setup. The five Aachen–built MSGC+GEM modules (1A and 2A to 3B) are marked in grey in the scheme.

During the whole beam test, module 1B could never be operated efficiently[3] and will thus not be included in the following analysis.

In front of and behind the mf2 bench, two groups of 16 MSGC counters each were placed. These MSGCs were tested in the so–called "mb2 milestone"[4] which is the equivalent to mf2 for the barrel part of the CMS tracker [16]. A photo and scheme of the three boxes can be seen in figure 5.1. As counting gas, Ne/DME (40 %:60 %) was used.

During the beam test, the signal of each detector had to be monitored as well as the current on it's electrodes. A scheme of the data acquisition system that was used can be seen in figure 5.2. The system was provided by the Lyon CMS forward tracker group[5].

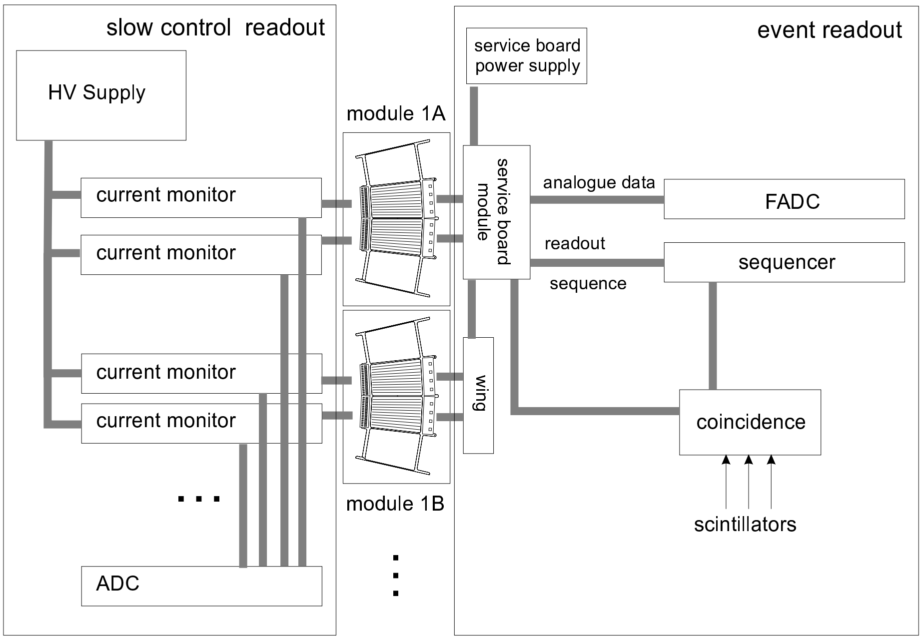

Figure 5.2: Scheme of the data acquisition system used at the milestone test-beam

The MSGC+GEM detector modules were read out by a so–called SBM[6] [31]. That module itself is equipped to read out two PreMux128 [11] hybrids. It can be extended by two wings, each capable to read out three additional PreMux128 hybrids. At mf2, two back–to–back detector modules were read out by a combination of an SBM to read out the front (A) module and one wing reading out the back (B) module.

The trigger was provided by a coincidence of several scintillators placed in front of and behind the setup. A sequencer was used to control the readout of

[3]Module 1B was the one equipped with IMEC substrates. (see chapter 4).

[4]**M**ilestone**B**arrel number 2, where at least 25 barrel–MSGCs with advanced passivated substrates had to be irradiated for at least 360 hours at a detection efficiency of 98 % with a loss of less than 0.27 % of readout strips.

[5]Institut de Physique Nucléaire, Lyon, France

[6]**S**ervice **B**oard **M**odule

the multiplexed PreMux128 channels via FADC.

The currents on the substrates and upper GEM sides also had to be monitored[7] via current monitors in the HV supply line and read out by two ADC cards every 2 ms. 1024 of these current values were combined to a so–called "slow–control event" to be stored on disk. This allowed a detection efficiency for discharges within the modules of around 95 %.

Unfortunately one of the two ADC cards used was defect during the first few days of the milestone. Thus only the substrate currents and the GEM currents of the modules 1A, 2A, 2B, 3B, 4A and 4B could be read out during that period. All GEM stability information given in this chapter for the other modules only considers the rest of the milestone. On the other hand, the currents have been watched manually during the whole test beam. Thus it is safe to assume that no significant changes in the behaviour of the GEM occurred.

In addition, the current monitor for the GEM current of module 5A was broken so that no GEM stability information is available there.

5.3 Beam test conditions

The modules were irradiated in a 350 MeV pion beam with a small proton contamination that was not exactly specified. The maximum beam intensity was $\approx 6\ kHz/mm^2$. The beam profile was almost gaussian with a horizontal width of $\sigma = 35\ mm$ and a vertical width of $\sigma = 45\ mm$ rms. In addition to the pions which are MIPs, the detectors were exposed to HIPs. The latter were produced by interactions of the pions with the detector material. The rate of HIPs was $\approx 10^{-4}$ per pion in each detector.

The six weeks at PSI were divided into 4 phases:

setting up (20.10. – 30.10.99): The detectors were mounted in the test area and brought to a working point of SNR=37.

hardening (30.10. – 4.11.99): The modules were operated at the working point so that weak strips that had survived the burn–in would be destroyed before starting the actual stability test.

mf2 milestone (4.11. – 24.11.99): Operation of the modules at the same working point for 376 hours.

exploration of safety margin (24.11. – 1.12.99): For six of the modules, the SNR was increased in order to determine the maximum SNR, for which safe operation is possible.

During operation at PSI, the SNR of the detectors had to be monitored constantly. To do so, some problems had to be overcome that will be described in the following.

During irradiation at a rate of $\approx 6\ kHz/mm^2$, the SNR, which is determined using the standard IRIS cluster finder (see appendix F) is too high by a factor of two to three. This is due to the fact that the triggering particle is not the only

[7]There were not enough readout channels to monitor all electrodes. However, by monitoring the upper GEM electrode and the substrate currents, it should be possible to detect all occurring discharges.

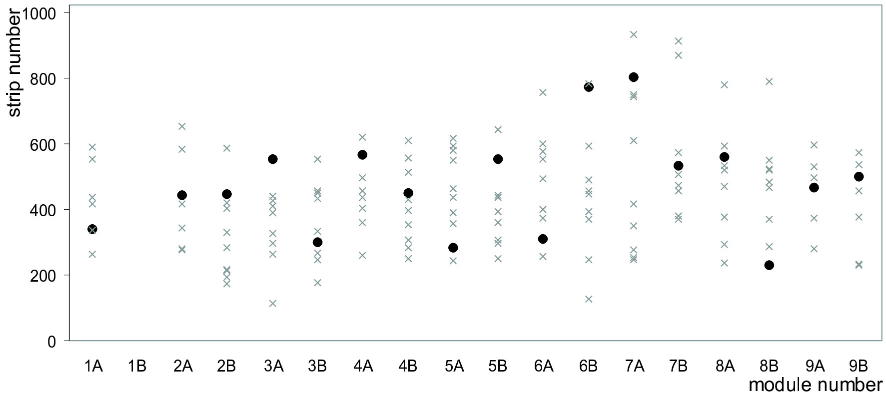

Figure 5.3: One event at full intensity. The position of the largest cluster in each module is marked with a circle while all other hit positions are represented by crosses.

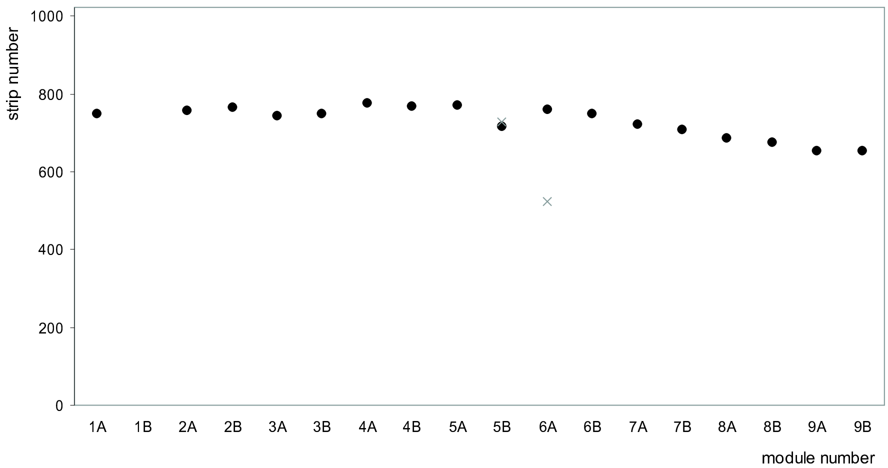

Figure 5.4: One event at low intensity. Only one track can be found here. A few noise hits are marked by crosses.

one found in the detector. At these high rates, the hit multiplicity is around 8–10 particles per event. An example of one event at a rate of $\approx 6\ kHz/mm^2$ can be seen in fig. 5.3. The largest cluster in each module is marked with a circle. Obviously the largest clusters are not always due to the triggering particle. As a consequence, the SNR coming from the largest clusters is systematically too high.

In order to identify all tracks, a complex tracking routine would be required. It would be necessary to find and distinguish approximately 10 tracks. Because of interactions and multiple scattering the routine would also have to include diverted tracks. Even if all tracks could be identified correctly, the track belonging to the triggering particle would still have to be found. Since the tracks are indistinguishable, this is impossible.

Finally, a different approach was chosen. Twice a day, the beam intensity was lowered to $\approx 0.2\ kHz/mm^2$ for about one hour in order to take reference points at "low intensity" where the triggering particle is the only one that leaves a track in the detectors. In fig. 5.4, an event at low intensity can be seen. After that, irradiation at "high intensity" continued.

5.4 Current monitoring and discharge detection

For a detector module that is powered but not irradiated, the current on the electrodes is expected to be $\leq$10 nA. Under high rate irradiation, the modules draw currents that depend on the gain of the counter and on the beam intensity. At an SNR of ≈ 37 and high intensity, the current on the MSGC cathodes lies between 60 nA and 120 nA. The current on the upper GEM amounts to 50–150 nA.

In addition to the currents, short but drastic overcurrents are observed. To detect and classify them, the currents recorded on the upper GEM electrode and on the cathode strips of the two irradiated substrates per module have been analysed (see appendix F). It was found, that for an MSGC+GEM one can distinguish between four sources of overcurrents:

1. **Discharges within the GEM:** In this case, a discharge between the upper and lower GEM electrode occurs. These events may trigger a spark on the cathode strips. A GEM discharge and the response on the substrates can be seen in figure 5.5. The discharge on the GEM cannot be observed directly, since it lasts only nanoseconds. What can be seen on the current monitors is the recharging of the GEM foil, which lasts several hundred milliseconds and drives the current monitor into saturation. On the two substrates, an induced overcurrent can be observed, followed by a drop in the current being due to the reduced gain within the module while the GEM capacity is recharging.

2. **Substrate overcurrents:** Since the substrate is the most fragile part in an MSGC+GEM detector, it is crucial to understand the different kinds of overcurrents that may occur there. To do so, the charge corresponding to substrate overcurrents were histogramed in figure 5.6. A clear separation of two types of overcurrents can be seen:

    - In most cases, the charge is below 5 nC, corresponding to self-quenched

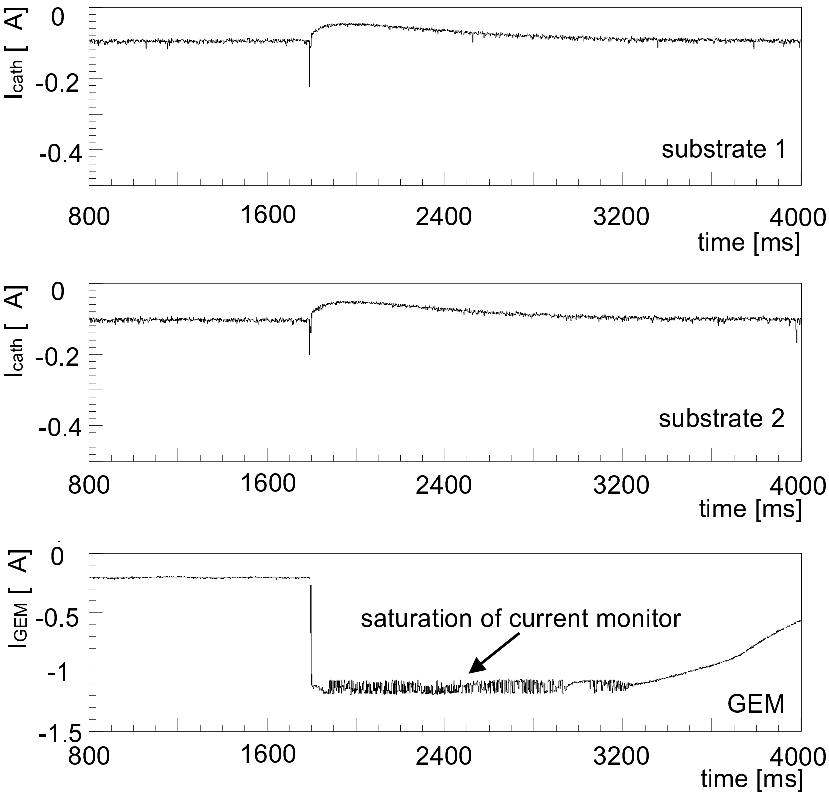

Figure 5.5: Cathode strip and upper GEM electrode current as a function of time when a GEM discharge occurs.

streamers. These streamers are most probably caused by the presence of HIPs that induce avalanches that are sometimes large enough to be detected in the current. A single streamer is thought not to do damage to the substrate. Consequently, the streamers will not be regarded in the following analysis.

- A second peak around 30 nC can be seen. This peak is understood as being caused by unquenched streamers developing into sparks from the anode to the cathode strips [34]. Their charge remains below the maximum charge of ≈ 38 nC that can be stored on a cathode group[8]. A typical spark can be seen in figure 5.7. A closer look at GEM discharges revealed that in some cases they triggered a spark on the substrate. The charge distribution of these events is the same as for sparks that are not correlated to a GEM activity. Thus the two types of sparks will be treated in the same way.

3. **Discharges from a GEM electrode to the substrate:** At higher transfer field, more and more field lines are going directly from the lower GEM

[8]The capacity of one cathode group was measured to be between 78 pF and 80 pF. With U_{cath} between -420 V and -480 V, the charge that is stored on a cathode group is around 38 nC.

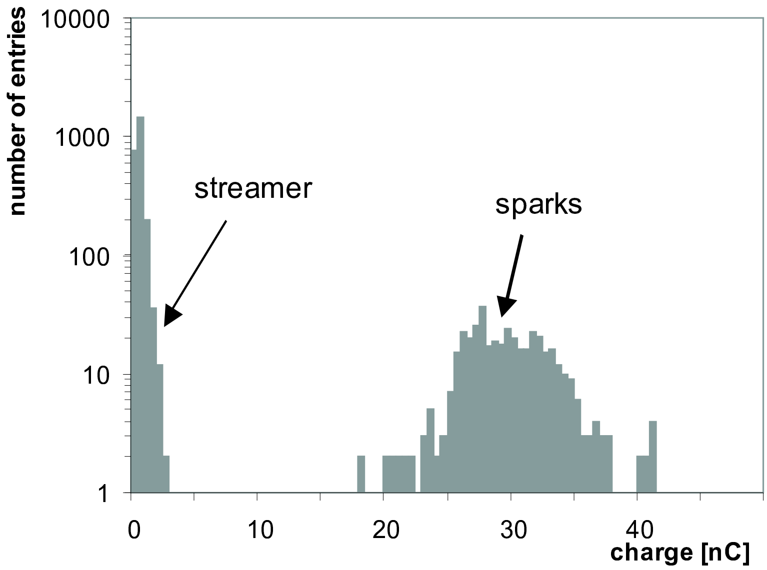

Figure 5.6: Distribution of the charges detected in the cathode strip overcurrent.

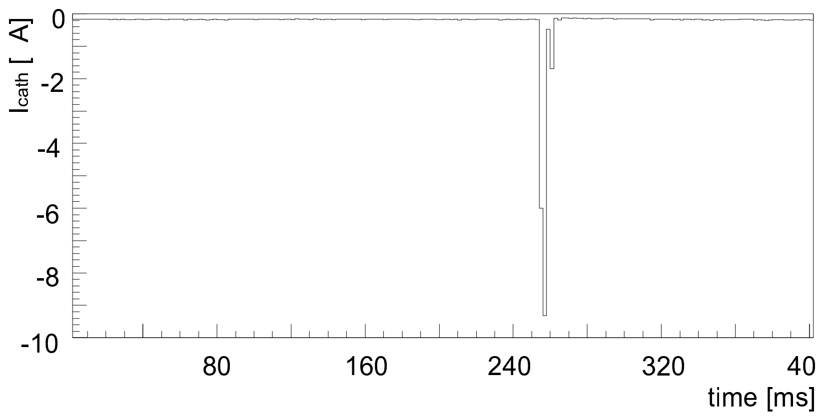

Figure 5.7: Cathode strip current as a function of time showing a substrate spark.

electrode to the substrate. Along these field lines, discharges between the lower GEM electrode and the substrate may occur [33]. However such events have not been observed during the whole data acquisition period. On the other hand, observations from other groups show, that discharges from the lower GEM to the substrate should leave a clear signature in the cathode current and are very likely to cause a shortcut in the affected cathode group [33].

4. **Discharges of the drift cathode:** In some rare cases, the drift cathode can discharge into the upper GEM electrode. No such event has been observed up to a drift field of 5 kV/cm although it should be possible to detect them by looking at the current in the upper GEM electrode.

5.5 Detector stability in the milestone

During the setting up and hardening phase, the detectors had already been set to the working point where they were kept for the whole milestone period.

The fields were comparable for all non–sagging modules. They were operated at drift fields of 4–5 kV/cm and transfer fields of $\approx 3.4\ kV/cm$.

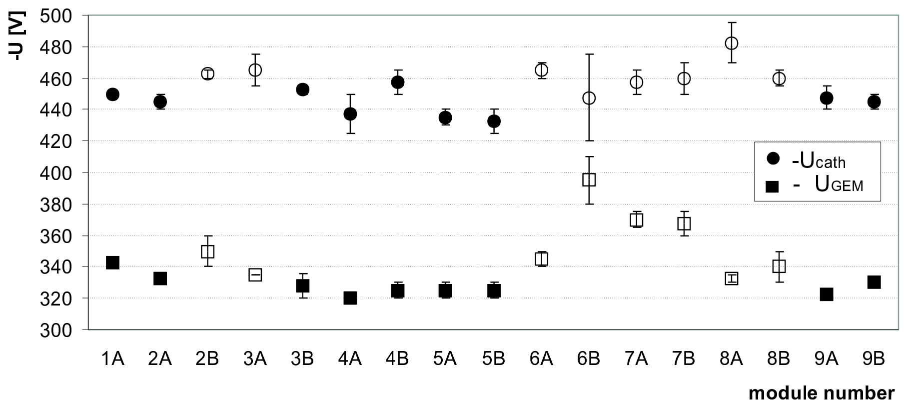

Figure 5.8: The voltage settings for U_{cath} and ΔU_{GEM} during the milestone. The open symbols indicate sagging GEM foils. Since the voltages were changed for some modules, the error bars indicate maximum and minimum voltage in these cases.

For the sagging GEMs it is not possible to give the exact field configuration, since the field varies along the strips. Still, the same potential difference between upper GEM and drift cathode as for the non–sagging modules was chosen. Thus the drift field should have been slightly above 5 kV/cm. Since the GEM foils were most likely sagging towards the drift cathode, a higher $U_{GEM\ down}$ than for the non sagging modules was chosen, setting the transfer field to $\approx 4.4\ kV/cm$ at the edges of the module.

The settings for U_{cath} and ΔU_{GEM} for all modules can be seen in fig. 5.8. The error bars in this figure indicate voltage modifications that were made during the milestone period giving the maximum and minimum applied voltage. Only minor voltage adjustments of no more than $\pm 5V$ to $\pm 15V$ on the U_{cath} or ΔU_{GEM} were made for the non–sagging modules. For the detectors with problems like sagging GEMs, larger modifications have been made.

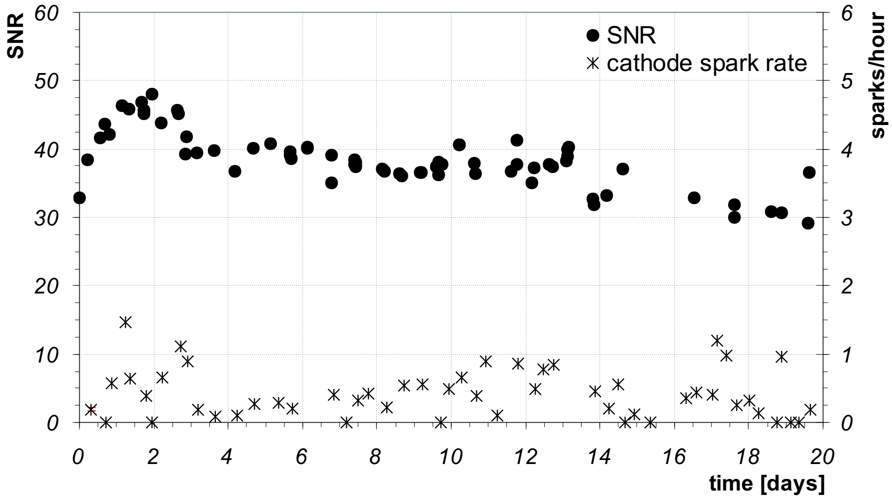

Figure 5.9: The SNR and spark rate of module 9A during the milestone period.

The mf2 milestone lasted for 20 days including all periods of low intensity operation and with no beam available. The performance of module 9A which was a typical non–sagging detector module during that period can be seen in fig. 5.9. Clearly, the module was operated at an SNR around the working point with a negligible substrate spark rate, mostly below one spark per hour. Yet, the SNR of the module was not constant during the milestone period. The SNR shows an overshoot of up to 20 % in the first four days and a decrease after day 14. The same variation can be seen in the other 16 modules and is studied in detail in [18]. In fig, 5.10, it can be seen, that all modules have been operated at an SNR around the chosen working point.

To determine whether the modules were operating safely at the chosen working point, the strip loss and discharge rate on the various electrodes have been monitored. In fig. 5.11, the GEM discharges, substrate sparks and strip losses for all 17 modules can be found. In general one can say that the rate of discharges was negligible thus leading to the loss of only few strips. However, three exceptions have to be discussed:

- Module 2B was the one where the GEM was ripped off during assembly. Obviously, this module lost significantly more strips than the others. This may be attributed to the fact that chips of dried glue were left within the module when repairing the damage during assembly. Such particles within the detection volume could attract discharges, thereby weakening and finally destroying the surrounding strips. Indeed, in this module most strip losses occurred within the same region. Nevertheless, data from the module will be included in the results given.

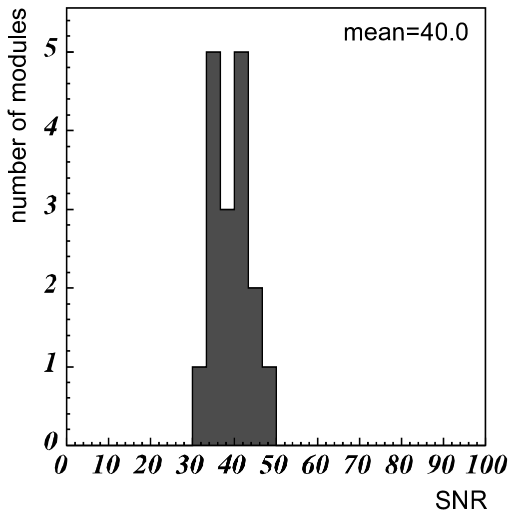

Figure 5.10: The SNR (averaged over the period from day 4 to day 14 where it was almost constant) histogramed for all substrates.

- Module 3B shows an outstandingly high substrate spark rate. Here the explanation is a short circuit in one HV group which developed during the hardening phase. It was not removed, since the milestone was to take place under LHC–like conditions where the tracker could not have been accessed at run–time. Within the damaged cathode group, the spark rate was substantially increased. Since that group was already useless, the discharges lead to no further strip losses. The remaining part of the substrate could still be operated safely and efficiently. Thus it can be concluded that MSGC+GEM detectors can be operated safely even if short circuits develop. This is a valuable discovery, since such defects are likely to occur in large scale experiments like CMS.

- One substrate in module 4A lost more than 40 strips, since it was badly cut and chips of gold were left on the substrate surface. This substrate should not have been used and thus the module is not considered further when discussing high rate capability of the MSGC+GEMs.

- For module 5A, the current monitor for the upper GEM was defect. The module did not show any substrate instabilities and did not loose any strips. Thus the module can be included into the analysis even without detailed information on the performance of the GEM.

In total, 16 out of the 18 mf2 modules are considered as part of the mf2 milestone. Within these, less than 0.14 % of the anode strips were damaged during the 376 hours of high intensity irradiation. Thus the milestone demands have been met.

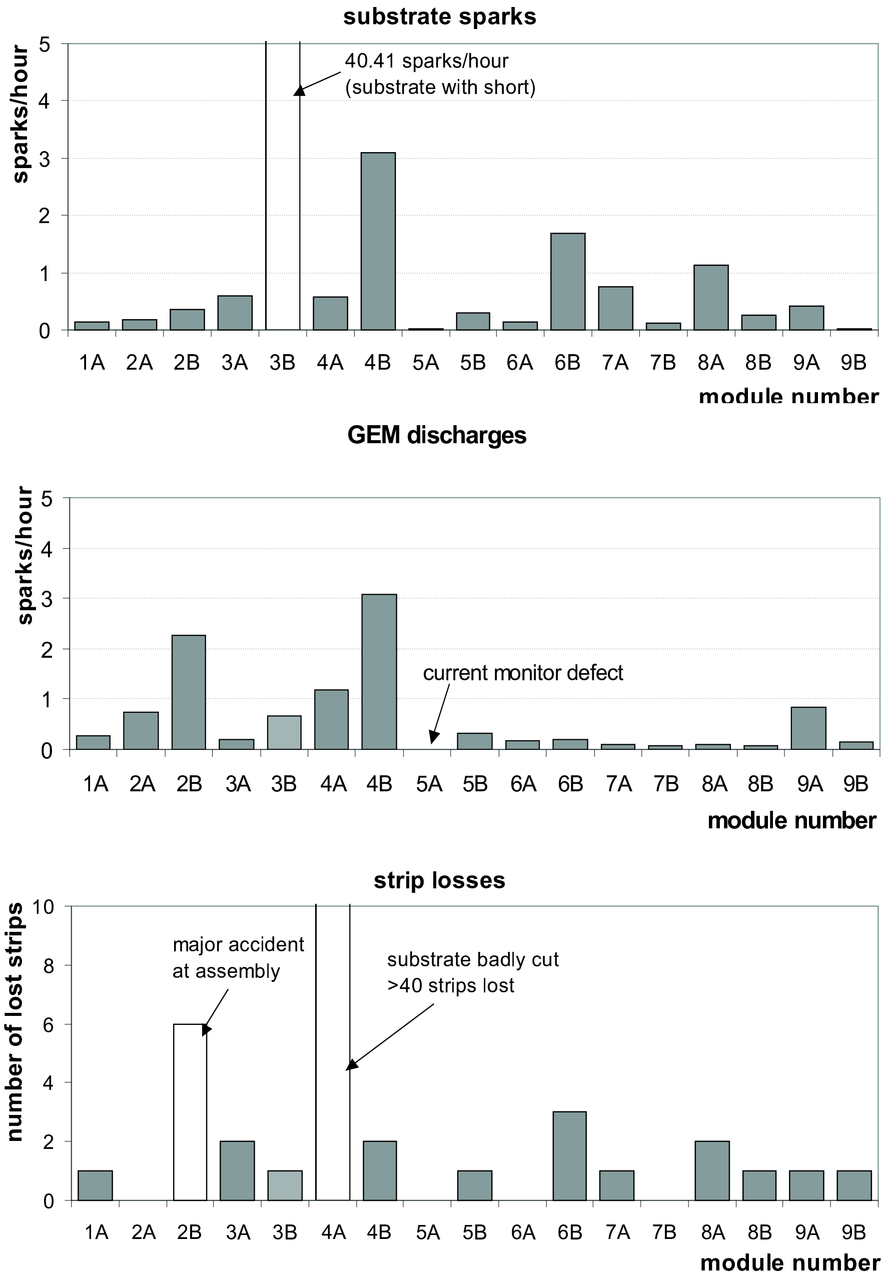

Figure 5.11: The rate of various discharges and the loss of strips for each module.

module	SNR	sparks per hour	hours of stay	SNR	sparks per hour	hours of operation
1A	61.0 ± 4.0	1.0 ± 0.9	55			
4B	48.3 ± 2.7	0.6 ± 0.1	46	72.1 ± 3.6	0.2 ± 0.6	17
5A	65.4 ± 4.8	0.01 ± 0.01	46	105.8 ± 3.6	0	17
5B	63.3 ± 4.1	0.4 ± 0.1	65			
9A	58.0 ± 6.0	0.12 ± 0.04	34	94.5 ± 9.5	0.75 ± 0.25	17
9B	68.6 ± 3.0	0	46	96.5 ± 3.4	0	17

Table 5.1: SNR and spark rate during the two phases of margin exploration.

5.6 The safety margin

Only six of the detectors were used for this part of the beam test. As described in the previous sections, not all modules were of equal quality. Thus only the modules which showed no obvious problems during assembly or operation will be regarded here. In addition, two detectors (2A and 3A) were used for voltage scans in parallel and thus could not participate in the margin study (see section 5.7.1).

The exploring of the margin was divided into two phases: First, the chambers were set to voltages that produced about 1.5–2 times the SNR of the previous working point. The chambers were kept there for one to two days before the voltages were further increased up to SNR ≈ 100 for some detectors. There the chambers remained for ≈ 17 more hours.

It was found that only four modules could be operate safely at the higher voltages after the first phase. Thus the two remaining detectors were left at their previous voltage settings for the last 17 hours.

Table 5.1 gives an overview of the two phases of the margin study for the six modules: The achieved SNR is given together with the spark rate and the duration of the operation at the defined settings. During the whole exploration of margins, only one strip was lost (in module 4B).

It can be seen, that all six detectors can be operated safely well beyond the chosen working point of SNR ≈ 37. Some detectors even went to almost 3 times that SNR without showing instabilities.

5.7 Detector uniformity

5.7.1 Comparison of the two GEM types

Until recently, the only source of GEM foils was the CERN workshop. Now with Würth Electronik, a second producer has been found [35]. Within this milestone, otherwise identical modules have been equipped with the two types of foils. Thus the two GEM types could be directly compared for the first time. To do so, several voltage scans have been performed with the Würth GEM (module 3A) and one of the CERN GEMs (module 2A). Since the Würth GEM is sagging over one substrate, only the other one is regarded here.

Two voltage scans were done, in which only U_{cath} was varied at two different transfer fields (3.4 kV/cm with $\Delta U_{GEM} = -335\ V$ and 5 kV/cm with

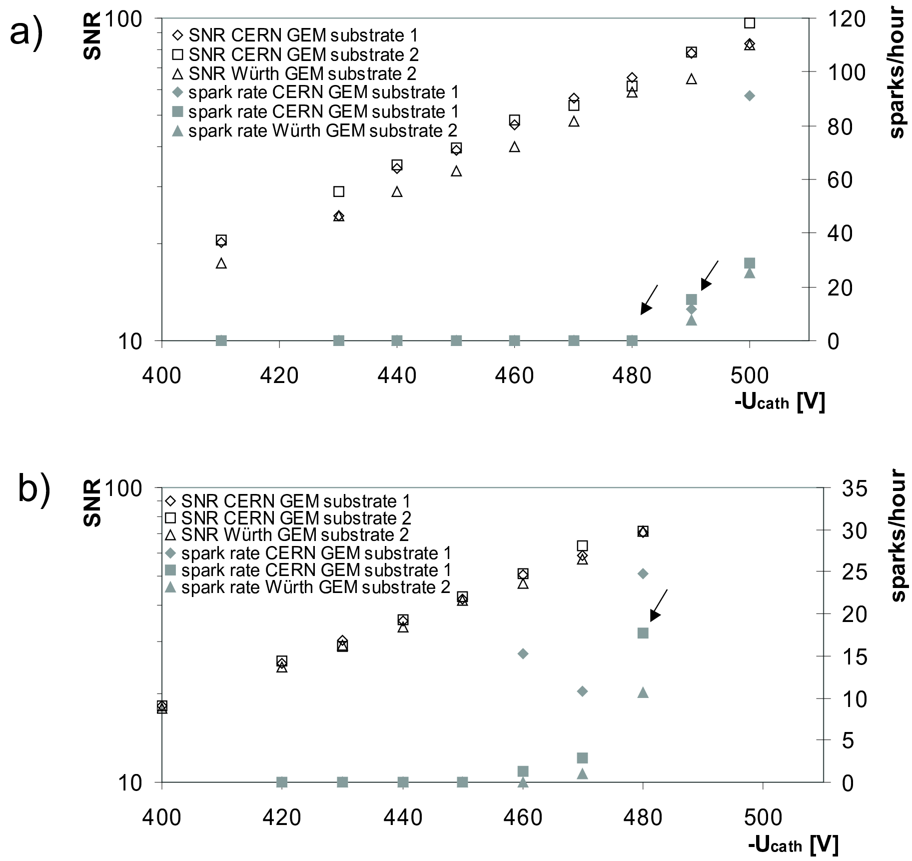

Figure 5.12: Spark rate and SNR as a function of U_{cath} when ΔU_{GEM} is fixed at (a)-335 V and (b)-320 V for transfer fields of (a)3.4 kV/cm and (b) 5 kV/cm. Strip losses are indicated by arrows.

$\Delta U_{GEM} = -320\ V$). In a third voltage scan, only ΔU_{GEM} was varied at a transfer field of 3.4 kV/cm and $U_{cath} = -450\ V$. During all voltage scans, E_{drift} was kept at 5 kV/cm. The SNR as a function of varying voltage was measured while running at low intensity. Later, the voltage scans were repeated at high intensity and the spark rate was recorded. In figures 5.12 and 5.13 the results can be seen.

In figure 5.12 (a) one can see that for the lower transfer field the sparking rate increased rapidly around $U_{cath} = -480\ V$ and several strips were lost. The GEMs however remained stable during the whole time at a discharge rate below one per hour. For the voltage scan at higher transfer field in fig. 5.12 (b), the cathode behaviour did not change much. On the other hand, the CERN GEM sparked with a significantly increased rate of around 12 discharges/hour while the Würth GEM remained stable and did not discharge during the whole voltage scan.

During the ΔU_{GEM}–scan, the substrates remained calm. The CERN GEM

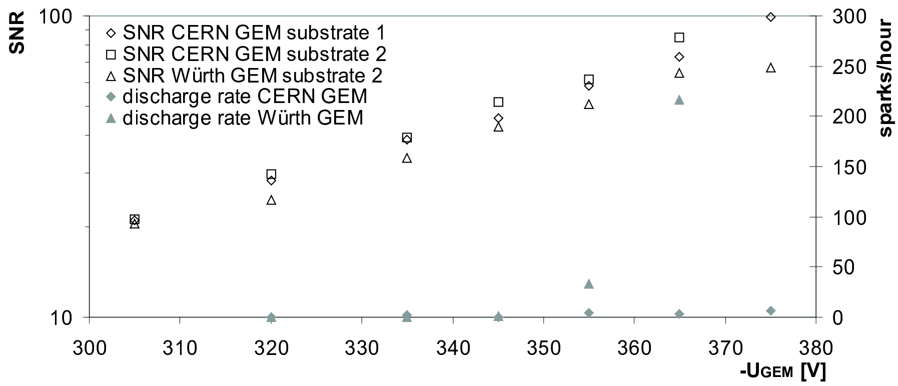

Figure 5.13: GEM discharge rate as a function of ΔU_{GEM} at $U_{cath} = -450\ V$.

in module 2A showed a good performance with the spark rate remaining below 10 discharges/hour until the end of the scan at $\Delta U_{GEM} = -375V$. On the contrary, the Würth GEM started discharging already at $\Delta U_{GEM} = -355V$ making the detector operation unstable.

From these voltage scans one can conclude that the CERN and Würth GEM foils have a comparable SNR. On the other hand, their stability in the various operation modes is quite different. The Würth GEM can work safely with higher transfer fields. Instead, ΔU_{GEM} is more limited than for the CERN GEM. The latter has to be attributed to the different etching processes used by the two manufacturers. The underetching in the Würth GEM (see chapter 3.3) clearly reduces the high voltage capability of the foil.

As a consequence optimised HV–configurations for the two GEM types have to be found separately. It remains to be seen whether the lower ΔU_{GEM} capability in the Würth GEM can be compensated by operating at higher transfer field and thus a higher a gain within the transfer gap.

The Würth GEMs may have room for improvement, since the foil built into module 3A was part of the very first series of GEMs ever produced in this size. Even so, chapter 5.7.2 will show that the Würth GEM is an equal to the CERN GEMs during the milestone, where operation at the chosen working point is concerned.

It should be mentioned here, that the performed voltage scans were not meant to prove the overall safety margin of the modules. This has to be done by optimising the distribution of gain between GEM foil, substrate and transfer field. In these tests, the stability of the three aspects has been studied separately.

5.7.2 Uniformity within the Aachen modules

With respect to a mass production of MSGC+GEMs it is of interest to compare the performance of the Aachen–built modules (1A, 2A–3B). Therefore two aspects can be considered:

- stability of operation during the milestone

module	ΔU_{GEM}	GEM discharges per hour	substrate	U_{cath}/V	scaled SNR	sparks per hour	strip loss
1A	-345V	0.27 ± 0.02	1	-445 to -450	1.00 ± 0.08	0.02 ± 0.01	1
			2	-445 to -450	1.09 ± 0.10	0.16 ± 0.02	0
2A	-335V	0.74 ± 0.04	1	-445 to -450	1.15 ± 0.09	0.13 ± 0.02	0
			2	-445 to -450	1.09 ± 0.11	0.03 ± 0.01	0
3A	-335V	0.19 ± 0.02	2	-455	1	0.13 ± 0.02	0
3B	-335V	0.66 ± 0.04	1	-450 to -455	1.12 ± 0.12	0.14 ± 0.02	1
			2	-450 to -455	1.26 ± 0.14	41.3 ± 0.33	0

Table 5.2: Working parameters for the Aachen modules during the milestone. Instead of absolute SNR, $\frac{SNR(regarded\ module)}{SNR(module\ 3A,\ substrate\ 2)}$ is given.

- comparability of detector gain

In the following discussion, the Aachen–built modules with sagging GEMs (module 2B and the second substrate of the Würth module 3A) will not be taken into account. The substrate with the short circuit will be included (module 3B, substrate 2). For each module the two substrates will be regarded separately.

Stability of operation during the milestone

During the milestone phase, the modules can be compared with respect to SNR, substrate spark rate, GEM discharge rate and strip loss. Determining the SNR of a module is not straight forward, since it varied significantly during the milestone phase (see fig. 5.9). Since, all substrates shared this variation, the ratio of the SNR of two substrates remains constant during the milestone[9] Thus the SNR will be scaled using substrate 2 of module 3A as a reference. For this module, the voltages remained constant during the whole milestone period making it the best choice for a reference detector.

In table 5.2, all parameters and results for the various substrates are listed. Obviously, the modules have been operated under very similar conditions with respect to voltage settings and thus SNR. They all showed good high rate performance with low spark rates and no more than two lost strips in total. However, the spark rates for different substrates and GEMs varies considerably. The differences can be accounted to slight variations in the quality of the material, especially in the GEM foil.

Comparability of detector signal

During the low intensity voltage scan which has been performed for modules 2A and 3A substrate 2 (see chapter 5.7.1), the other Aachen–built modules were kept at constant voltages. This allows to compare the signals of the modules directly. Instead of SNR, the cluster charge is used so that the different noise in the various PreMux128 chips is not taken into account.

[9] As a first approximation, the minor voltage modifications within the Aachen modules can be neglected.

module	substrate	scaled charge
1A	1	0.72 ± 0.09
	2	0.85 ± 0.08
2A	1	1.16 ± 0.07
	2	1.19 ± 0.10
3A	2	1
3B	1	0.79 ± 0.06
	2	1.09 ± 0.14

Table 5.3: $\frac{cluster\ charge(regarded\ module)}{cluster\ charge(module\ 3A,\ substrate\ 2)}$ for all substrates normalised to equal voltage settings.

Since the modules were not operated at the same voltage settings, the cluster charge is scaled using the second substrate of module 3A as a reference again. With the help of the voltage scans, the cluster charge of this module can be extrapolated for all voltage settings.

The scaled cluster charges can be seen in table 5.3. One can see that the gain varies up to ±25 % for the 7 substrates.

These differences may be due to variations within the GEM geometry [33]. Module 2A shows the highest signal, an effect that could be caused by smaller GEM holes. For that module, more evidence for GEM holes with a reduced diameter was found and will be presented in chapter 6.

5.8 Conclusion

During the beam test at PSI, 16 modules out of the 18 assembled have clearly met the milestone demands. They have been safely operated under LHC–like conditions for 20 days with less than 0.14 % of the readout channels damaged. Thus they have proven their capability to equip the CMS outer tracker. In addition, it could be shown, that in high rate experiments Würth Elektronik GEMs are an alternative for the use of CERN–built GEMs.

Chapter 6

Signal shaping and detector transparency

An MSGC+GEM detector has various operation parameters that need to be optimised. Among them are the transfer– and drift field. Within this chapter, the dependence of the signal, shaping and transparency on the field configuration will be discussed.

6.1 Laboratory test setups

Within this section, laboratory tests with single detector modules are described. For irradiation, a Sr^{90} source was used that was placed above the tested module. A scintillator below the module served as trigger.

For the tests described, two different types of readout electronics have been used: PreMux128 (see appendix D) and APVM [40] (see appendix E). The results obtained with both readout chips are comparable, since they have the same preamplifier.

Two different DAQ[1] systems were required. They will be described in the following two sections.

6.1.1 PreMux128 readout system

A scheme of the PreMux128 DAQ used in Aachen [21, 30] can be seen in figure 6.1. As in the system described in chapter 5, the modules are read out via a combination of SBM and wing.

The readout sequence is controlled by a sequencer while the analogue data is read out by an FADC via a so–called adapter board [30]. This board provides the means to generate a trigger signal from a coincidence of up to four scintillators. In addition an automated delay scan can be conducted. The power supply for the SBM is also provided through the adapter board.

Both, the adapter board and the SBM may be programmed by CAOs[2].

[1] **D**ata **Acq**uisition System
[2] **CA**MAC **O**utput registers

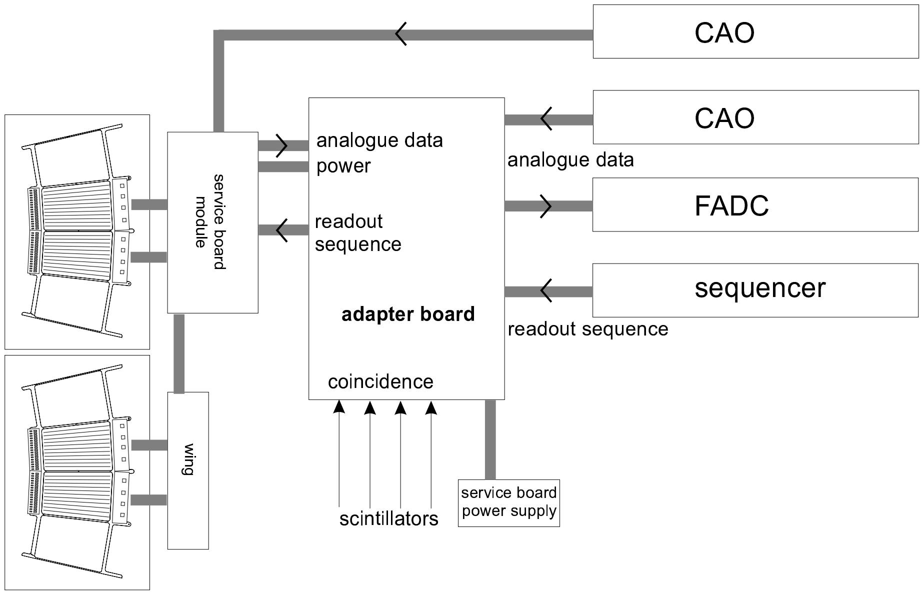

Figure 6.1: Scheme of the PreMux128 DAQ setup used in Aachen.

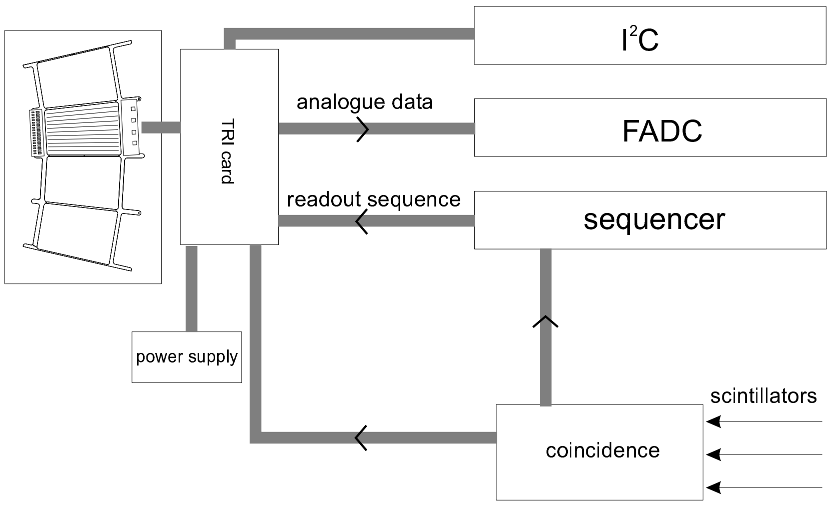

Figure 6.2: Scheme of the APVM DAQ setup used in Aachen.

6.1.2 APVM readout system

A scheme of the Aachen APVM readout [22] can be seen in figure 6.2.

For the APVM chip, the SBM and wing is to be replaced by several so–called TRI cards. Each of them can be used to read out one APVM hybrid. However, the four APVM chips on the hybrid can not be multiplexed but have to be read out separately. The TRI card is directly addressed by the sequencer and the FADC. The power for the TRI card is provided by a separate power supply. The programming of the APVM chip is performed via an I^2C interface.

The trigger can again be generated by coincidence of up to four Scintillators.

6.1.3 Detectors under test

All five Aachen–built detector modules have been used in the laboratory tests. For some of them, the PreMux128 readout electronics was replaced by APVM hybrids. The new configuration of the five modules was the following:

1A: CERN GEM with PreMux128 readout electronics.

2A: CERN GEM. Only one substrate was read out using APVM electronics.

2B: CERN GEM with PreMux128 readout electronics. This module was known to have a sagging GEM since the burn–in.

3A: Würth GEM. Only the substrate below the non–sagging GEM was read out using APVM electronics.

3B: CERN GEM with PreMux128 readout electronics.

6.1.4 Gas mixtures

For the measurements described in this chapter, the following three gas mixtures were used:

Ne/DME 40:60 This gas was foreseen for the CMS experiment. This choice was mainly motivated by the small Lorentz angle of the gas mixture and the low voltages required to achieve efficient operation [27]. As can be seen in figure 3.4, it has a comparably low drift velocity that reaches a plateau for electric fields above 5 kV/cm.

Ne/DME/CO_2 40:40:20 This gas was considered an improvement of pure Ne/DME by adding 20 % of CO_2 to increase the drift velocity [27].

Ar/CO_2 70:30 This gas is used in the HERA b Experiment. It's main advantage compared to Ne/DME is that it is non–flammable and thus safer to handle. In addition, figure 3.4 shows that it has a significantly higher drift velocity that already reaches it's plateau at $E \approx 2$ kV/cm.

6.2 Signal shape and drift field

The drift velocity plays an important role in the detector performance (see section 6.2.1). For the fast readout electronics used for the mf2 modules, the choice of an appropriate gas mixture is essential.

Delay scans with varying drift fields have been performed for all three gases. Therefore the time between trigger and signal readout was varied. For every delay time, the cluster charge was determined and plotted (see figure 6.4). Thereby the shape of the preamplified detector signal was reproduced. All delay scans were scaled in a way that the maximum cluster charge is 1. The time at which the maximum is reached is called peaking time.

For the two readout systems used, no absolute delay between trigger and time of readout was known. Especially the relative offset of the delay between the PreMux128 and APVM DAQ was unknown.

An absolute time scale for the delay curves was defined by measuring a delay curve with each system under identical conditions and determining the shift. The offset for both setups was then chosen in a way that the peaking time for both delay curves was 0. For a faster operation mode of a detector, this leads to negative peaking times.

The results of the delay scans will be described in sections 6.2.2 and 6.2.3.

6.2.1 Delay curve calculations

To understand the process of signal formation, one has to distinguish between the 'detector shaping' and the 'electronic shaping'. The two processes will be described in the following:

Detector shaping: The detector shaping describes the formation of the signal that is induced on the anode strips of a detector.

That signal is created by avalanche electrons as well as by ion feedback near the anode strip. The length of the signal is dominated by the drift of the primary electrons in the drift space. Still, the major part of the signal charge is induced by the ions within the avalanche that drift away from the anode strip.

The average signal can be calculated[3]. The results for three different cases can be seen in figure 6.3 (a):

1. If only the signal from the electrons is considered in the simulation, a constant electron current is detected while the electrons from the drift space arrive on the anode strip.

   Consequently the length ΔT of the signal is given by the drift velocity v_{drift} within the drift space and the thickness d of that space:

$$\Delta T = d/v_{drift}$$

   This case is shown in figure 6.3 (a) for a high drift velocity.

[3]This was done with the help of a LabView simulation program provided by Tom Beckers, Universiteit Antwerpen (UIA), Antwerpen, Belgium.

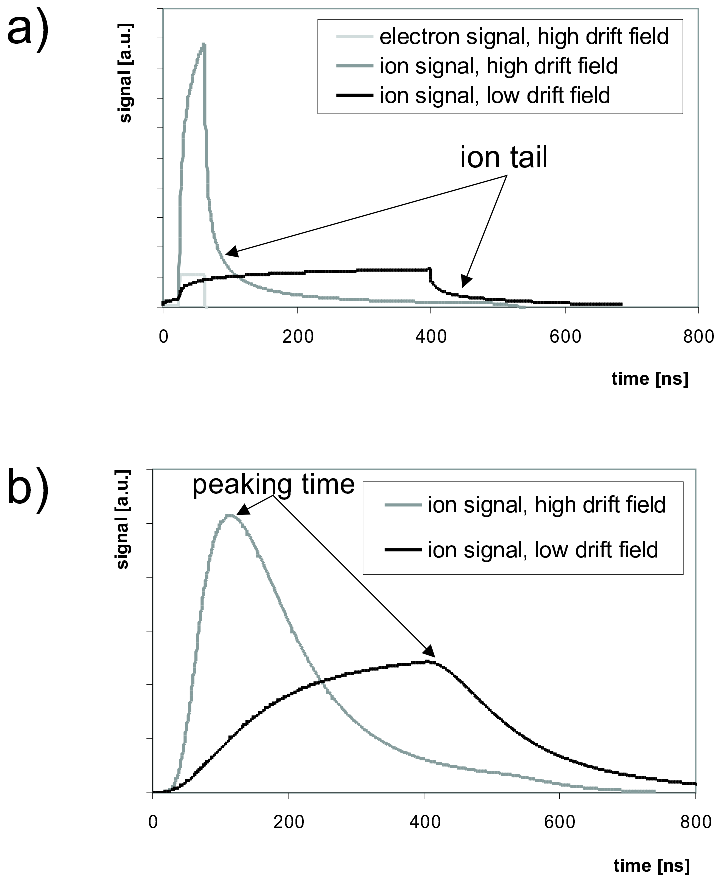

Figure 6.3: The detector signal before (a) and after (b) the electronic shaping for two different drift velocities in the drift space. For the higher drift velocity, the signal with and without the contribution of the ion feedback near the anode is shown.

2. If the ion feedback is included into the simulation, the amplitude of the signal is significantly increased.

   In addition, the edges of the signal curve are smoothed. After the termination of the electron drift, the slower ions are still close enough to the anode strip to induce a detectable signal. This manifests as an ion tail that can also be seen in figure 6.3 (a).

3. For lower drift fields and thus lower drift velocities, the signal is spread over a longer time. If the total detector amplification remains constant, the signal amplitude is reduced. However, the ion tail is the same as for a high drift velocity in the drift field since the conditions in the transfer field are unchanged.

Electronic shaping The shape of the detector signal is altered during the preamplification by the shaper of the readout chip.That process is called electronic shaping.

The impact of the electronic shaping on the two latter cases described above can be seen in figure 6.3 (b).

For the higher drift velocitiy, the signal shape is dominated by the CR–RC shape of the amplifier. In the case of low drift velocity on the other hand, the shape approaches that of the detector signal. Consequently, the peaking time is increased.

For the 50ns shaping constant of the APVM and PreMux128, the height of the signal is reduced for low drift velocities. This decrease can be described by the so–called ballistic coefficient (see also appendix F) that is defined as:

$$ballistic\ coefficient = \frac{S}{S_{delta}}$$

where S is the signal seen by the readout electronics and S_{delta} is the signal that would have been seen if the input charge had arrived in a delta pulse.

6.2.2 Delay curve measurements

All measurements described in this section have been performed with module 2A.

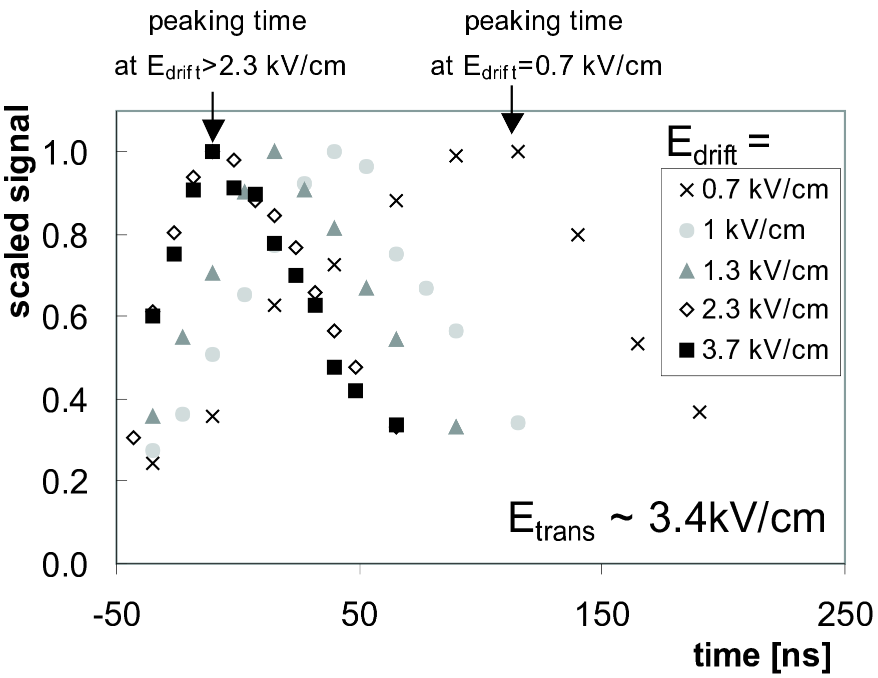

Figure 6.4: Some delay curves as obtained in Ar/CO_2.

The drift field should mainly influence the length of the rising edge of the detector signal leading to a shift of the signal maximum in time (peaking time) as can be seen in figure 6.4 for Ar/CO_2. The shift of the peaking time however is only a side effect of the longer rise time. Thus the delay curves are better displayed by superimposing their maxima so that the curve shapes can be compared more easily.

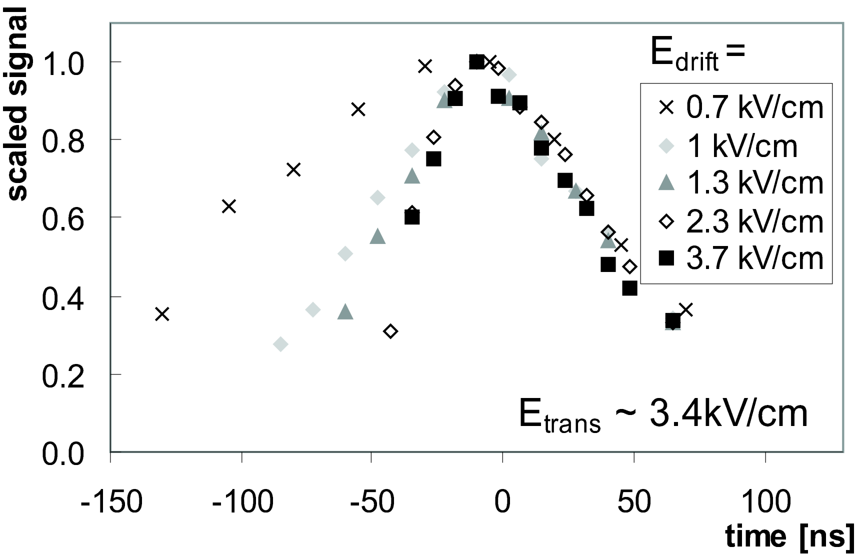

Figure 6.5: Delay curves for Ar/CO_2 with the maximum of each curve superimposed.

The modified version of figure 6.4 can be seen in figure 6.5. There it becomes clear, that the falling edge of the delay curve is not affected by the drift field setting. The rising edge however is longer for lower fields.

As mentioned before, the drift velocity in Ar/CO_2 increases up to drift fields of about 2 kV/cm reaching a plateau for higher field settings. Consequently, the shapes of the delay curves do not depend on the field settings for higher E_{drift} as can also be seen in figure 6.5.

A series of delay scans for Ne/DME can be seen in figure 6.6. For this gas, the drift velocity reaches it's plateau for much higher fields than in Ar/CO_2. As a consequence, the shape of the delay curve remains unaffected by the drift field only for $E_{drift} > 5\ kV/cm$.

The drift velocity in $Ne/DME/CO_2$ is almost equal to that in Ne/DME. Thus, the delay curves in the double and triple gas mixture are almost identical as can be seen by comparing figure 6.6 to figure 6.7.

Figure 6.8 shows a comparison of the delay curves taken on the drift velocity plateau in all three gas mixtures. There it is even more obvious, that for the two DME based gas mixtures the signal shape is the same. For the much faster Ar/CO_2 on the other hand, the rise time is noticeably shorter.

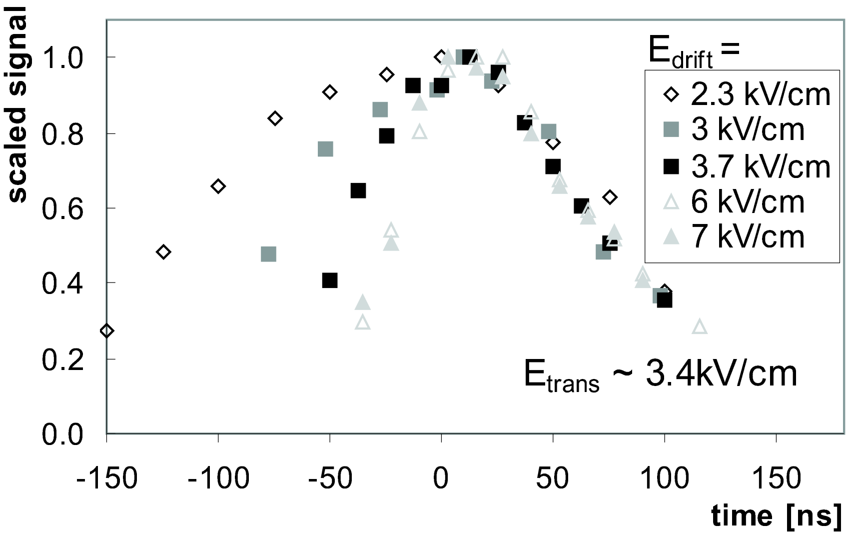

Figure 6.6: Some delay curves in Ne/DME.

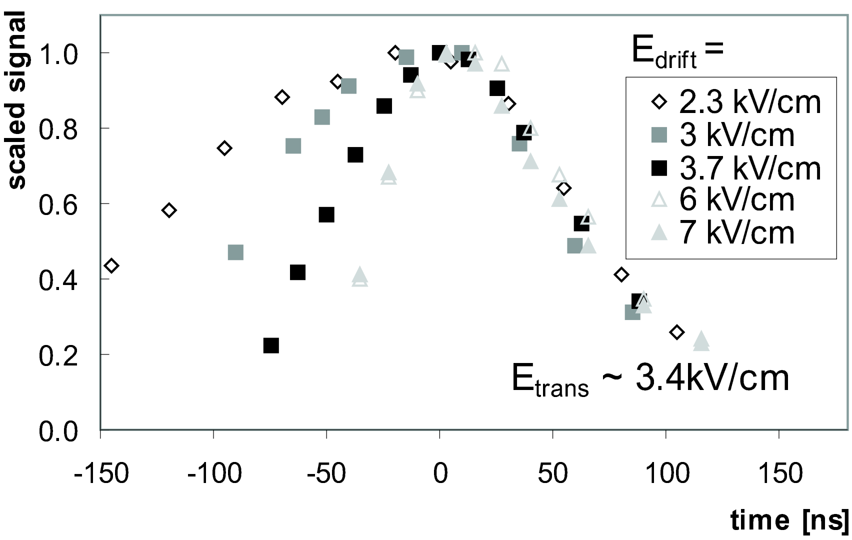

Figure 6.7: Some delay curves in Ne/DME/CO_2.

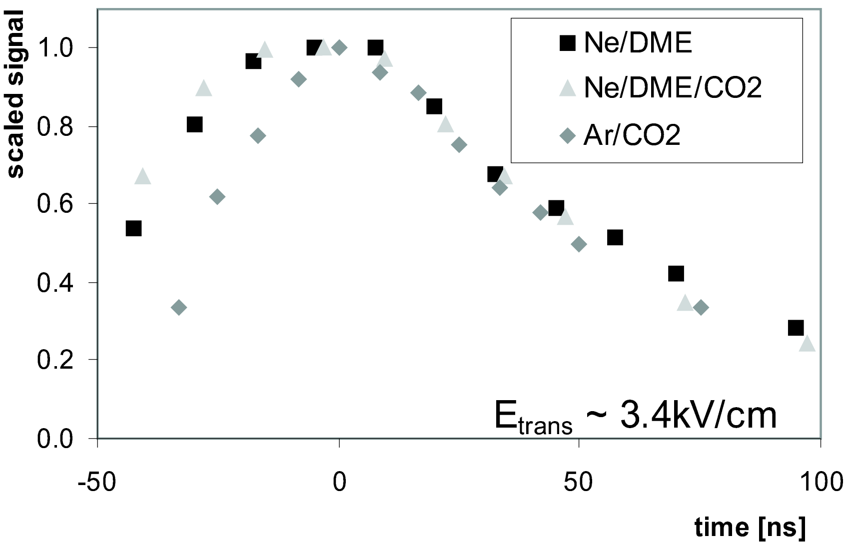

Figure 6.8: Comparison of the delay curves on the drift velocity plateau for the three gas mixtures.

Peaking time and ballistic coefficient

For the laboratory tests described, the comparison of the three gas mixtures is considerably simplified, if the peaking time of each delay curve is used. The dependence of the peaking time on the drift field in all three gases is plotted in figure 6.9. Again, it can be seen, that Ne/DME and Ne/DME/CO_2 show almost identical behaviour. For both gas mixtures, the peaking time is stable down to $E_{drift} \approx 5\ kV/cm$. Below that drift field, the peaking time increases due to the decreasing drift velocity in the drift field.

Ar/CO_2 clearly shows a lower peaking time on the drift velocity plateau than the DME based gas mixtures. In addition, the peaking time is stable down to drift fields of about 2 kV/cm.

As explained in section 6.2.1, the shifted peaking time at low drift velocities is accompanied by an increased ballistic coefficient. This will lead to a decrease of signal for $E_{drift} < 5\ kV/cm$ in the DME based gas mixtures and $E_{drift} < 2\ kV/cm$ in Ar/CO_2.

6.2.3 Identification of a sagging GEM through the delay

For a sagging GEM, the drift distance is changed with respect to the non–sagging modules. Consequently, the drift field is not the same for identical voltage settings. Thus it should be possible to identify a sagging GEM by comparing the shift of peaking time for low $U_{GEM\ up} - U_{drift}$ to that of a good module. Indeed, the first evidence for a sagging GEM was a shift of the peaking time. Within this section, the effect will be investigated systematically.

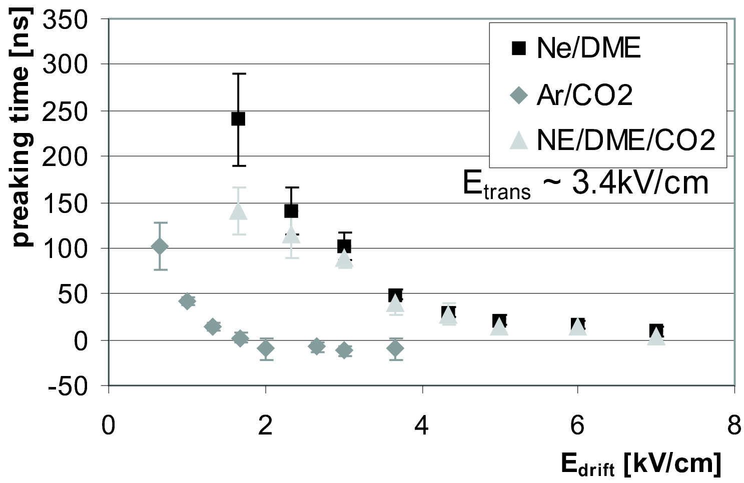

Figure 6.9: The dependence of the peaking time on the drift field in all three gas mixtures.

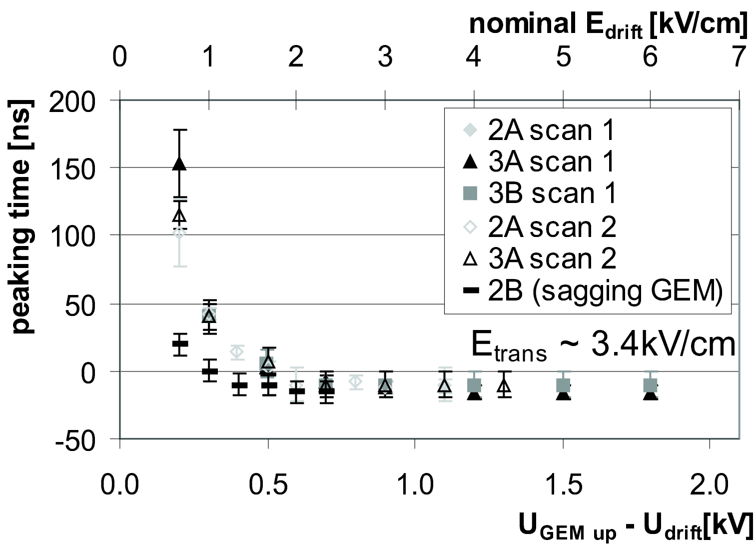

Figure 6.10: Peaking time vs. $U_{GEM\ up} - U_{drift}$ in Ar/CO_2 for several non–sagging detectors and the module 2B with the sagging GEM. For some of the modules, more than one delay scan is displayed. The potential difference between upper GEM side and drift cathode and the nominal drift field are given on two separate axes, since measurements for a sagging GEM are included. There the distance between GEM foil and drift cathode is not known and thus no electric field can be calculated.

The delay scans described for module 2A have been repeated for the other detectors. In most cases, it was found that the curve shape obtained for module 2A could be reproduced for the GEMs where no sag had been discovered during the functionality test[4].

To compare the performance of the different detector modules, the peaking times of the several scans are shown in figure 6.10.

The measurement of the peaking time was also done for the GEM that is sagging towards the drift cathode (module 2B). As expected, a significant shift of the thus obtained curve with respect to the other modules is observed (see also figure 6.10). The peaking time of module 2B is stable down to $U_{GEM\ up} - U_{drift} =$ 0.4 kV instead of 0.6 kV as for the other modules.

6.3 Detector signal, transparency and drift field

As discussed in chapter 3.3, GEM transparency is an important feature of all GEM type detectors. Within this section, transparency measurements for the five Aachen–built modules will be presented.

6.3.1 The Würth GEM

The dependence of the transparency on the drift field was measured for the Würth GEM in the three gas mixtures under test. Therefore the drift field was varied and the cluster charge of the signal recorded. The results can be seen in figure 6.11. Here the signal is scaled so that the maximum is 1. The solid lines have been added to guide the eye.

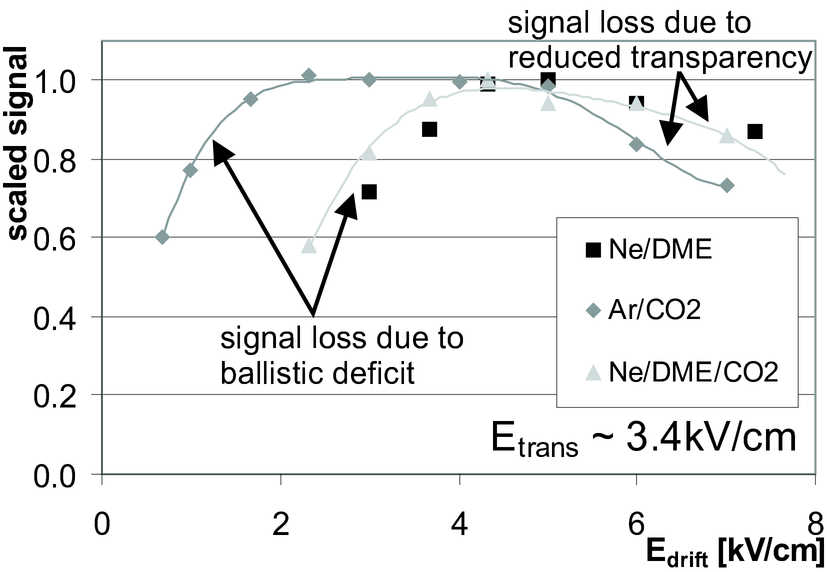

Figure 6.11: Transparency curves for the Würth GEM in three gases.

[4]Exceptions will be discussed in section 6.3.2

In the Ar/CO_2 gas mixture, a plateau of maximum signal (and therefore maximum transparency) is observed that ends at $E_{drift} > 4\ kV/cm$. For drift fields below 2.3 kV/cm, a drop of signal can be observed that is due to a decreasing ballistic coefficient. Consequently, the transparency at lower fields can not be determined.

In the DME based gas mixtures, the decrease of signal at low fields already starts at $E_{drift} = 4\ kV/cm$ as expected from the peaking times seen in figure 6.9. As a consequence, no transparency plateau is observed here.

For high drift field, the signal decrease in the DME based gas mixtures is significantly lower than for Ar/CO_2. This can be attributed to signal loss due to attachment in Ar/CO_2 which starts to play a role above electric fields of 5 kV/cm (see figure 3.2).

The loss of signal due to attachment can be corrected for as described in chapter 3. The results are presented in figure 6.12. It turns out, that the signal drop due to transparency loss at high E_{drift} is the same for the three gas mixtures. Thus it can be concluded that the Würth GEM can be operated at maximum signal and transparency for all three gas mixtures.

A Würth GEM of comparable geometry had already been tested in [35]. There, an even longer transparency plateau had been observed.

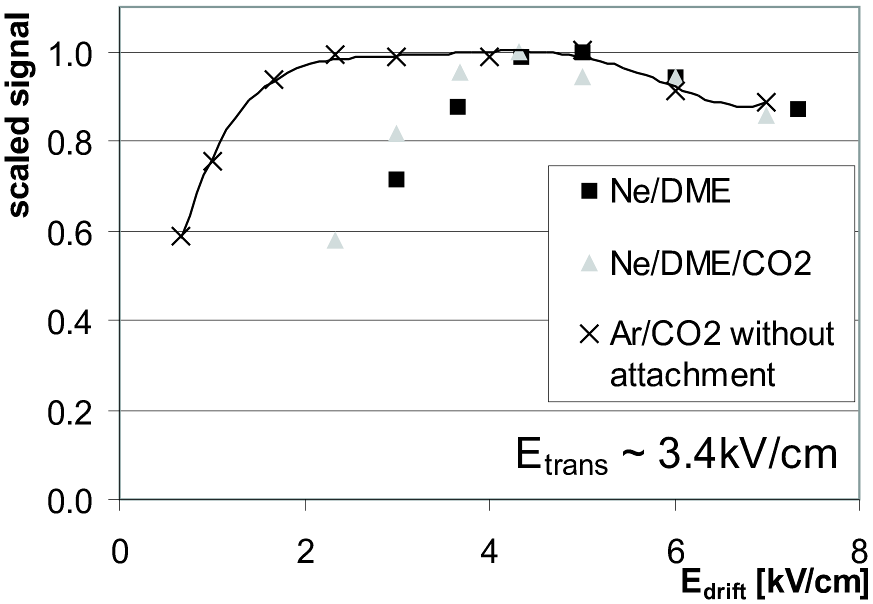

Figure 6.12: Transparency curves for the Würth GEM with the Ar/CO_2 data corrected for the attachment loss.

6.3.2 The CERN GEMs

The Würth and CERN GEM have almost the same optical transparency (34 % and 33 % respectively). However, the different shape of the hole tubes may lead to quite different transparency plateaus. Within this section, a comparison between the two GEM types will be drawn. In addition, the uniformity of the CERN GEMs will be investigated.

Current and Sr^{90} measurements

The transparency of module 1A has been investigated by G. de Lentdecker [5]. He measured the current induced by a γ ray gun that produces 8.3 keV photons at a flux of 10^5 Hz/mm^2 to obtain transparency information [23].

For a high flux of γ rays, the substrate of an MSGC+GEM draws a current of the order of a few 100 nA. The total current depends on the irradiation flux and the gain of the module. For a constant irradiation rate, the substrate current is proportional to the detector signal. Therefore the substrate current measurements can be directly compared to the Sr^{90} tests that were performed in Aachen.

In the γ ray measurements, scans of substrate current vs. drift field were made in the Ne/DME and Ar/CO_2 gas mixtures.

The result can be seen in figure 6.13. A curve obtained in Aachen with Ar/CO_2 using a Sr^{90} source and PreMux128 electronics to scan the same module is added. In this way the two types of transparency measurement can be compared directly.

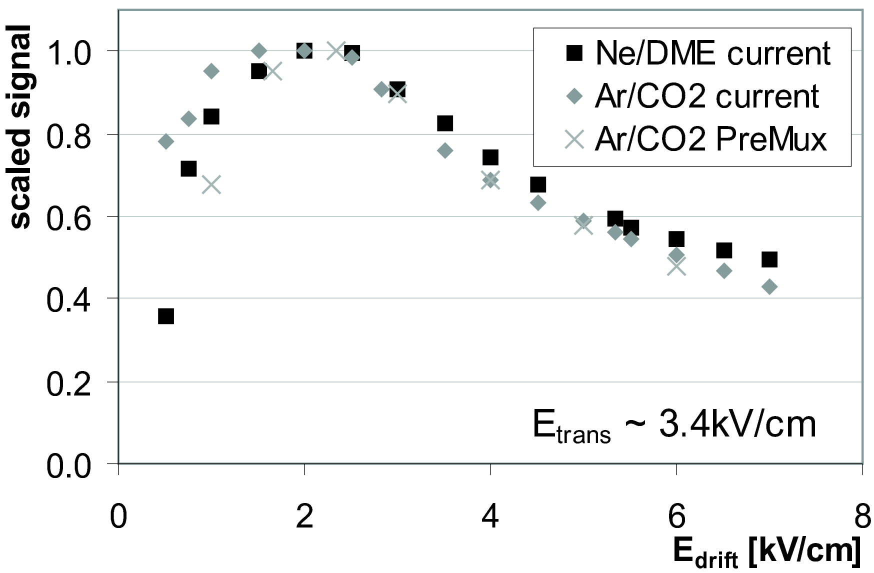

Figure 6.13: Detector signal vs. drift field obtained with current measurements [23] and PreMux128 electronics. The current measurements were performed in two gas mixtures whereas only Ar/CO_2 is shown for the PreMux128 curve.

[5]Universite Libre de Bruxelles, Belgium.

The signal decreases for drift fields above $E_{drift} = 2.3 \pm 0.3\ kV/cm$. In addition, a decrease of signal for low fields can be seen in both types of measurements.

In the case of the PreMux128 measurements, the latter decrease can be accounted to the decreasing ballistic coefficient. For the current measurement, is studied in [18]. In this case, the decrease of signal is accounted to charging of the GEM foil.

The decrease at $E_{drift} = 2.3 \pm 0.3\ kV/cm$ has to be accounted to a decrease of transparency. Obviously, the transparency of a CERN-GEM starts decreasing at much lower fields compared to the Würth GEM.

For the current measurements, the signal remains at it's maximum for less than 1 kV/cm of drift field variation, showing a short transparency plateau. For the PreMux128 measurement, the transparency plateau is not observed.

It can be concluded, that the current measurements in both gas mixtures and the Sr^{90} measurements in Ar/CO_2 give comparable results when measuring the decrease of transparency at high drift fields. The end of the transparency plateau at low drift fields can be observed neither in current– nor in PreMux128 measurements.

Comparison of three gas mixtures

Looking at figure 6.11, it can be seen, that the signal starts decreasing below a drift field of E_{drift} ≈4 kV/cm in the DME–based gas mixtures. This could be accounted to a decreasing ballistic coefficient.

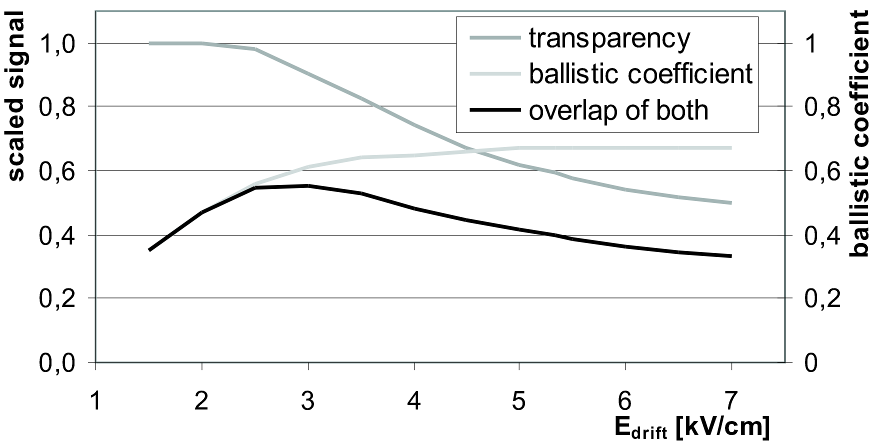

Figure 6.14: Effect of the transparency and ballistic coefficient on the detector signal. In the DME based gas mixtures, the two effects should overlap when using PreMux128 or APVM readout electronics. The transparency is derived from the current measurement whereas the ballistic coefficient was determined using the LabView program.

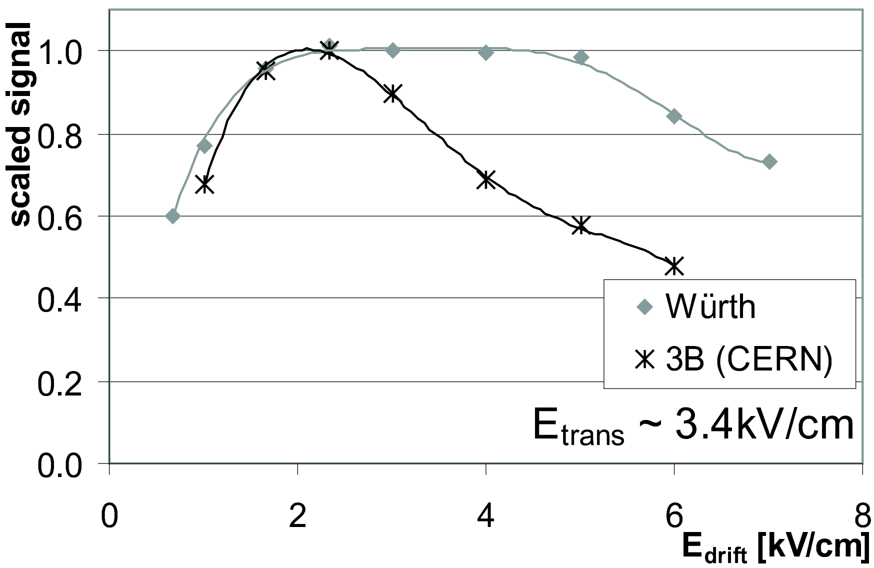

Figure 6.15: Transparency curves for the Würth GEM and CERN GEM in Ar/CO_2.

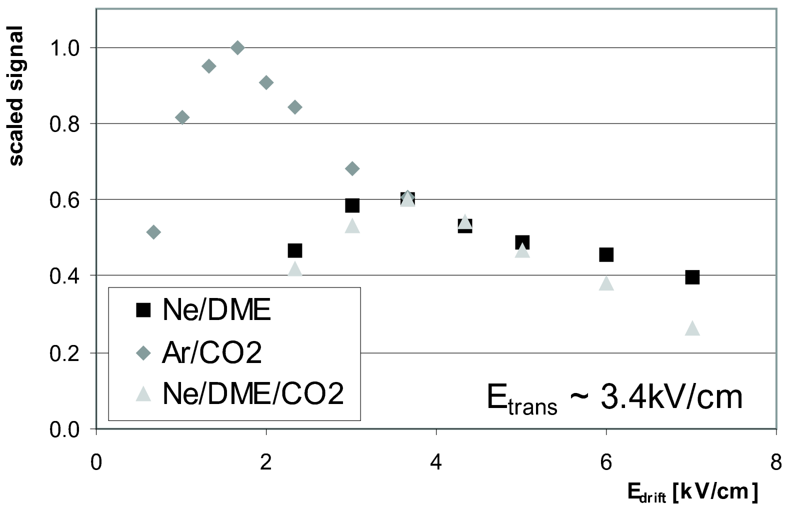

Figure 6.16: Detector signal vs. drift field in the three gas mixtures. In the slower DME based mixtures, the signal has been scaled in a way, that the loss of transparency in the maximum can be seen.

For the CERN GEMs, the transparency starts decreasing already at $E_{drift} > 2.3\ kV/cm$. Thus an overlap of the two effects is expected when measuring the dependence of the detector signal on the drift field in these gases for a CERN GEM (see figure 6.14).

On the other hand, this overlap does not play a role in Ar/CO_2 as can be seen in figure 6.15. There the transparency measurements for Würth– and CERN GEM are compared. The signal maximum is reached at $E_{drift} = 2.3\ kV/cm$ for both detectors. At lower fields, the decreasing ballistic coefficient reduces the measured signal. The decrease of transparency starts above $E_{drift} = 2.3\ kV/cm$ fields for both GEM types.

The Sr^{90} measurements for module 2A in the three gas mixtures can be seen in figure 6.16 with the maxima of the scans in DME based gases scaled to match the Ar/CO_2 scan. Indeed a shifted maximum of signal for DME based gas mixtures is observed. In Ar/CO_2 the signal shows a decrease at a drift field below 2 kV/cm. The maximum of signal in the DME based gas mixtures however, is shifted to $E_{drift} = 3.7 \pm 0.3\ kV/cm$.

Since the detector transparency is unaffected by the gas mixture (see current measurements in figure 6.13), the shift has to be accounted to the overlap of decreasing transparency and ballistic coefficient. As a consequence, the CERN GEMs can not be operated on the transparency plateau in DME based gas mixtures.

The effect of the ballistic coefficient can be reduced by readout electronics that has a larger shaping constant. Therefore, the shaping constant of the APVMs in module 2A was increased and the Ne/DME measurement was repeated. The result can be found in figure 6.17 compared to a measurement with a shaping constant of 50ns. Indeed, the maximum of the signal is shifted to lower E_{drift} for the higher shaping constant.

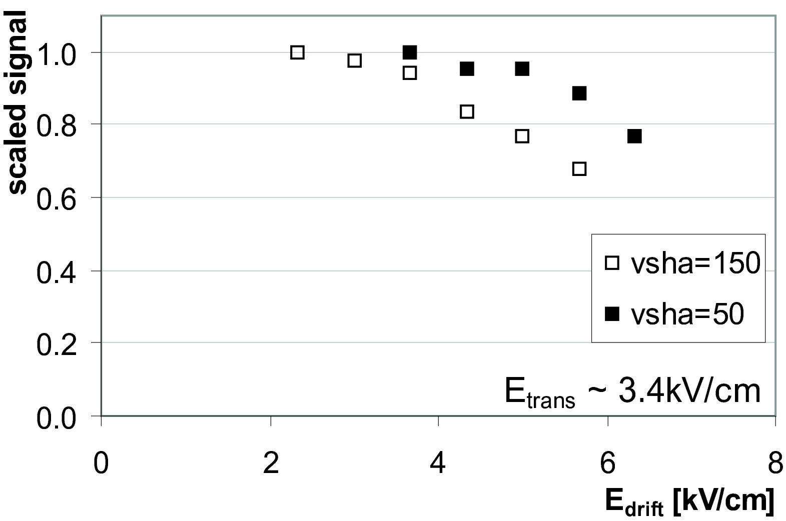

Figure 6.17: Signal vs. drift field in Ne/DME for two different shaping constants. The signal is again scaled to be 1 at the maximum.

It can be concluded that DME based gas mixtures are not well adapted to the fast shaping of the PreMux128 and APVM electronics in case of the CERN GEMs. On the other hand, Ar/CO_2 is suited to operate at maximum transparency with PreMux128 and APVM electronics in peak mode even for the reduced transparency plateau of the CERN GEMs.

Consequently, a gas with a drift velocity that remains on the plateau down to low electric fields, should be used in high rate experiments like HERA b and CMS where fast shaping is required.

Transparency measurements in Ar/CO_2

As shown in the previous section, it is not possible to measure the transparency of a CERN GEM directly with Ne/DME or $Ne/DME/CO_2$ using PreMux128 or APVM electronics.

Since the PreMux128 measurements with Ar/CO_2 match with the current measurements, this gas mixture can be used to determine transparency with the Aachen setup. Consequently, only Ar/CO_2 results will be presented within this section.

Figure 6.18 shows the transparency curves for all four modules equipped with a CERN GEM[6]. There it can be seen, that not all modules show the same decrease in transparency. Instead, the following behaviour is observed:

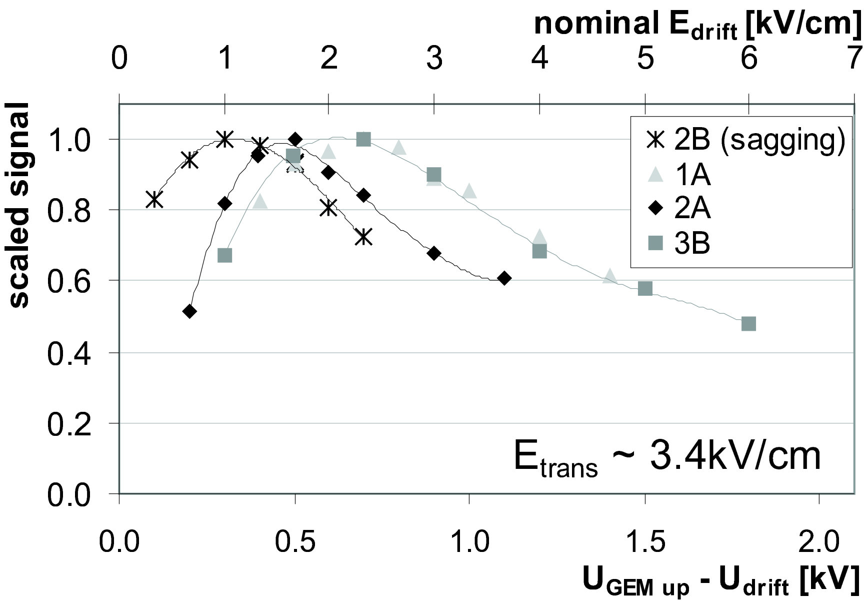

Figure 6.18: Comparison of the transparency curves of the four CERN GEMs

[6]Alike in figure 6.10, no drift field information is available for module 2B due to the GEM sag. Thus, $U_{GEM\ up} - U_{drift}$ is given on the primary axis whereas the drift field for the other modules is shown on the secondary axis.

- Detector 1A and 3B show similar results. For those two, the transparency starts decreasing at $E_{drift} = 2.3 \pm 0.3\ kV/cm$.
- For detector 2A, the maximum of signal is found for a drift field below 2 kV/cm.
- For module 2B, a decrease of signal at lower $U_{GEM\ up} - U_{drift}$ is expected because of the sagging GEM. Since the foil is sagging towards the drift cathode, the same $U_{GEM\ up} - U_{drift}$ will lead to a higher drift field and thus a lower transparency. This behaviour is indeed observed in figure 6.18.

For module 2A, the difference in the transparency was not expected and has to be investigated further. Therefore several transparency scans were performed for all modules except 2B for different positions of the Sr^{90} source above the substrates. The results will be presented in the following.

Module 1A: For module 1A, six field scans were performed across both substrates. The results can be seen in figure 6.19 (a) together with the current measurement from figure 6.13. The corresponding peaking times are shown in figure 6.19 (b).

For the peaking time data in figure 6.19 (b), a reference scan (taken from figure 6.10) performed with module 2A is added. Thus, the peaking time of a non–sagging GEM can be compared to the data of module 1A. For three of the delay scans that were taken with the source placed above one substrate, no variation in the peaking time can be seen. In the scans made above the other substrate, however, the peaking time starts increasing already at higher drift fields. From these scans, a sag of the GEM towards the substrate can be deduced.

The seven transparency curves are in good agreement. No variation due to the GEM sag can be observed. Most likely, the sag is so small, that it has no noticeable impact on the transparency.

Module 2A: For module 2A, the drift field scans were repeated on 3 positions across the substrate that was read out via APVM. The result can be seen in figure 6.20. Obviously, the shape of the transparency curve can be reproduced in all three cases. The peaking times also were the same for all scans, so that a GEM sag can be excluded as an explanation for the early transparency decrease.

An alternative explanation may be a reduced diameter of the GEM holes due to an error in the GEM etching. Smaller holes would lead to a reduced optical transparency and thus reduce the transparency plateau of the module [19]. However, to verify this, the module will have to be opened to measure the size of the GEM holes. This could not be done up to now.

Module 3B: Finally, the results for detector 3B can be found in figure 6.21. The delay in Figure 6.21 (b) shows the characteristic shift in the peaking time for one source position. Thus a GEM sag towards the drift cathode can be deduced at that place. Consequently, the transparency decrease starts at lower $U_{GEM\ up} - U_{drift}$.

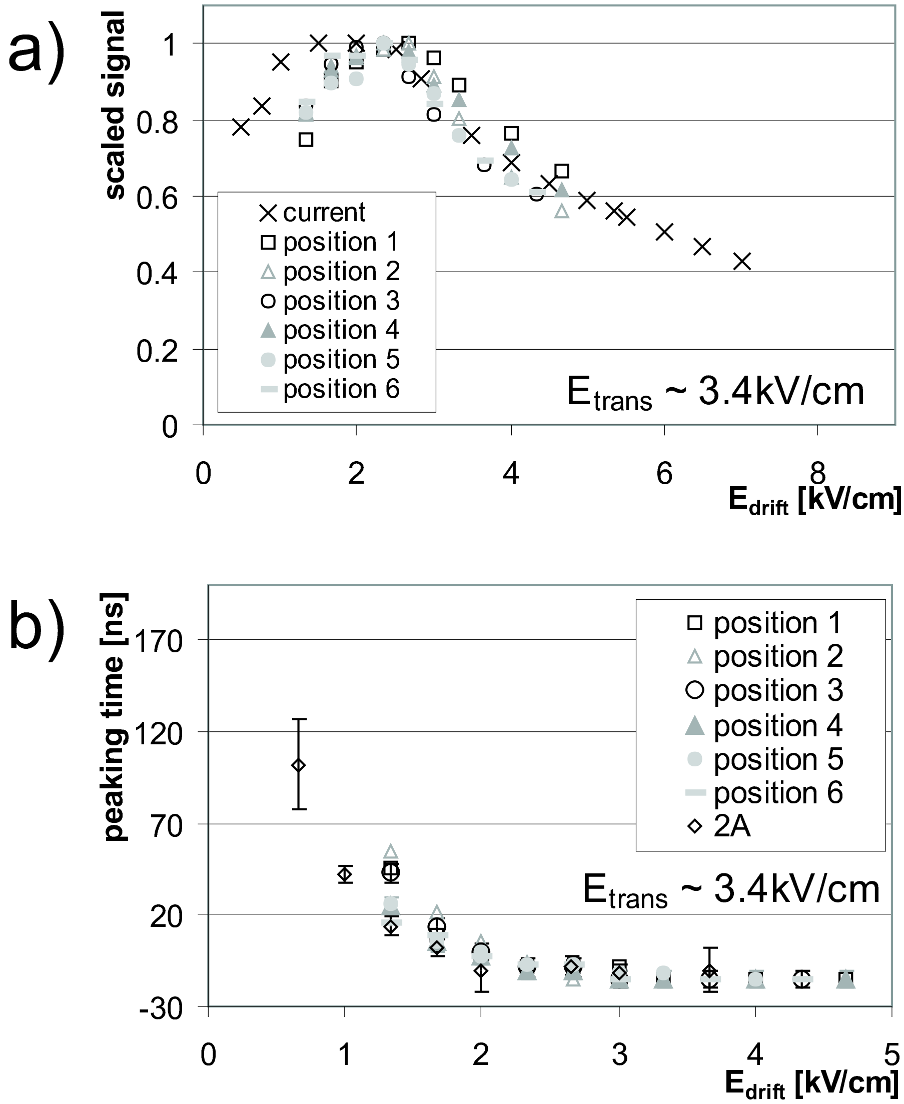

Figure 6.19: Transparency curves (a) and peaking times (b) of module 1A for different source positions across the module. The open symbols represent measurements with the source placed above one substrate, the full symbols stand for scans above the other substrate.

The GEM sag within this module had not been detected before. These results show the importance of module tests across the whole active surface to discover possible defects.

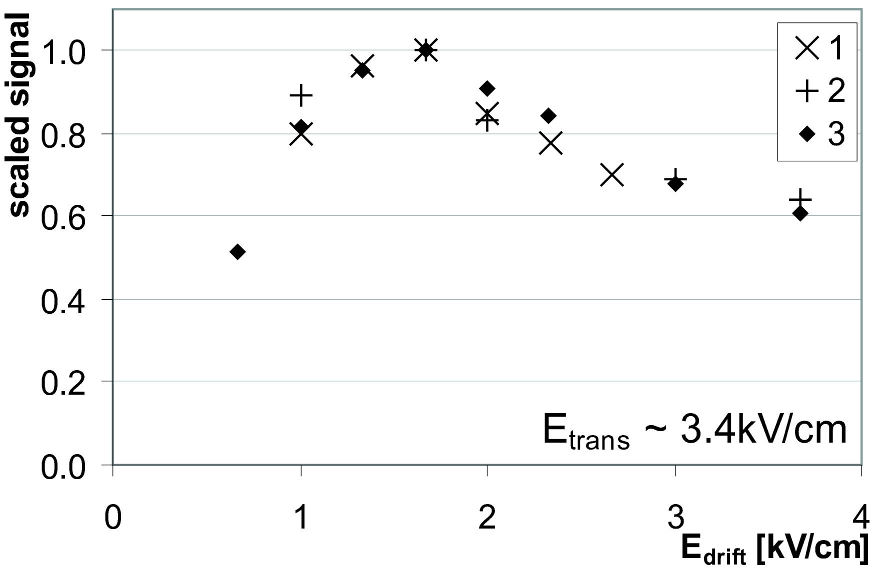

Figure 6.20: Transparency curves of module 2A for different source positions across the module.

6.3.3 Summary

A comparison of the Würth– and CERN GEMs shows that only a detector module equipped with a Würth GEM can be operated on the transparency plateau in all three gas mixtures under test using PreMux128 and APVM electronics. For the CERN GEMs an overlap of decreasing ballistic coefficient and decreasing transparency has been found.

Measuring the uniformity within the four CERN GEMs, two parameters that may influence the performance of any GEM were discovered:

GEM sag: The sagging of the GEM has a great impact on the operating voltage of a detector. The uniformity of performance across the detector is lost. Thus, means have to be found to stabilise the foil and prevent the sag.

GEM hole variations: Variations of the GEM hole diameter may affect the GEM transparency. The drift field setting for detector operation has to be chosen accordingly. The cause for such hole diameter variations is to be found in the GEM manufacturing process.

Both effects endanger a large scale use of MSGC+GEM detectors as it has been foreseen for the CMS experiment. For a tracking system that contains

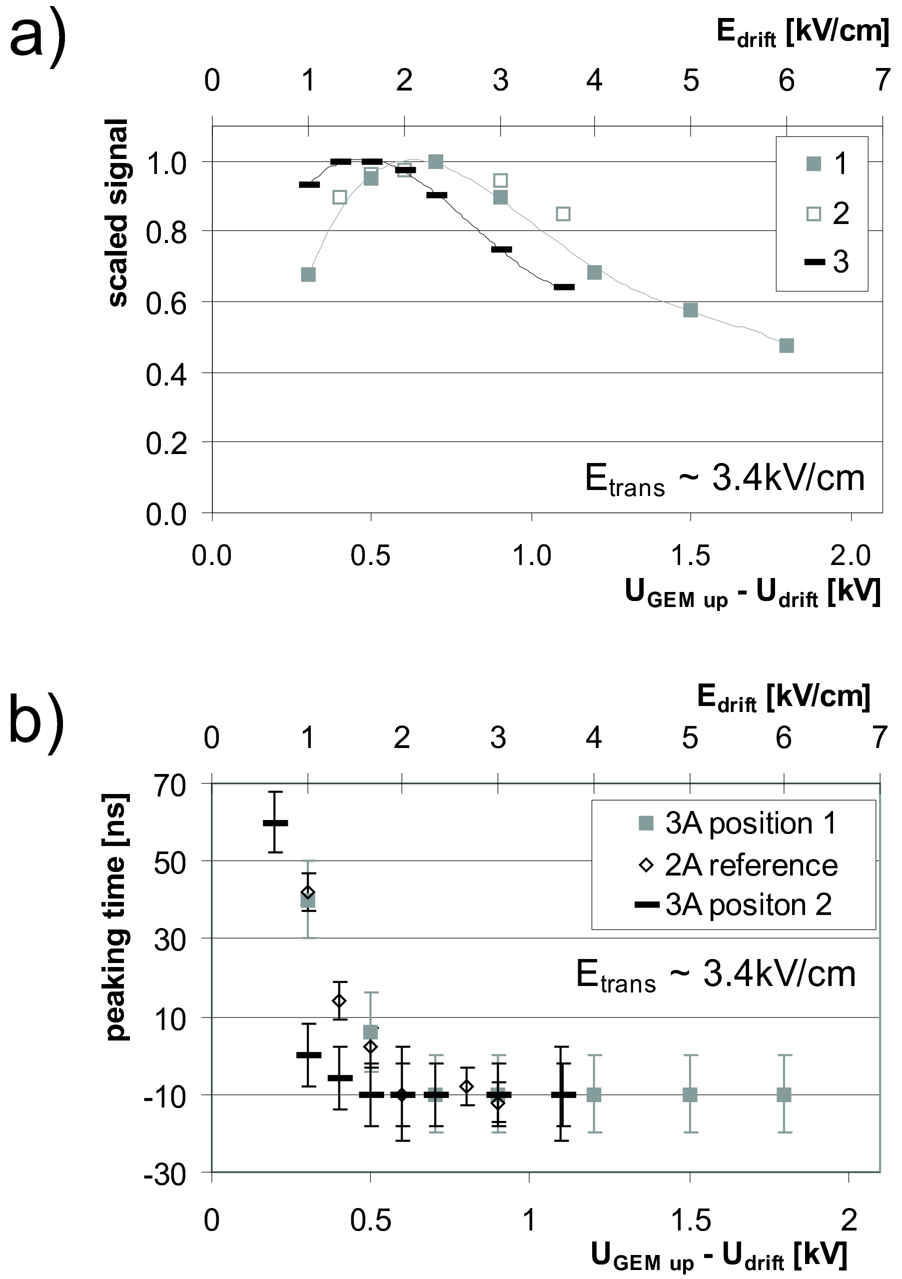

Figure 6.21: Transparency curves (a) and peaking times (b) of module 3B for different source positions across the module. To the peaking time measurements, a curve obtained for module 2A has been added as a reference.

several thousand MSGC+GEM detectors, all modules have to show uniform performance. Thus a way to overcome the described problems has to be found, before MSGC+GEMs can be used for large scale experiments.

6.4 The transfer field

6.4.1 Signal shape and peaking time

It can be easily seen, that the transfer field has no influence on the signal shape. The amplified electron cloud produced within the GEM just crosses the transfer space on it's way to the substrate. The drift time through the transfer space is given by the drift velocity. Thus the signal will be delayed if the drift velocity decreases as can be seen in the simulation in figure 6.23. To obtain those plots, the same LabView program as in section 6.2.1 was used.

Measurements of the delay curves in the three gases were also performed for different transfer fields. In Figure 6.22, superimposed delay scans in Ne/DME are shown as an example. As expected, the shape of the signal is independent of the transfer field. The same is true for the two other gas mixtures.

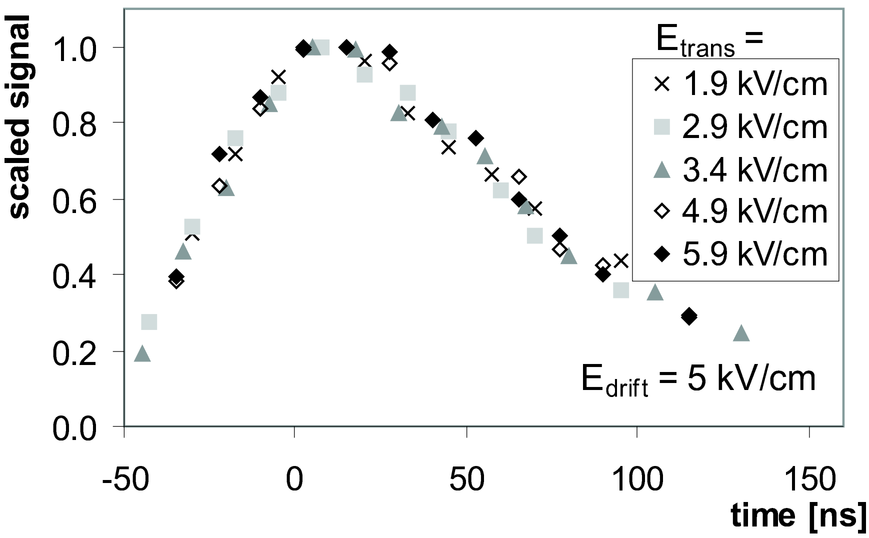

Figure 6.22: Delay curves for different transfer fields in Ne/DME. The offset for the different delay scans has been adapted to overlay the curves.

On the other hand, a shift of the peaking time at lower E_{trans} is observed, as can be seen in figure 6.24. Again, for the DME–based gas mixtures the peaking time starts to shif below 4 kV/cm. For Ar/CO_2, it remains constant until below 2 kV/cm.

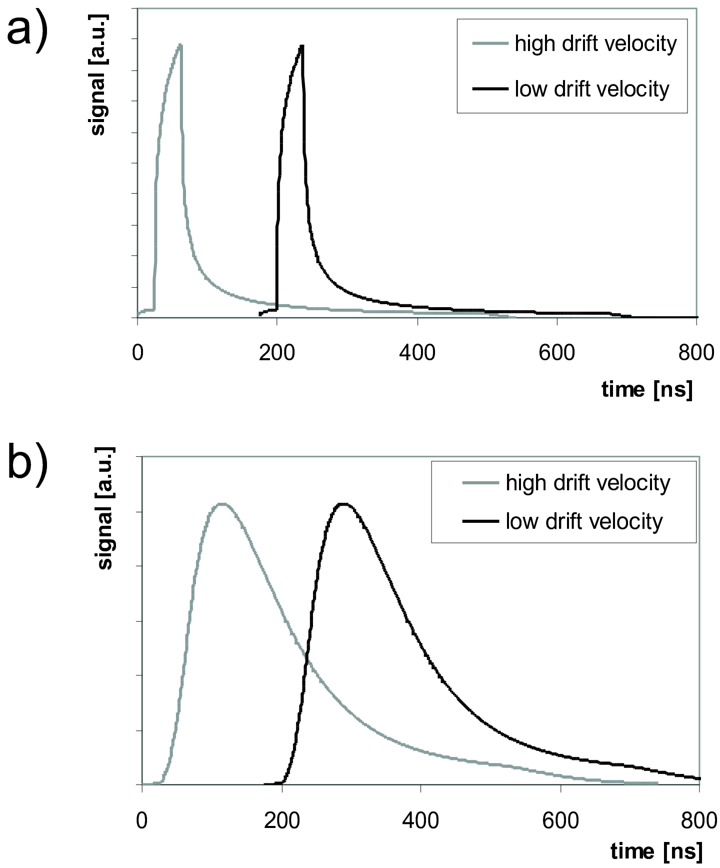

Figure 6.23: The detector signal before (a) and after (b) the electronic shaping for different drift velocities in the transfer space. For both cases, the same total detector amplification is used.

6.4.2 Signal

It is known, that the transfer field hardly influences the GEM transparency [19]. Thus the only impact of the transfer field on the size of the detector signal should come from the increasing amplification due to the increased transfer field.

Figure 6.25 shows the dependence of the cluster charge on the transfer field in Ne/DME and Ar/CO_2. For these measurements, module 2A was used. The two curves have been normalised setting the signal at a transfer field of 4.3 kV/cm to 1. The absolute signals are not comparable, since the measurements for non of the scans were be performed on the transparency plateau.

The signal shows the expected linear increase with the transfer field. Obviously, the slope of the signal curve is the same for the two gas mixtures.

Even though the measurement was not performed for $Ne/DME/CO_2$, no deviation from the results obtained here is to be expected.

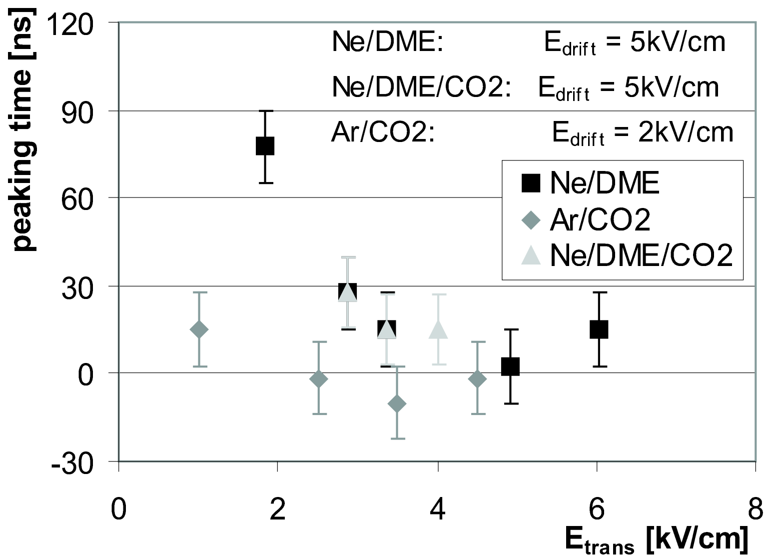

Figure 6.24: Dependence of the peaking time on the transfer field in three gas mixtures.

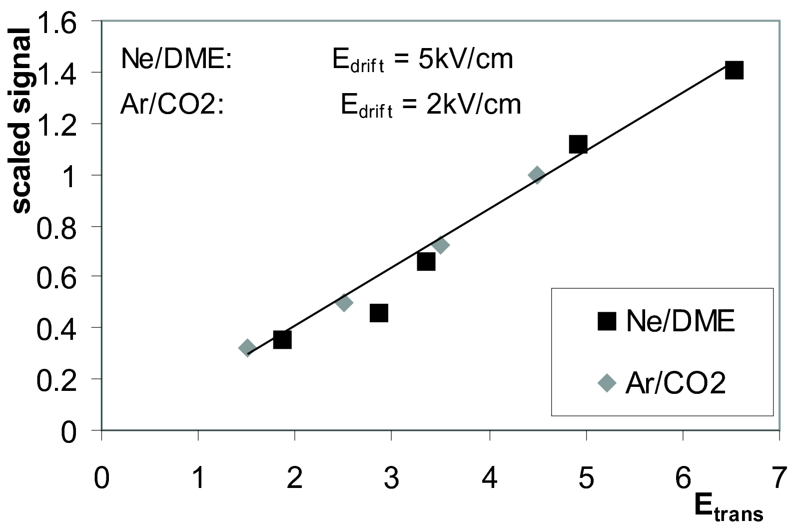

Figure 6.25: Cluster charge vs. transfer field in three gas mixtures for module 2A. The cluster charge is scaled so that it is 1 for a transfer field of 4.3 kV/cm.

Chapter 7

Conclusions and outlook

In this thesis, the high rate capability and transparency of a pre–series of MSGC+GEM detectors was investigated. For these tests, five modules were assembled in Aachen with GEM foils from the CERN workshop and Würth Elektronik GmbH. In addition 13 modules from Karlsruhe participated in the high rate tests.

The 18 detectors from the two institutes were irradiated in a high intensity hadron beam together. All five Aachen–built MSGC+GEMs and eleven of the Karlsruhe detectors proved their robustness under LHC like conditions. In addition, a noticeable safety margin of operation has been demonstrated.

Even though MSGC+GEMs will not be used in the CMS experiment, they have proven their readiness for high rate experiments.

The GEM transparency of the CMS prototypes has been investigated. Ar/CO_2 was found to be an adequate gas mixture for the operation at maximum transparency using the fast CMS electronics. Slower DME–based gas mixtures have also been investigated. Here only the geometry of the Würth GEM leads to a sufficiently long transparency plateau.

The MSGC+GEMs are only one example for a vast number of applications of GEM foils. Single and multiple GEM detector technology is envisaged or already used in a number of high energy experiments like HERA b, LHC b or COMPASS. However, the use of GEM technology is not limited to high energy physics. For example, multiple GEM prototypes are developed for medical imaging [39].

List of Figures

Bibliography

[1] O. Nachtmann, *Phnomene und Konzepte der Elementarteilchenphysik*, Viehweg, 1986.

[2] B.W. Lee, C. Quigg, H.B. Thacker *Weak interactions at very high energies: The role of the higgs boson mass* Phys. Rev. D16, 1977.

[3] The LEP collaborations ALEPH, DELPHI, L3, OPAL, the LEP electroweak working group and the SLD heavy flavour and electroweak groups, *A combination of preliminary electroweak measurements and constraints on the standard model*, CERN–EP 2001-21

[4] W.Blum and L.Rolandi, *Particle detection with Drift chambers*, Springer Verlag, 1994.

[5] C.Grupen, *Particle detectors*, Cambridge University Press, 1996

[6] R.K. Bock et. al., *Formulae and methods in experimental data evaluation*, General Glossary Volume 1, 1984

[7] ALEPH, DELPHI, L3 and OPAL collaborations *Search for the Standard Model Higgs Boson at LEP* CERN-EP/2001-055, 2001

[8] O.Bouhali et. al., *Operation of microstrip gas counters with DME–based gas mixtures*, Nucl. Instr. and Meth. A413, 1998.

[9] G. Baum et al. *Proposal for a common muon and proton apparatus for structure and spectroscopy* CERN/SPSLC 96-14 SPSC/P 297

[10] LHC b collaboration *LHC b vertex locator TDR* CERN, 2001

[11] L.L. Jones, *PreMux128 specifications version 2.3*, Rutherford Appleton Laboratory, 1995.

[12] O. Bouhali et al., *CMS Forward-Backward MSGC milestone*, CMS Note 1998/095, CERN, 1998.

[13] R. Bellazini et. al., *Electric field, avalanche growth and signal development in micro–strip gas chamber and micro–gap chamber*, INFN PI/AE 94/02.

[14] O. Pooth *Micro Strip Gas Detector Modules: Development and Integration in the Forward Tracking System of the CMS Experiment* PITHA 99/29, RWTH Aachen, 1999.

[15] S. Bachmann, *Investigation of Microstrip Gas Chambers and their application in the CMS Experiment*, PITHA 98/25, RWTH Aachen, 1998.

[16] R. Bellazzini et al., *The CMS Micro–strip Gas Chamber project – Development of a high resolution tracking detector for harsh radiation environments* Nucl. Instr. and Meth. A457, 2001.

[17] M. Argeron et al., *Robustness Test of a System of MSGC+GEM Detectors at the Cyclotron Facility of the Paul Scherrer Institute*, CMS Note 2000/058, CERN, 2000.

[18] M. Argeron et al., *Experimental and simulation study of the various operation modes of MSGC+GEM detectors*, to be published.

[19] S. Bachmann et al., *Charge Amplification and Transfer Processes in the Gas Electron Multiplier*, CERN-EP/99-48.

[20] F. Sauli, *Gas detectors: achievments and trends*, CERN-EP/2000-80.

[21] J. Kremp, *Entwicklung eines Mikrostreifengasdetektormoduls für den inneren Spurdetektor bei CMS*, PITHA 97/47, RWTH Aachen, December 1997.

[22] M. Petertil, P. Schmitz, *Readout and Calibration of CMS Pipeline Chips to Examine the Signal Development of Tracking Strip Detectors*, CMS NOTE 2001/016

[23] G. de Lentdecker, Universite Libre de Bruxelles, Belgium private communications

[24] R. Bouclier, *Study of materials outgasing and their effect on gaseous detector lifetime*, CMS TN96/38, march 1996

[25] C.Caso et. al, *The european physics jornal C3*, 1998.

[26] CMS Collaboration, *CMS, the compact muopn solenoid, Technical proposal*, CERN/LHCC 94-38, 1994.

[27] CMS Collaboration, *The Tracker Project Technical Design Report*, CERN/LHCC 98-6, 1998

[28] *Addendum to the CMS tracker TDR*, CERN/LHCC 2000-016, 2000

[29] F. Sauli, *Primciples of operation of multiwire proportional and drift chambers*, CERN 77-09, 1977.

[30] V. Commichau, *PREMUXADO00, instruction manual*, RWTH Aachen, 1996.

[31] B. Baiboussinov et al., *Readout and slow control system for the forward MSGC prototype*, CERN documentation, 1997.

[32] S. Viesbeck, *Untersuchungen von Prototypen der Mikrostreifen-Gaskammern (MSGC) des inneren Spurkammersystems des HERA-B Experiments*, Technische Universität Heidelberg, 1996.

[33] C. Richter *Development of Micro Pattern Gas Detectors for High Rate Experiments* Technische Universität Heidelberg, 2000.

[34] V. Peskov, *Feedback and breakdown in microstrip gas counters*, Nuclear Instruments and Methods A397, 1997.

[35] D. Macke, *Micro Strip Gas Chambers with Gas Electron Multipliers and their Application in the CMS* , PITHA 00/01, RWTH Aachen, October 2000.

[36] M. Gottschalk, *Bau und Test eines GEM verstärkten MSGC–Moduls für den CMS Vorwärtsbereich* , PITHA 00/01, RWTH Aachen, October 2000. PITHA 00/03, RWTH Aachen, February 2000.

[37] A. Nowack, *Steigert eine Gas–Elektron–Vervielfachungsfolie die Betriebssicherheit eiines Mikrostreifengasdetektors*, PITHA 98/30, RWTH Aachen 1998.

[38] A. Nowack *Investigations of a Pre-Series of Micro Strip Gas Chambers with Gas Electron Multipliers for High Rate Environments*, phd thesis to be published, Aachen

[39] S. Bachman et.al., *Development and applications of the gas electron multiplier*, CERN EP 2000–299.

[40] M. French, *APV6 user manual*, Rutherford Appleton Laboratory, 1997.

Appendix A

Detector layout

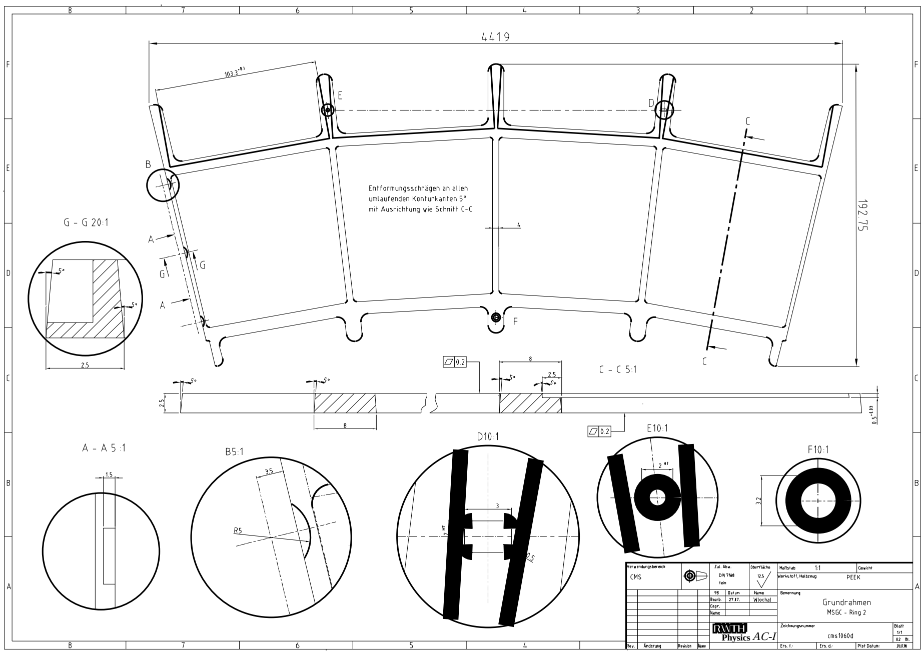

Figure A.1: Technical drawing of the bottom frame of an mf2 module.

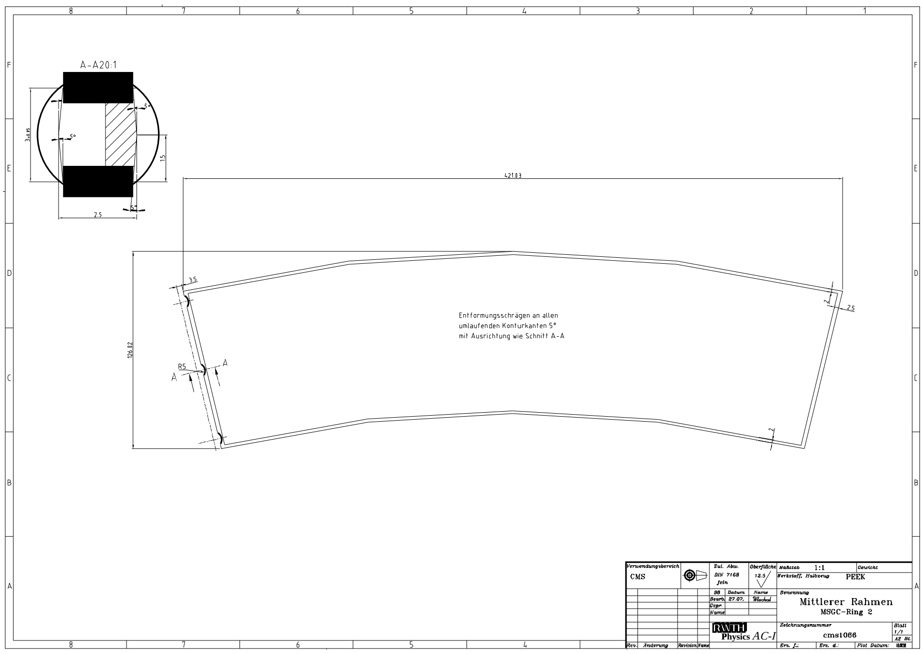

Figure A.2: Technical drawing of the spacer frames of an mf2 module.

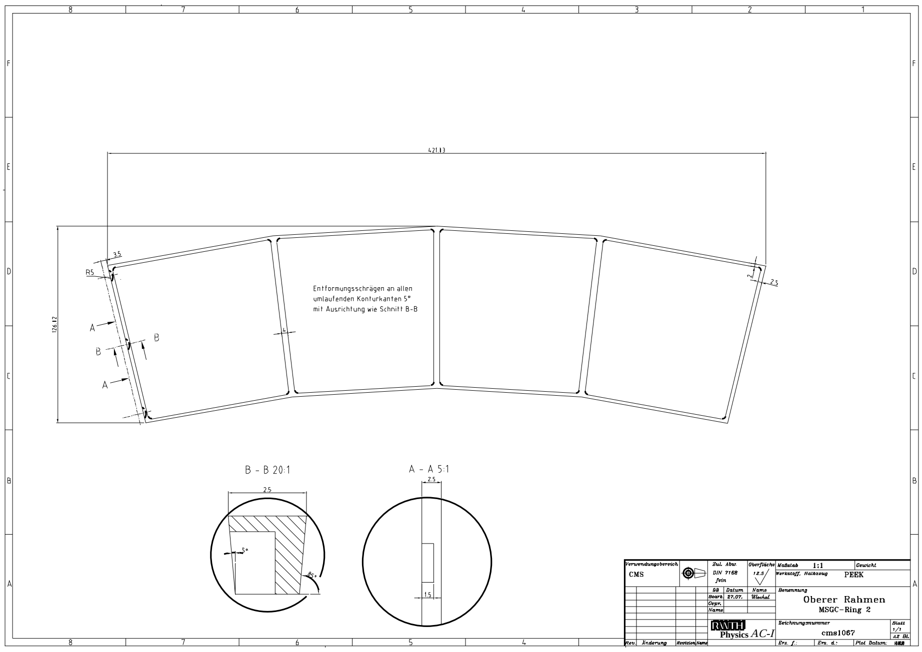

Figure A.3: Technical drawing of the stabiliser frame of an mf2 module.

Appendix B

GEM manufacturing processes

Manufacturing processes for the two types of GEM foils		
	Würth GEM	CERN GEM
a)	Coating of the foil with a photo resist	
b)	Alignment of the masks that define the hole pattern on both sides of the GEM foil. Exposure to UV light	
c)	Development of the photo resist	
d)	Wet etching with a copper solvent thus engraving the hole pattern into the copper.	
e)	Removal of photoresist.	
f)	Plasma etching of cylindrical holes into the polymer foil. The polymer is removed even a short way underneath the copper (underetching).	Wet etching of double conical holes into the polymer foil.
g)	Wet etching to remove the copper extending into the holes. This way, the HV capability of the foil is increases	Wet etching to remove a thin ring of copper around the holes to improve the HV capability of the foil

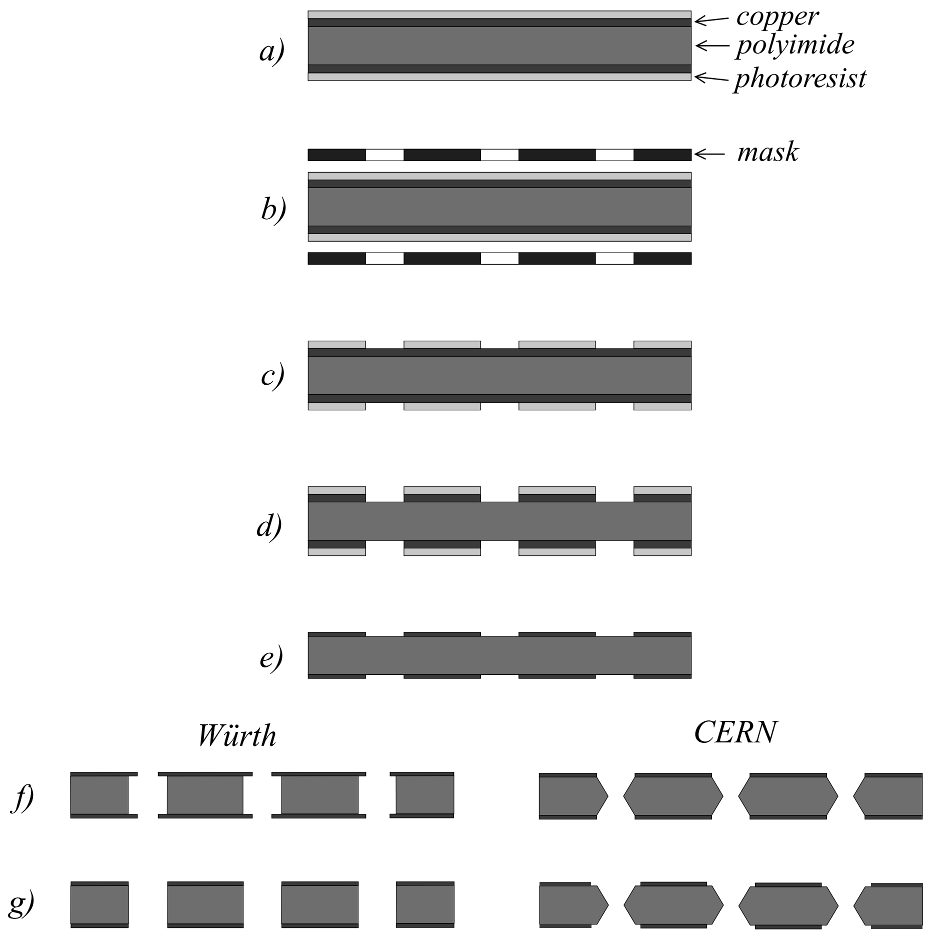

Figure B.1: Scheme of the steps in the GEM production process.

Appendix C

Detection of broken anode strips

To detect a broken strip, the following three methods can be used:

- Monitoring of the beam profiles. A broken strip shows a reduced number of particle hits.
- Injection of a signal that is coupled capacitively to the readout channels. A broken strip shows a reduced signal due to it's reduced capacitance.
- Investigation of the noise (usually determined from the pedestal runs). Due to their reduced capacitance, broken strips show a reduced noise. Figure C.1 shows the loss of a strip identified by this method.

During the MF2 milestone, all three methods were used. Thus the time of a strip loss could be determined with a precision of one runfile.

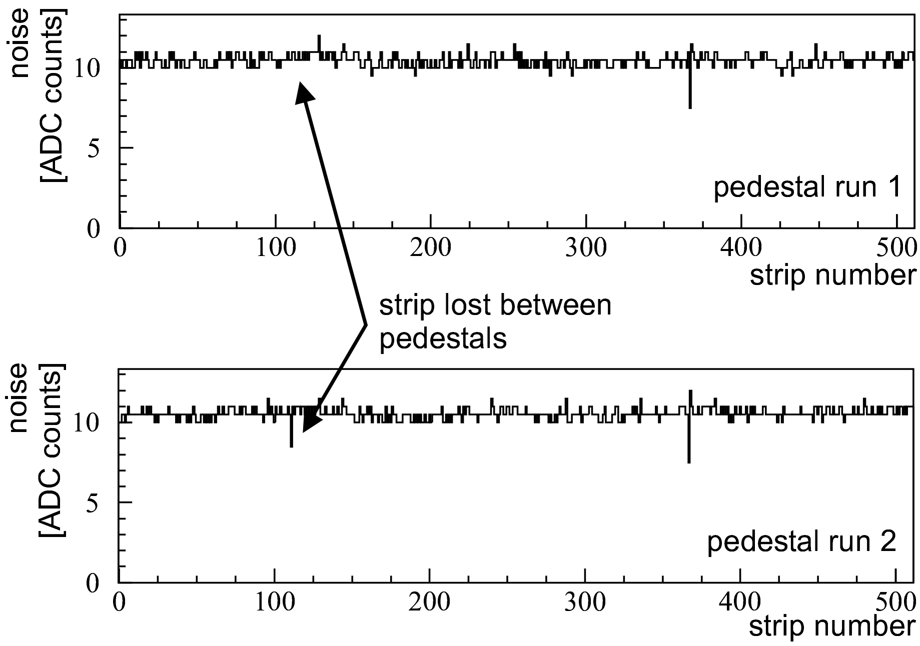

Figure C.1: Noise distribution for one detector before and after a strip loss.

Appendix D

The PreMux128 readout chip

The PreMux128 [11] is a 128 channel chip that is used as frontend electronics to read out MSGC+GEM detectors. As can be seen in figure D.1, each readout channel consists of a test signal input, two protection diodes[1], a charge sensitive preamplifer, a CR–RC shaper with a shaping constant of 40–50 ns and a DCS[2] circuit.

The detector signals from the 128 PreMux128 channels are read out in series using an analogue multiplexer that is also implemented on the chip. Several PreMux128 chips may be daisy chained and read out by a single FADC.

To read out the 512 anode strips of an MSGC+GEM detector, four PreMux128 chips have to be mounted on a hybrid that then will be be bonded to the substrate.

D.1 Readout modes

The detector signal may be read out in DCS mode. In that case, two 2 pF capacitors per channel are connected to the CR–RC shaper through the switches S1 and S2. When one of those switches is opened, the corresponding capacitor stores the signal voltage. Thus, two samples of a signal at t_{S1} and t_{S2} can be read out.

S2 is closed at the maximum of the signal. S1 is closed sufficiently long before or after the signal to provide a measurement of the baseline of the channel. On the SBM, the difference between the S1 and S2 signals is determined and read out. However, the DCS mode was not used in this thesis.

Instead, the so–called dummy channel mode has been chosen. There, the signal from an additional 129th channel –being grounded– replaces the S1 information. In that case, the difference between the ground and the signal at S2 is read out.

In a particle detector, the exact timeing of the maximum of the signal with respect to the trigger is not known. Normally, the trigger is provided before

[1] They avoid damage to the readout channel in case of a substrate discharge

[2] **D**ouble **C**orrellated **S**ampling

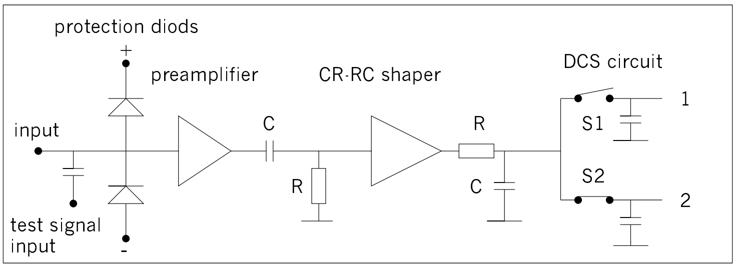

Figure D.1: Principle of one PreMux128 channel.

the signal of the MSGC+GEM is at it's maximum and thus has to be delayed. The correct delay value is determined by a so–called delay scan. There, the MSGC+GEM signal is measured for different delay values to find the signal maximum.

D.2 Ballistic coefficient

When only the maximum of a pulse is read out with fast electronics, part of the signal charge may be lost. To quantify that loss, the so–called 'ballistic coefficient' has been introduced. It is defined as:

$$ballistic\ coefficient = \frac{S}{S_{delta}}$$

where S is the signal seen by the readout electronics and S_{delta} is the signal that would have been seen if the input charge had arrived in form of a delta pulse.

Consequently, the readout signal decreases proportional to the ballistic coefficient.

The ballistic coefficient depends on the electron– and ion collection time of the MSGC+GEM, the evolution of the signal in time, the signal shaping by the electronics and the sampling method. It is below 1 for any gas detector, because the signal is spread at least across the drift time of the electrons and thus it is no longer an ideal delta pulse. However, this effect is noticeable only for detectors with small shaping constants like PreMux128 and APVM. For a shaping constant that is much longer than the electron collection time, the ballistic coefficient is approximately 1.

Appendix E

The APVM readout chip

The 128 channel APVM chip [40] was constructed to read out the detectors of the CMS MSGC tracker. The principle of one readout channel can be found in figure E.1. There it can be seen, that the preamplifier and CR–RC shaper are followed by a 160 column deep analogue pipeline.

The CR-RC shaper has a variable shaping constant. The shaping can be adjusted using a programmable register ('vsha'). For the CMS experiment, a 50 ns shaping will be used corresponding to vsha=50.

Each APVM channel is read out with the LHC bunch crossing frequency of 40 Mhz. The data is stored in the analogue pipeline and can then be read out in three different ways:

peak mode: Only one pipeline entry is read out at the APVM signal maximum. Therefore the correct column has to be found as will be described in the following:

For an APVM readout, the trigger arrives after the maximum of the APVM signal. The data corresponding to the triggered event is still stored in the pipeline and can now be read out. The delay of the trigger with respect to the signal is called trigger latency and defines which column is to be read out (see figure E.2).

deconvolution mode: The deconvolution mode was designed to adjust the rise time of the signal to the 25 ns between two LHC bunch crossings [27]. Therefore, three column entries in the rising edge of the signal are added in a weighted sum. The first column to read out is again defined by the trigger latency.

Due to the deconvolution, the ballistic coefficient decreases and the noise increases. As a consequence, the SNR is reduced by a factor of 2.2.

multi mode: In the multi mode, three columns are read out for each trigger.

Like the PreMux128, the APVM channels are multiplexed when they are read out. Each chip is addressed and configured via a two wire serial interface according to the Phillips I^2C standard [40]. More information about the APVM chips used in this thesis can be found in [38].

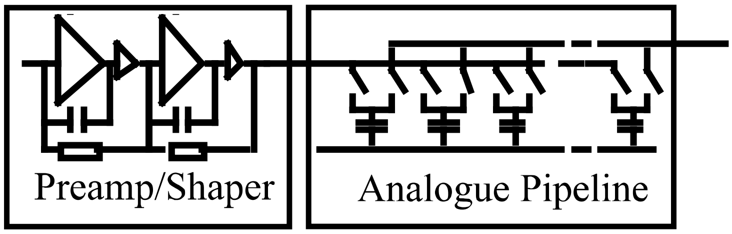

Figure E.1: Principle of one APVM channel.

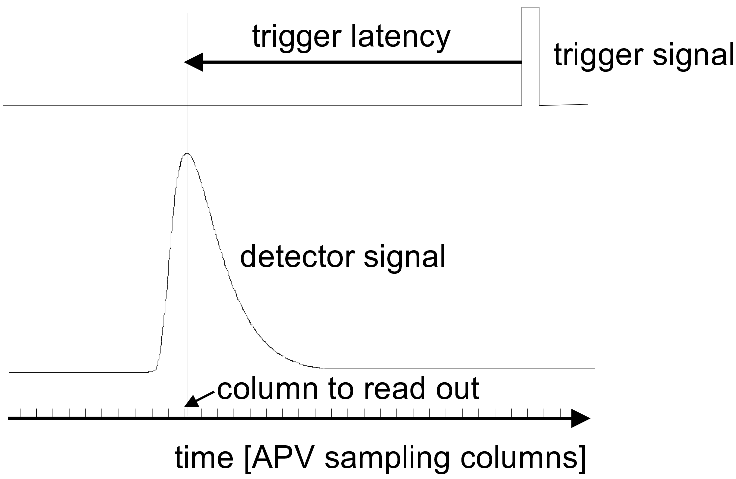

Figure E.2: Principle of the trigger latency in peak mode.

Appendix F

Data analysis with IRIS

To analyse the data taken during the tests described in this thesis, the IRIS[1] software was used [21, 36, 38]. It contains routines for hit detection and signal processing (see section F.1) in the PreMux128 and APVM data. In addition, current monitoring and discharge detection routines have been implemented into a version especially designed for the PSI conditions (see section F.2).

F.1 Hit finding procedure

F.1.1 Data corrections

The data $r_{i,j}$ read out from a PreMux128 or APVM chip for event i and channel j is the sum of several components:

- $s_{i,j}$: signal amplitude
- p_j: pedestal value
- c_i: common mode
- $n_{i,j}$: noise
- h_i: HV crosstalk

$$r_{i,j} = s_{i,j} + p_j + c_i + n_{i,j} + h_i$$

For data analysis, only the signal amplitude is of interest. Thus the other contributions have to be known and appropriate corrections applied before searching for the detector signal.

Pedestals, common mode and HV crosstalk are systematic effects and can be corrected for. The data with all corrections applied is called baseline. The noise on the other hand is a random fluctuation and has to be handled differently.

[1] **I**nteractive **R**unfile **I**nspection **S**ystem

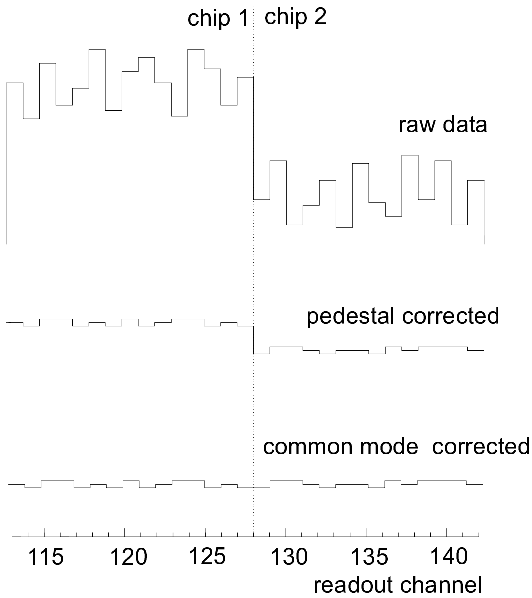

Figure F.1: The effect of pedestal subtraction and common mode correction on the raw data.

Pedestal and noise

Every channel has it's own characteristic pedestal and noise. They are determined using so–called pedestal runs where data without traversing particles is taken, using a random trigger. The pedestals can then be determined to be the average raw data of N readout cycles:

$$p_j = \frac{1}{N}\sum_{i=1}^{N} r_{i,j}$$

The noise is the standard deviation of the detector baseline.

Common mode

The common mode is caused by a random fluctuation of the raw data that all readout channels in one chip have in common. Thus it has to be determined individually for each chip and event in pedestal runs as well as in physics runs[2]. Common mode is defined as the deviation of the raw data from the pedestal:

$$c_i = \frac{1}{128}\sum_{j=1}^{128}(r_{i,j} - p_j)$$

The effect of pedestal subtraction and common mode correction on the raw data can be seen in figure F.1.

[2]Runs with traversing particles.

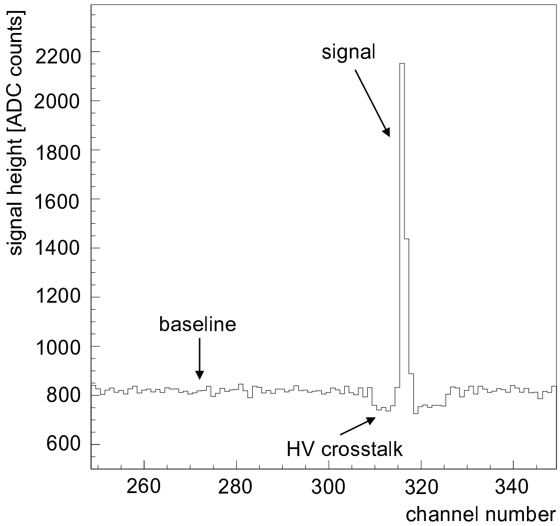

Figure F.2: The effect of the HV crosstalk on the data.

HV crosstalk

Another correction that has to be applied on individual events in physics runs is the HV crosstalk. If a particle is detected over a HV group, the positive charges that are collected on the cathode strips must be compensated for by the power supply. For large signals, the electrons are not provided fast enough. Consequently, the output of the channel is reduced. Uncorrected, this effect leads to a systematically smaller signal (see figure F.2). The effect is corrected for by calculating the average deviation of all channels not in the signal cluster (HV crosstalk):

$$h_g = \frac{1}{G}\sum_{g=1}^{G}(r_{i,j} - p_j - c_i)$$

where G is the number of channels used for averaging.

F.1.2 Hit detection

In order to identify a traversing particle, channels where the baseline exceeds the noise fluctuations have to be identified. The usual criterion is, that the signal is by a factor n larger than the noise: $s_i > n \cdot n_i$. Typically n is between 1.5 and 2.5. However, the average particle leaves a signal on more than one anode strip. These strips form a cluster. An example of one cluster can be found in figure F.3.

When a cluster has been identified, it's characteristic properties like cluster charge, SNR and the hit position x (in anode pitches) are calculated.

The cluster charge C is the sum of the signals of all strips in a cluster:

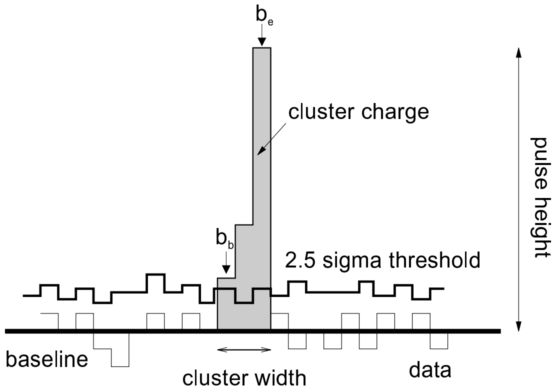

Figure F.3: A typical cluster induced by a particle crossing the detector. The cluster begins at strip b_b and ends at strip b_e.

$$C = \sum_{i=b_b}^{b_e} s_i$$

Where b_b is the number of the first strip in the cluster and b_e that of the last strip.

The SNR is the total charge of a cluster divided by the mean square of the strip noise:

$$SNR = \frac{\sum_{i=b_b}^{b_e} s_i}{\sqrt{\frac{\sum_{i=b_b}^{b_e} n_i^2}{(b_e - b_b)}}}$$

Finally, the hit position x is calculated using the so–called COG[3] method:

$$x = \frac{\sum_{i=b_b}^{b_e} i \cdot s_i}{\sum_{i=b_b}^{b_e} s_i}$$

With the vast amount of readout channels in an MSGC+GEM, a few channels per event may exceed the signal threshold due to statistical fluctuations. Thus some fake hits will be found. They leave a so–called noise peak that is clearly separated from the signal of the particle (see figure F.4 (a)). Therefore, a second cut has to be defined to get rid of these unwanted hits. For these cuts, several approaches are possible:

- A cut on the height of the highest strip in a cluster like $s_i > N \cdot n_i$ with $N > n$, typically between 3 and 5.
- A cut on cluster charge or SNR.

The effect of the second cut can be seen in figure F.4 (b). If several clusters remain after applying the second cut, only the largest one is used for further anslysis.

[3]**C**enter **O**f **G**ravity

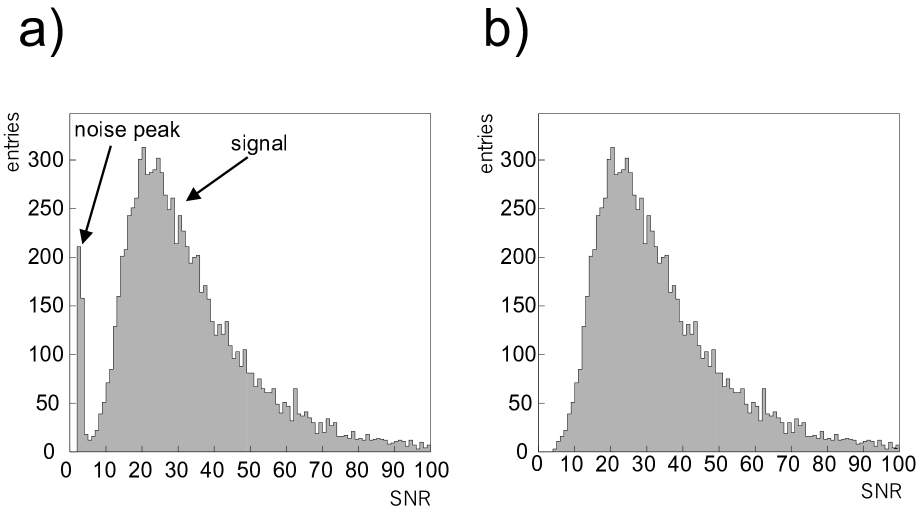

Figure F.4: Distribution of detector SNR without (a) and with (b) an additional cut on the cluster SNR.

F.2 Current monitoring algorithms

In chapter 5.4, the different types of discharges within an MSGC+GEM detector are described. In addition, there are some module–independent effects that have to be considered by a discharge detection algorithm. While here only a short overview will be given, they are described in detail in [35, 36].

In principle baseline determination for the detector current is similar to the algorithms described in the previous section. However, some systematic differences have to be considered:

- The detector baseline is not constant. It depends on the gain of a module and the beam intensity (see chapter 5.4). Especially the second parameter may lead to sudden shifts in the baseline, for example when the beam is lost during the runfile (see figure F.5). Therefore, the baseline has to be determined for each event individually. Module–independent events like beam losses may then be identified, because they will be seen in all modules.
- The discharges themselves are more complex than the events described in the previous section. GEM discharges for example may last over several seconds and may thus have a noticeable impact on the detector baseline (see figure F.6 and chapter 5.4). Therefore, the bin–to bin–variation of the current data is searched for variations that exceed a defined threshold. If a GEM discharge is found, the baseline is either calculated from the data before the discharge or the baseline from the previous event is used (if the discharge occurs at the beginning of a slow–control–event). If a GEM discharge occurs between events, a shift of the baseline with respect to the previous event is detected.

When the baseline is known, the peak finding algorithms as described in the previous section are applied to the corrected data.

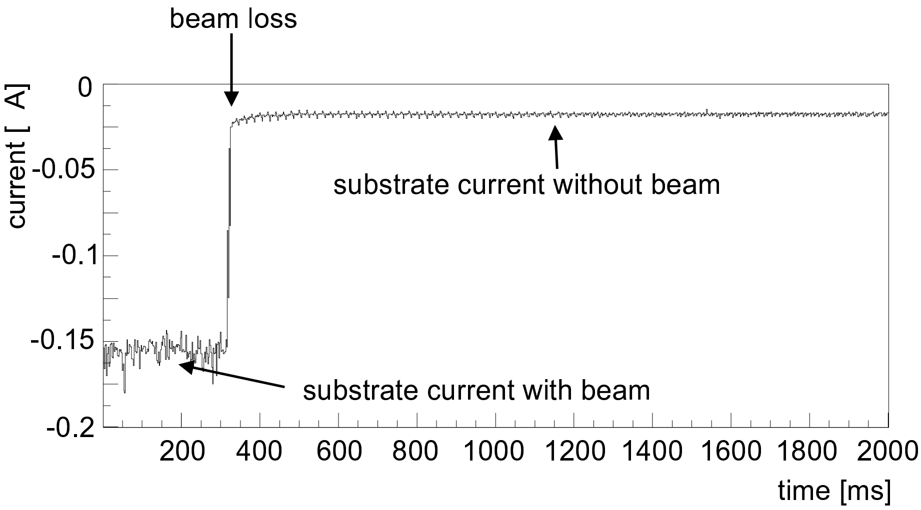

Figure F.5: Effect of a beam loss on the current on one substrate: The current drawn at high intensity is reduced to almost 0. The same drop can be observed for all channels. When the beam is brought back, the current will slowly return to it's initial value.

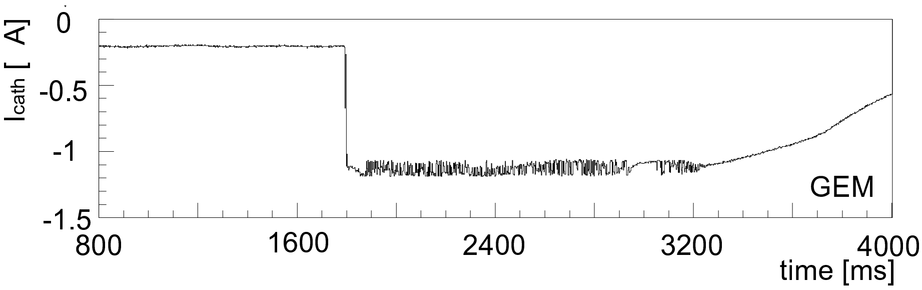

Figure F.6: Effect of a GEM discharge on the upper GEM electrode.

After all discharges have been found, the software searches for possible correlations between substrate and GEM activity. In this way discharges between substrate and GEM or substrate sparks that are triggered by a GEM discharge are identified.

Acknowledgements

Finally I wish to thank all the people who supported me in the past three years:

Prof. Flügge offered me the chance to start my work in the field of MSGCs for the CMS detector and helped me to finish it, when the MSGC+GEMs were no longer needed in the CMS tracker.

Dr. Reiner Schulte and Dr. Wolfgang Struczinski always helped me with my problems and questions.

Thanks to Dirk Macke for the support, especially at the beginning of my thesis, when I had to find my way into the subject. The experience at the x5 test beam proved invaluable.

I worked with Andreas Nowack for three years and he always was the expert on subjects where I was not (especially the analysis software). Without him, mf2 would have been impossible.

Thanks to Jürgen Kremp for his work on PETRA, the people in Lyon for the PSI data acquisition system and to Markus Petertill and Dr. Peter Schmitz for the APVM readout.

I also want to thank all my other colleagues in Aachen: Oliver Pooth, Christof Knöß, Rasmus Ischebeck, Matthias Gottschalk, Markus Axer, Michael Pöttgens, Peter Schorn, Thorsten Francke, Can Ilgin, Jan Niehusmann, Andreas Krantz and anyone else who read my thesis and offered corrections.

The support of the mechanics workshop, especially Mr. Boffin, Mr. Bock and Mr. Jahn was as invaluable as the help from Dr. Commichau, Dr. Hangarter, Mr. Camps and Mr. Beissel where electronics problems were concerned.

Many people in the CMS collaboration have been of great help during my thesis. Special thanks have to go to Walter Van Doninck and Jean–Marie Brom for managing the mf2 milestone. I also want to thank the mf2 analysis group: Catherine Vander Velde, Fred Udo, Valery Zhukov, Pascal Vanlaer, Tom Beckers, Gilles De Lentdecker, Stephanie Moreau and Olivier Devrode for the fruitful work on our papers.

My special gratitude is to Stefan for tea and discussions on "the lord and the world".

Thanks to my parents for financial, scientific and personal support. Thank you also for showing me the fascination in physics.

My husband was always there with his support and love.

Lebenslauf

Name:	Anette Zander
Geburtsname:	Fuchs
Geburtsdatum:	17.5.1974
Geburtsort:	Kassel

1980-1984	Besuch der Grundschule St. Martinus in Schlich
1984-1993	Besuch des Städtischen Gymnasiums am Wirteltor, Düren
1993	Abschluß des Gymnasiums mit dem Abitur
1993-1998	Physikstudium an der RWTH Aachen
3.7.1998	Trauung mit Andreas Zander im Standesamt Eilendorf
1998	Abschluß des Studiums mit dem Diplom
1998-2001	Promotion am III. Physikalischen Institut der RWTH Aachen